The First Stars and the Convective-Reactive Regime.

by

Ondrea Clarkson
Bachelor of Science in Physics, University of Illinois at Chicago, 2014
A Dissertation Submitted in Partial Fulfillment of the
Requirements for the Degree of

DOCTOR OF PHILOSOPHY

in the Department of Physics and Astronomy

University of Victoria

The First Stars and the Convective-Reactive Regime.

by

Ondrea Clarkson
Bachelor of Science in Physics, University of Illinois at Chicago, 2014

Supervisory Committee

Dr. F. Herwig, Supervisor
(Department of Physics and Astronomy)

Dr. K. Venn, Departmental Member
(Department of Physics and Astronomy)

Dr. J. Cullen, Departmental Member
(Department of Earth and Ocean Science)

ABSTRACT

Due to their initially metal-free composition, the first stars in the Universe, which are termed Population III (Pop III) stars, were fundamentally different than later generations of stars. As of now, we have yet to observe a truly metal-free star although much effort has been placed on this task and that of finding the second generation of stars. Given they were the first stars, Pop III stars are expected to have made the first contributions to elements heavier than those produced during the Big Bang. For decades significant mixing between H and He burning layers has been reported in simulations of massive Pop III stars. In this thesis I investigate this poorly understood phenomenon and I posit that interactions between hydrogen and helium-burning layers in Pop III stars may have had a profound impact on their nucleosynthetic contribution to the early universe, and second generation of stars.

First, I examined a single massive Pop III star. This was done using a combination of stellar evolution and single-zone nucleosynthesis calculations. For this project I investigated whether the abundances in the most iron-poor stars observed at the time of publication, were reproducible by an interaction between H and He-burning layers. Here it was found that the i process may operate under such conditions. The neutrons are able to fill in odd elements such as Na, creating what is sometimes called the 'light-element [abundance] signature' in observed CEMP stars. I also present the finding that it is possible to produce elements heavier than iron as a result of the i process operating in massive Pop III stars.

A parameter study I conducted on H-He interactions in a grid of 22/26 `MESA` stellar evolution simulations is then described. I grouped these interactions into four categories based on the core-contraction phase they occur in and the convective stability of the helium-burning layer involved. I also examine in detail the hydrogen-burning conditions within massive Pop III stars and the behaviour of the CN cycle during H-He interactions. The latter is compared to observed CN ratios in CEMP stars.

Finally, I describe the first ever 4π 3D hydrodynamic simulations of H-He shells in Pop III stars. I also examine the challenges in modelling such configurations and demonstrate the contributions I have made in modelling Pop III H and He shell systems in the `PPMStar` hydrodynamics code. My contributions apply to other stellar modelling applications as well.

Contents

List of Tables

List of Figures

Acknowledgements

I would like to thank: **Douglas Rennehan** for being my best friend, partner, and Douglas fir. **My cats**, Spike (RIP baby), Werner and Margaret for cuddles and getting me out of uncomfortable social situations. **My parents, Lee Walton and Orlin Clarkson** for raising me to be the woman I am today. **Byron Clarkson** for being the biggest little bro I'll ever know. **Falk Herwig** for teaching me pushing me to my full potential. **Kim Venn** for being my guide star. **Frank Timmes** for lifting me up when it was of no benefit to you. **Claudio Ugalde** for introducing me to the wonders of stellar nucleosynthesis, and for being a wonderful mentor and person. **Kim Arvidsson** for introducing me to stellar interiors and Red Dwarf. **Anirhuda Menon** for admiring me. **Wayne Foster** for suffering with me. **Jorge Arroyo** for always encouraging me. **Benoit Cote**, **Marco Pignatari**, **Sam Jones** and **Chris Fryer** for making meetings fun. **Pavel Dennissenkov** for being a great scientific role model. **Chervin Laporte** for keepin' it real. **Jane Peng** for confiding in me and allowing me to do the same to you.

"They'll get the stars. How can you not envy them that?"
- Naomi Nagata, Leviathan Wakes

Dedication

To Byron and Mom. Thank you for making this possible.

Contributions

All calculations presented in Chapters 2-4 were preformed by me. Specific details for contributions on each project are presented at the beginning of each chapter.

Chapter 1

Introduction

1.1 Motivations and Introduction to the Problem

After the Big Bang, the baryonic matter within the Universe was primarily composed of hydrogen, helium, and a little bit of lithium. All heavier elements were created within stars, beginning with the first generation. Stars are grouped into populations depending on their overall metal content (Baade, 1944). The standard grouping places stars with a similar metal content to our Sun as Population I, stars with a lower metal content than the Sun as Population II, and metal-free stars as Population III.

Even before the Big Bang theory of cosmology was widely accepted, an early population of massive stars were introduced to explain the lack of metals in "extreme" Population II stars within the galaxy (Schwarzschild & Spitzer, 1953) among other observational quandaries. In the following years and decades, models were constructed of pure hydrogen stars (Ezer, 1961) and stars of various masses compromised of only hydrogen and helium (Ezer & Cameron, 1971; Chiosi, 1983; Castellani & Paolicchi, 1975).

In this time, mixing between H- and He-rich burning layers was observed in stellar models of zero and low metallicity. Much of this work was focused on low and intermediate mass stars ($\approx 0.8 - 8M_{\odot}$). For massive ($\gtrapprox 8M_{\odot}$) Pop III stars such an interaction was first described in 1982 for a $200M_{\odot}$ stellar model by Woosley & Weaver (1982). Since then, these interactions have been often mentioned but never investigated in great detail.

H-He interactions release large amounts of energy and can have a significant impact on the nucleosynthesis occurring in the first stars. Additionally, they have the

potential to affect the final fates of the stars in which they occur. By better understanding these interactions, we can gain new insights in the fields of early cosmic chemical evolution, galactic archaeology and stellar physics as a whole.

1.2 The Evolution of Single Stars

The study of the evolution of single stars requires ingredients from many fields of physics including but not limited to, atomic physics, hydrodynamics, nuclear physics, magnetodynamics, thermodynamics, particle physics, and special and general relativity. The relevant physical scales range from the subatomic to millions of kilometers. Telescopes allow observers to obtain and tease out information previously unknown about stars. If we want to fully understand this data we obtain through observations, we must explain them through physical models. This is what is done in the fields of theoretical and computational stellar astrophysics. Kippenhahn & Weigert (1990), Iliadis (2007) and Hansen & Kawaler (1994) were utilized in writing this section.

1.2.1 Governing Equations

In this section I will outline the equations needed to construct a stellar model. These include the equation for hydrostatic equilibrium, the equations for mass and energy conservation, the equation for energy transport and finally the equation for evolution of nuclear species. These equations allow us to model stars and gain insights into their interior evolution and are supplemented with other equations describing various physical processes. For example, a model of convection, an equation of state, opacity tables and a nuclear reaction network are all required.

Assuming spherical symmetry, and hydrostatic equilibrium, the governing equations for the evolution of single stars can be written in Lagrangian form as follows:

$$\frac{\partial P}{\partial m} = -\frac{Gm}{4\pi r^4} \tag{1.1}$$

Where P is the pressure, m is the Lagrangian mass coordinate and G is the gravitational constant. We assume for most of a stars life this equation holds true. This tells us that the gravitational force on one element of star 'fluid' is perfectly balanced by pressure and there is no local acceleration.

Eq. (1.2) Is the mass conservation equation. All variables are the same as in Eq. (1.1) with the addition of the density, ρ. This equation as is assumes a steady state and often another term must be added to account for mass-loss, which is a critical component in the evolution of most stars.

$$\frac{\partial r}{\partial m} = \frac{1}{4\pi r^2 \rho} \tag{1.2}$$

Eq. (1.3) Is the energy conservation equation. It says that a change in luminosity, l is due to: $\epsilon_{\rm nuc}$ or energy generated through nuclear reactions, ϵ_ν, or energy lost via neutrinos, and $\epsilon_{\rm g}$, or gravitational energy changes through expansion or contraction.

$$\frac{\partial l}{\partial m} = \epsilon_{\rm nuc} - \epsilon_\nu + \epsilon_{\rm g} \tag{1.3}$$

Eq. (1.4) is the equation for energy transport. T is the temperature, κ is the Rosseland mean opacity and a and c are the radiation constant and speed of light, respectively.

$$\frac{\partial T}{\partial m} = \frac{GmT}{4\pi r^4 P}\nabla \text{ , where } \nabla = \begin{cases} \nabla_{\rm rad} = \frac{3}{16\pi acG}\frac{P\kappa l}{mT^4} \\ \nabla_{\rm ad} + \nabla_{\rm S-ad} \end{cases} \tag{1.4}$$

Here, $\nabla_{\rm rad}$ is the radiative temperature gradient, which describes the spatial temperature gradient within a star where heat is transported by radiation. $\nabla_{\rm ad}$ is the adiabatic temperature gradient and describes the change in temperature within an adiabatic fluid element. $\nabla_{\rm S-ad}$, the superadiabatic temperature gradient is the difference between the true temperature gradient and the adiabatic temperature gradient (i.e., if large, convection is not efficient enough to transport all heat). If $\nabla_{rad} < \nabla_{ad}$ the region of interest is stable against convection. This is known as the *Schwarzschild criterion* for convection.

The final equation, Eq. (1.5), describes the change in mole fraction of a given isotope, Y_i, in time due to nuclear reactions which both produce and destroy it. Here λ_{kj} and λ_{jk} are the forward and reverse reaction rates. This equation only explicitly includes two-body reactions and can easily be appended for single and multi-body reactions.

$$\frac{\partial Y_i}{\partial t} = \sum_{j,k} Y_l Y_k \lambda_{kj}(l) - Y_i Y_j \lambda_{jk}(i) \tag{1.5}$$

1.2.2 Timescales

Another series of equations which are invaluable in our understanding of stars, relate to the timescales in which different processes and evolutionary phases take place. These timescales tell how quickly a star can return to an equilibrium state due to various internal processes. This is by no means an exhaustive list, but rather the most important and commonly used timescales for understanding the global evolution of stars. A theorist can in principle construct timescales for many physical processes of

interest within a star. Some of the timescales presented here are a result of the virial theorem, which states the relationship between the internal energy and gravitational potential energy of a star. For a general equation of state the virial theorem can be written:

$$E_{int} = -\frac{1}{3}\phi E_{grav} \tag{1.6}$$

Where E_{int} is the total internal energy of the star, E_{grav} is the total gravitational energy and ϕ describes the relationship between pressure and internal energy of the stellar material. For and ideal gas $\phi = 3/2$, and for pure radiation $\phi = 3$.

From the virial theorem we can estimate the thermal timescale of a star. The thermal timescale, also known as the Kelvin-Helmholtz timescale for a star, is the timescale in which a star adjusts when thermal equilibrium is perturbed. More explicitly, it is the evolutionary timescale for a contracting star and is estimated as follows:

$$\tau_{KH} \approx \frac{GM^2}{2R} \tag{1.7}$$

In the above equation all variables have their typical meaning: G is the gravitational constant, M is the total mass and R is the total radius. Another important timescale is the dynamical timescale, or the timescale in which a star reacts to a departure from hydrostatic equilibrium (Eq. (1.1)).

$$\tau_{dyn} \approx \sqrt{\frac{R^3}{GM}} \tag{1.8}$$

For a star in thermal equilibrium, the luminosity leaving the star is in balance with the energy created by nuclear reactions, $L = -dE_{nuc}/dt$. The nuclear timescale is the timescale in which this equilibrium can be maintained and is written as follows:

$$\tau_{nuc} = \frac{E_{nuc}}{L} \tag{1.9}$$

Finally, a star which has suddenly lost all pressure support will collapse on the free-fall timescale shown in Eq. (1.10). This timescale is important for understanding the death of massive stars which is described in 1.2.4.

$$\tau_{ff} = \left(\frac{R}{g}\right)^{(1/2)} \tag{1.10}$$

1.2.3 Nucleosynthesis

The major energy source acting against gravity within stars is nuclear fusion[1]. All elements in the Universe beyond those which existed after the Big Bang were created within the stars through nuclear fusion, fission and other decay processes, cosmic ray spallation, and photodisintegration, these processes are collectively termed nucleosynthesis. Here I will review some of the basics of stellar nucleosynthesis, focusing mainly on nuclear fusion, which is the main mode by which most of the elements in the universe are made. More specifically, most of the metals up to Fe we observe (by mass) were created through charged-particle reactions. Elements heavier than Fe are created primarily by neutron-capture reactions.

The deep interiors of stars are composed of a combination of charged particles, neutrons and nuclei. Charged-particle reactions occur when the mean kinetic energy (hence also being called *thermonuclear* reactions) of the gas, which can be represented by a Maxwell-Boltzmann distribution, is such that the charged particles are able to penetrate the Coloumb barrier of another charged particle or nucleus. This happens through quantum mechanical tunneling and for each reaction there is a probability of this tunneling taking place at a given temperature. The total reaction rate for a charged-particle reaction between two particles labelled particle "0" and particle "1" is:

$$r = \frac{1}{1+\delta_{01}} Y_0 Y_1 N_A \langle \sigma v \rangle_{01} \tag{1.11}$$

Which has units of reactions per $\mathrm{cm}^{-3}\,\mathrm{s}^{-1}$. Here δ_{01} is the Kroneker delta symbol, which accounts for the possibility that two particles are the same. Y_0 and Y_1 are the mole fractions of the two interacting particles, N_A is Avogadro's number and $\langle \sigma v \rangle_{01}$ tells us the probability of the reaction occurring and is given by:

$$\langle \sigma v \rangle_{01} = \left(\frac{8}{\pi \mu_{01}} \right)^{1/2} \frac{1}{kT^{3/2}} \int_0^\infty E \sigma(E) e^{-E/kT} dE \tag{1.12}$$

Where σ is the effective cross-sectional area and μ is the reduced mass , $M_0 M_1/(M_0 + M_1)$.

For neutron capture reactions the cross-section, and therefore the reaction rate, is typically proportional to $(1/\sqrt{E})$. Reaction rates are determined either experi-

[1] This is where the ϵ_{nuc} term in Eq. (1.3) comes from

mentally in laboratories or using theoretical models (e.g. Hauser & Feshbach (1952); Rauscher & Thielemann (2000)).

There are several reaction groups which are important for understanding the basics of stellar nucleosynthesis as discussed in this thesis.

pp chains: The pp (proton proton) chains take place to some extent in all H-burning environments and are the most important source of energy in low mass main sequence stars, such as our Sun. pp chains include various low-temperature reactions and ultimately to convert H to He.

CNO: The CNO cycles are a group of reactions that take place within the H-

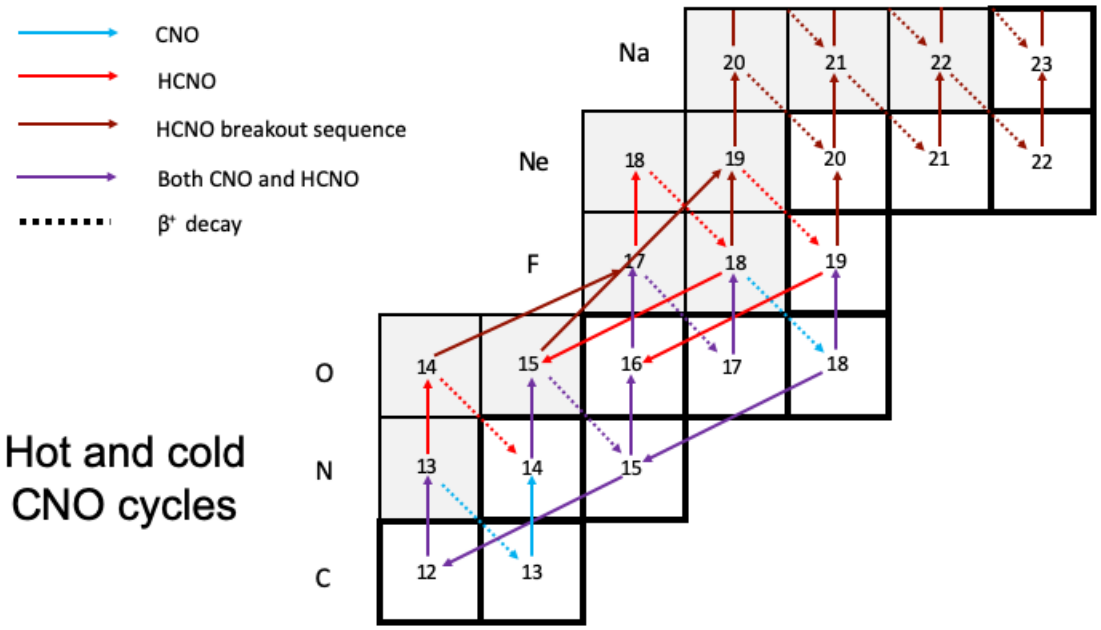

Figure 1.1: The CNO and hot CNO cycles. Breakout reactions are shown here are representative of what occurs in Pop III stars. See Chapter 3 for further details.

burning cores and shells of stars with zero-age main sequence (ZAMS) masses of $\sim 2\,M_{\odot}$. These cycles act ultimately convert H to He with C, N and O facilitating the conversion. There are three CNO cycles that occur within stars, called CNO1[2], CNO2 and CNO3 and which are active depends on the temperature and density conditions. In addition, hot CNO cycles can occur when conditions are extreme enough. Hot CNO cycles are different because they are limited not by the slowest charged particle capture, as is the case with classic CNO cycles, but rather by the

[2]Also called the CN cycle.

decay time of unstable species. Hot CNO cycles are discussed further in Chapter 3. Fig. 1.1 shows both the CNO1 and hot CNO1 cycles.

triple-α: The triple-α occurs during He burning in all stars. Through this reaction three He nuclei are converted to ^{12}C. Other important reactions during He burning include α captures onto C, O and Ne.

***s*-process**: The *s* process or slow neutron capture occurs in either what is called the ^{13}C pocket in intermediate mass AGB stars or in core or shell He burning in massive stars. The neutron source is either the $^{13}\mathrm{C}(\alpha,n)^{16}\mathrm{O}$ reaction or the $^{22}\mathrm{Ne}(\alpha,n)^{25}\mathrm{Mg}$ reaction, (generally) respectively. The main characteristic of *s*-process nucleosynthesis is the fact that is is *slow* enough that β^- decays of unstable species generally occur faster than neutron captures. This leads to a reaction flow staying near the *valley of stability*[3], as can be seen in Fig. 1.2. Typical neutron densities are from $Nn \sim 10^6 - 10^{12}\,\mathrm{cm}^{-3}$ (Käppeler et al., 2011)

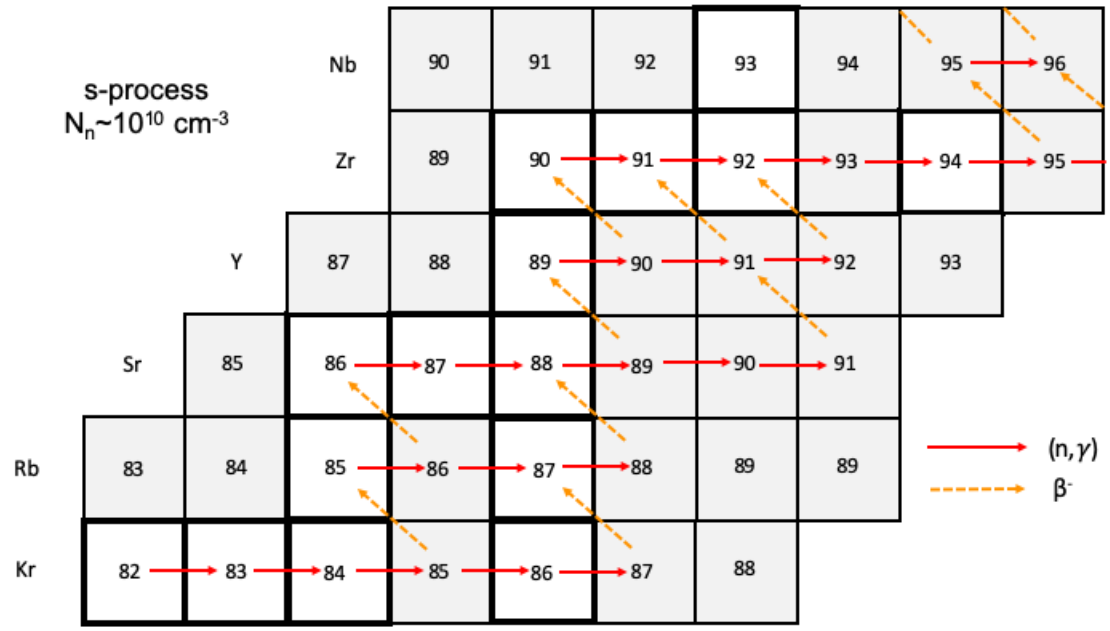

Figure 1.2: *s*-process path typical of neutron densities of around $10^{10}\,\mathrm{cm}^{-3}$. White squares indicate stable isotopes and grey show unstable isotopes.

***r*-process**: The *r* process or rapid neutron capture process occurs in extreme environments with high neutron number density. Typical neutron densities are $Nn \gtrapprox$

[3]The valley of stability refers to the lowest part of the valley-like shape created when plotting the number of protons and neutrons against the stability of each isotope or binding energy

$10^{20}\,\mathrm{cm}^{-3}$ (Arnould et al., 2007). We now have evidence for the r process taking place in neutron star mergers (Pian et al., 2017), though we cannot rule out the other main theoretical site, core-collapse supernovae.

i-process: The i process has neutron densities *intermediate* between those of the classical r or s processes ($Nn \sim 10^{13} - 10^{16}$). This process was first described in detail by Cowan & Rose (1977) (See also Starrfield et al., 1975). All suggested i process sites have the $^{13}\mathrm{C}(\alpha, n)^{16}\mathrm{O}$ reaction as the neutron source and rely on a *convective-reactive* environment, where the timescale of convection is similar to the relevant nuclear timescale, to create the necessary conditions for this reaction. Possible sites identified so far are: AGB and Post-AGB stars (Dardelet et al., 2014; Hampel et al., 2016; Herwig et al., 2011), super-AGB stars (Jones et al., 2016), He-shell flashes in low-mass stars Cowan & Rose (1977), rapidly-accreting white dwarfs (Denissenkov et al., 2019) and as I will show in this thesis, H-He interactions in Pop III stars.

There are other important sites and processes which are significant in contributing to galactic chemical evolution as well. For example, Type Ia supernovae supply most of the galactic Fe-group elements. Additionally, late stage shell and explosive burning in core-collapse supernovae, which creates most of the so-called α elements in our galaxy.

1.2.4 Evolutionary Phases

Below I describe the main evolutionary phases for stars depending on initial mass. While this is the dominant factor in understanding the life and death of a star, other factors can have important consequences such as metallicity and mass-loss rates, which I neglect below.

Pre-Main Sequence: Neglecting the details of star formation, the earliest stage of a stars life is called the pre-main sequence. During the pre-main sequence phase, the star has settled in mass (i.e. it is no longer accreting material/fragmenting etc.). Such a star is contracting and increasing in temperature. It's luminosity comes from this gravitational contraction with a small amount of nuclear burning. A pre-main sequence star does not begin by burning H, but rather burns fragile nuclei such as ^{2}H, ^{3}He and subsequently ^{7}Li. The pre-main sequence phase lasts anywhere from around 10^5 to over 10^7 yrs, the time being dictated by the mass, radius and luminosity of the young star.

Main Sequence: After the pre-main sequence, the star has contracted such that

the central temperature is high enough to begin fusion of H in the core, which marks the beginning of the longest phase of a star's life, the main sequence phase. This phase is indicated by the leftmost, or bluest, region for each star on the Hertzsprung-Russell diagram (Fig. 1.3), where the line is thicker. Due to the amount of time spent in this evolutionary stage, most stars in the sky are main-sequence stars, as is our own Sun. For stars above $\sim 2\,M_\odot$, H burning proceeds through the CNO cycle and for low-mass stars like our Sun H is burned through what are called $p-p$-chains. Both of these are a series of nuclear reactions which ultimately convert H into He. One of the main differences between these two cycles is the temperature sensitivity. Energy generation from $p-p$-chains are $\propto T^4$ whereas for the CNO cycle energy generation is $\propto T^{18}$. Due to this, massive stars have convective cores while stars around the mass of the sun have radiative cores. ∇_{rad} becomes large when either κ, the opacity is large or when the energy flux to be transported becomes large, or l/m, which can be seen in Eq. (1.4). After the main sequence, stars will either become what are considered giant or sub-giant stars, which are described below.

Post-Main Sequence: Massive stars continue through several more evolutionary phases during their lives. After the main-sequence comes the He-core burning phase. During this time, the surface temperature of the star decreases due to expansion, with a near constant luminosity. The main nuclear reaction in He burning is the triple α reaction. Once the core He is exhausted, a C-O core forms and C burning then takes place. This is then followed by O burning, Ne burning and Si burning. At the end of the star's life you are left with an onion-like structure of burning regions surrounded by the H envelope. This is displayed in Fig. 1.4. Unlike lower mass stars, the colour-magnitude evolution of massive stars is less illuminating regarding the internal structure of the star. In general, high-mass stars evolve redward during the post-MS evolution, shown in Fig. 1.3 for the $25M_\odot$ star. From a theoretical perspective, the details of the evolution on the HR diagram during the final phases of the star's life relies on the details of the particular model.

Low- and intermediate- mass stars take different evolutionary routes. For low mass stars, the core is electron degenerate and inert as it moves along the sub-giant branch and RGB. The core increases in mass due to H-shell burning and the star undergoes the He flash, whereby He burning begins. During core-He burning these stars are located on the Horizontal branch. After core-He burning these stars enter the Asymptotic Giant branch phase. During the AGB phase, the star has degenerate C-O core and burns He and H in the shells above. The AGB phase is marked by

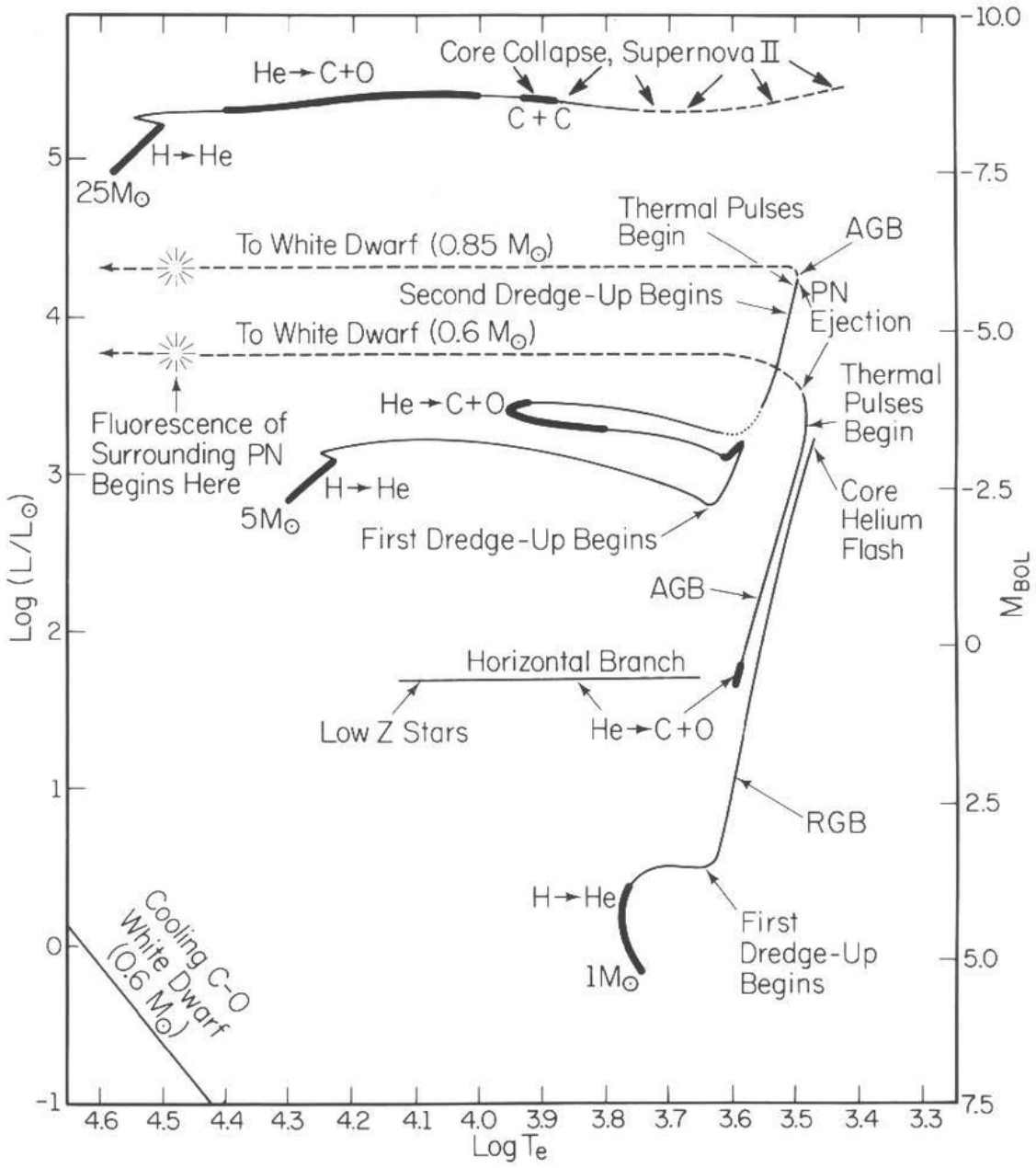

Figure 1.3: Hertzsprung-Russell diagram showing evolutionary tracks for stars of various masses. Image from Iben (1985).

strong mass loss. These primary phases are all indicated in Fig. 1.3.

Death: Again, depending on initial mass, the final fate of massive stars can have a variety of outcomes. For low mass and intermediate mass stars, after the AGB phase the star will transition to a planetary nebula—a misnomer for a white dwarf

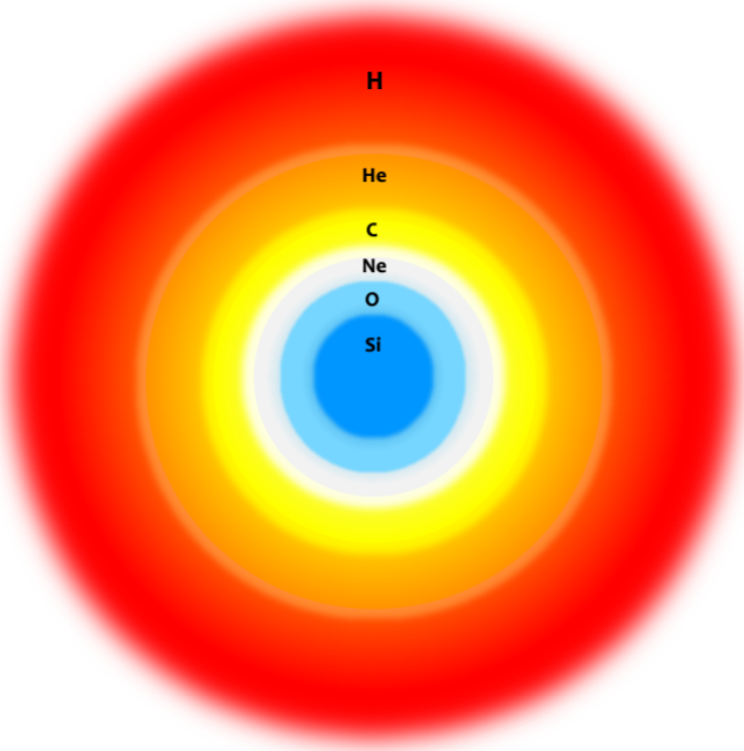

Figure 1.4: Slice-through schematic displaying the internal structure of the final stages of a massive star's life. Not to scale.

surround by an expanding shell of ionized stellar material. Eventually all the envelope material will be blown off the star and it will end up as a white dwarf; slowly cooling for billions of years.

Massive stars die as core-collapse supernovae or collapse directly into a black hole. There is great debate over which massive stars will die in which way, which is further discussed in 1.3. Most of the debate stems from uncertainty in various input physics and our incomplete understanding of the supernova engine. During the final hours of a massive star's life, silicon burning converts silicon and sulfur to primarily Fe and Ni. At this time, the temperature and density of the core steadily increase, and fusion ceases as the binding energies of Fe and Ni are too high to be overcome at even the now very high stellar temperatures (4×10^9 K). The core continues to grow and ccontract until eventually its mass exceeds the Chandrasekhar mass limit, which is the maximum mass that can be supported by electron degeneracy pressure and collapses on the free-fall timescale, Eq. (1.10). During this time, photodisintegration and

electron captures occur, which are endothermic and contribute to loss of degenerate pressure, respectively, and further accelerate the collapse. The core density momentarily surpasses the nuclear density ($\rho \approx 10^{14}\mathrm{g\,cm^{-3}}$), and nuclei and nucleons begin behaviour as dictated by the strong nuclear force. This creates a sudden halting and rebound of the core, which then propagates a shock through the core. This shock eventually will lose its kinetic energy and stall. The details of how the shock then revives and cause the star to explode are still a topic of ongoing research. The most favoured mechanism is currently the neutrino-driven explosions (Janka et al., 2016). The shock then leads to nucleosynthesis in the stellar material as it passes through—a process known as explosive nuclear burning.

Core collapse supernovae can be classified observationally based on their spectral signatures. Type II are dominated by hydrogen lines with some Ca, O and Mg present. There are several subclasses of Type II supernovae which are differentiated by the morphology of their light curves. In this thesis, Type IIn are briefly discussed; these supernova show both narrow and broad emission lines which are believed to be due to strong mass loss events depositing high-density gas around the star shortly before the supernova explosion. Supernovae Type Ib have weak hydrogen lines and strong helium lines. Ic have weak lines for both. Both show O, Ca and Mg. These are interpreted to be from stars which lost their H envelope due to strong sustained mass loss.

1.2.5 Stellar Hydrodynamics Simulations and the `PPMStar` Code

1D stellar evolution simulations generally conform to assumptions presented in Eq. (1.1) – Eq. (1.5). Mixing of nuclear species is critical to the overall evolution and nucleosynthesis within stars. In 1D models, the mixing of species is assumed to occur via a diffusive process. Energy is transported according to Eq. (1.4), using results from mixing length theory (MLT), which is a 1D theory of convective mixing. The *convective-reactive regime* exists when the mixing timescale becomes comparable to the relevant timescale for nuclear reactions, which is dictated by the shortest timescale of a reaction that is either important for nucleosynthesis or energetics. In this regime, these assumptions no longer apply and one must turn to 3D hydrodynamic simulations to gain a better understanding of both mixing and nucleosynthesis. Apart from the convective-reactive regime, 3D simulations are also used in understanding core

collapse supernovae (e.g., Janka et al., 2016), Type Ia supernovae (e.g., Seitenzahl et al., 2013), novae (e.g., Casanova et al., 2011) and convection (and its effects) in general (e.g., Cristini et al., 2017). The common thread between all of these simulations and their respective regimes is that MLT is especially limited in its predictive ability in these scenarios.

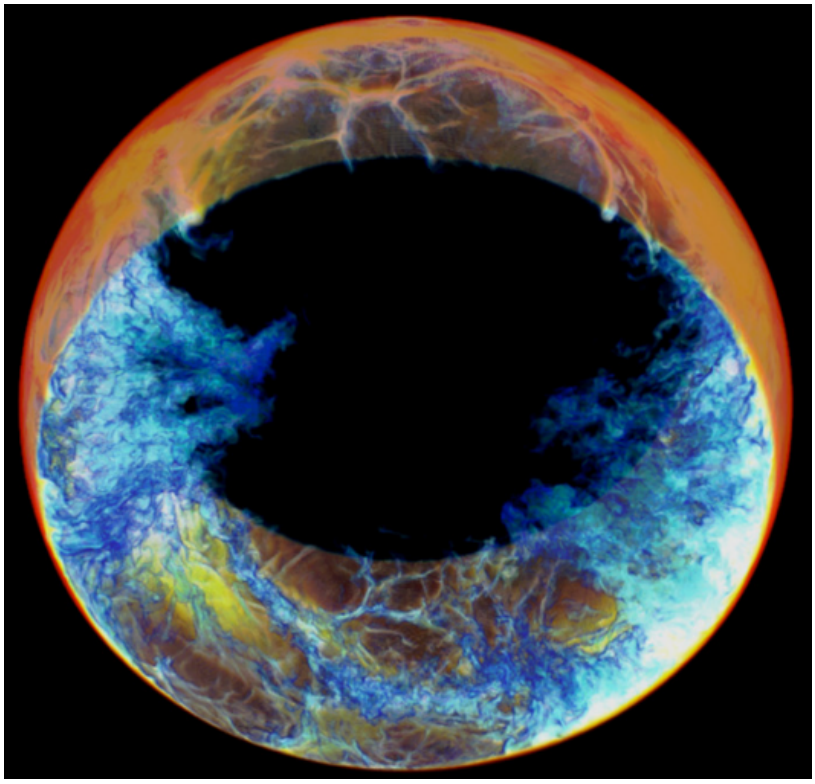

Figure 1.5: Partial layer of a full-sphere `PPMstar` simulation from Woodward et al. (2015) showing fractional volume of H-rich fluid as it is entrained in to He-rich zone below.

The `PPMStar` code developed by Paul Woodward was used in this thesis and has been utilized to investigate a range of stellar convection regimes. An example of one such regime is shown in Fig. 1.5, which shows H mixing into a He-rich layer during the He-shell flash in a $2\,M_\odot$ AGB star. For typical stellar interiors the Euler equations can be used as the flow is effectively inviscid[4]. The `PPMStar` code uses a more accurate variant of the Piecewise Parabolic Method (PPM) (Colella & Woodward, 1984) called the Piecewise Parabolic Boltzmann method (PPB) (Woodward et al.,

[4]In reality, a very small amount of viscosity is present in a fully-ionized gas due to Coulomb interactions between ions (Eq. 5-54 in Spitzer, 1962)

2008). These are similar but slightly different numerical schemes to solve the fluid equations, advecting fluid from one computational cell to another.

Because the `PPMStar` code uses an explicit solver method, the flow must satisfy the Courant–Friedrichs–Lewy (CFL) condition, which states that for every spatial dimension, the timestep is limited by the distance the flow can travel relative to a grid cell size. The flows considered in this work are typically low-Mach number flows ($\mathrm{Ma} \sim 10^{-4} - 10^{-2}$). The mach number is the velocity of the flow relative to the local sounds speed, therefore these flows are *subsonic*. Because of the low velocities, the *driving luminosity*—a constant luminosity included at the base of the convection zone meant to mimic the energy generation from nuclear reactions—may be increased in order to satisfy the CFL condition. In stellar hydrodynamics simulations, simplified networks are required as the computational cost of solving for the time evolution of species (Eq. (1.5)) in three dimensions along with the flow contemporaneously becomes quickly prohibitive. This is particularly true for high resolution and/or full 4π spherical simulations, which are not always used. In the `PPMStar` code discussed in 4, a single-reaction network is typically used though there exists examples of larger networks (e.g. Mocák et al., 2018; Couch et al., 2015; Eiden et al., 2020).

1.3 Population III

1.3.1 Birth of the First Stars

Shortly after the Big Bang, elementary particles were created and within minutes Big Bang nucleosynthesis created the lightest nuclei, (Cyburt et al., 2016). At this point in time, the young Universe was a hot, dense plasma, where the mean-free-path of photons was so short they rapidly scattered off matter particles rather than travel freely. Recombination—the cosmological epoch in which atoms were first neutral—took place around redshift ~ 1100 (Ryden, 2003), which corresponds to about 375,000 yrs after the Big Bang. Once the temperature cooled enough for recombination to take place, photons were able to travel relatively uninterrupted. The time immediately following Recombination is known as the Dark Ages, named such due to the fact that we have very little information as to what went on during it. In this time, photons were able to travel but there were few processes apart from the hyperfine transition of neutral hydrogen could create them, hence the era was 'dark'.

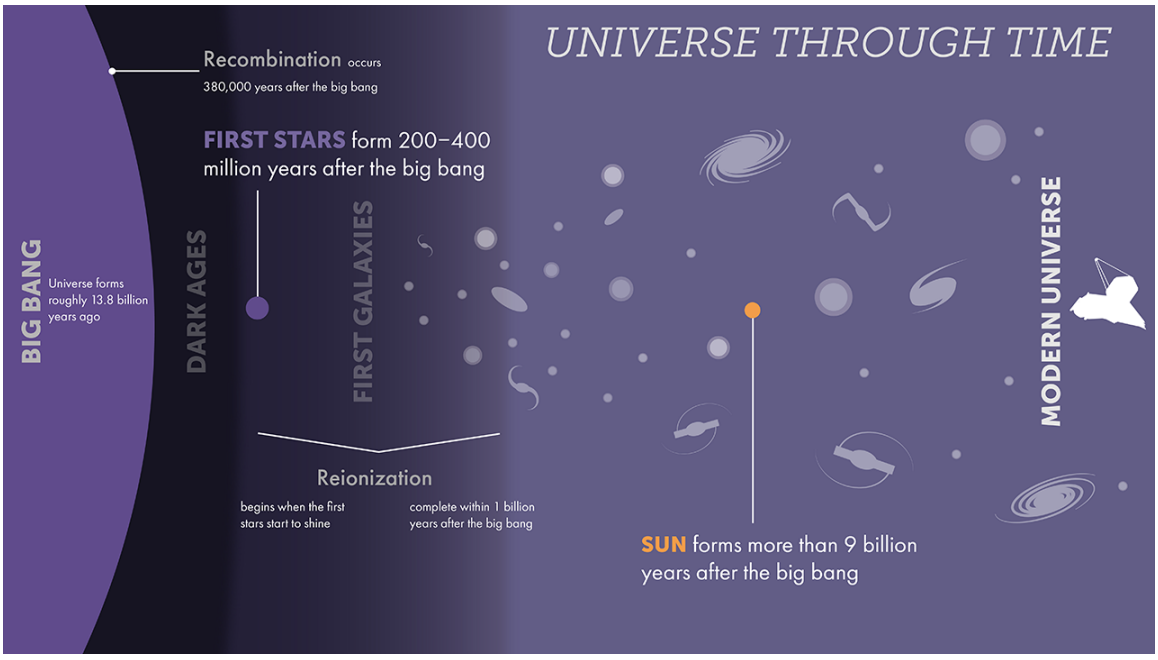

Figure 1.6: The history of the Universe. Image credit: STScI.

During the Dark Ages, it is believed that the first dark matter halos began to collapse when the Universe was between $100 - 200\,\mathrm{Myr}$ old (Reed et al., 2007). It is within these first overdense collapse events in dark matter halos of $\sim 10^6\,\mathrm{M}_\odot$ that we

believe the first stars were born.

It has long been theorized that the first stars were more massive than their modern day counterparts. This was first proposed in order to understand the chemical evolution of the Milky Way (Truran & Cameron, 1971). Modern simulations including more sophisticated physics, such as collisional emission and heating from H_2 formation, suggest that Pop III stars were typically $\sim 10 - 100\,M_\odot$ (Hirano et al., 2014; Stacy et al., 2016; Turk et al., 2009). These stars are often thought to have formed first in isolation as single stars Bromm & Yoshida (2011), and only later as halos merged to from galaxies (Fig. 1.7).

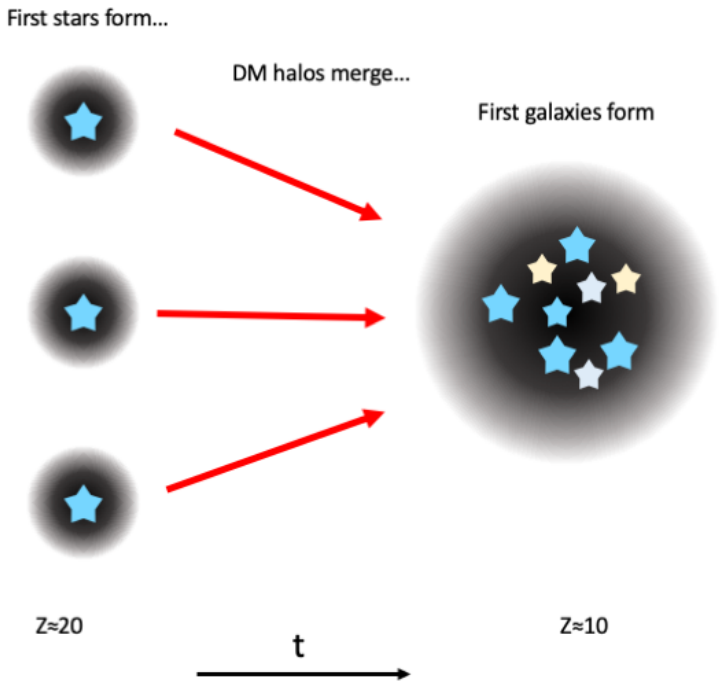

Figure 1.7: Cartoon representation of the formation of the first stars and galaxies.

Reionization was likely a gradual process that lasted around 1 Gyr (Miralda-Escudé et al., 2000) with first stars and galaxies likely being the primary source of ionizing radiation (Barkana & Loeb, 2001), followed perhaps by quasars. Assuming our estimations of the Pop III IMF are correct, the first stars were likely to have died within millions of years of their formation. Only very low mass Pop III stars could have survived until the present day and one has yet to be identified. As the first massive stars died, they would have enriched the surrounding gas with metals until dust cooling could become efficient and low-mass stars would start to dominate. The

critical metallicity for the IMF to transition to a Population II IMF is Z_{crit} 10^{-6}-$10^{-3.5} Z_{\mathrm{M}_\odot}$ (Wise et al., 2012). The details of the transition remain unclear but it seems to have ended around a redshift of 6 (Robertson et al., 2015), or around 1 billion yrs after the Big Bang.

1.3.2 Lives and Deaths of the First Stars

There are several notable differences between Pop III stars and all later stars. Based on theory and the observation of the lowest metallicity stars seen in the Milky Way halo today, we believe Pop III stars were likely more massive, hotter, and more compact than higher metallicity stars. They also were unlikely to have experienced significant mass-loss.

As stated previously, Pop III stars were massive and formed from gas composed of H, He and Li and all of the aforementioned differences are a direct result of the initial composition. In stars of higher metallicity, during the main sequence (MS) phase $p-p$ chains are the dominant mode of energy generation for stars $\sim 0.8-2\,\mathrm{M}_\odot$ and the CNO cycles dominate at all masses greater. Given the likely top-heavy[5] IMF, one would expect Pop III stars to use the CNO cycle as their main source of energy during the main-sequence, and this is absolutely true. The difference is that due to not having any CNO catalysts initially, massive Pop III stars start burning H through $p-p$ chains (Ezer & Cameron, 1971). Since the energy liberated in these reactions is insufficient to counter the effects of gravity, the star continues to contract until high enough central temperatures are reached, producing a small amount of catalyst. This is achieved via the triple α reaction, which produces C. C is produced in very small amounts, about $X_{^{12}\mathrm{C}} = 10^{-9}$, which is just enough to sustain the CNO cycle. Due to the aforementioned, simulations predict that massive Pop III stars have higher H-burning temperatures than their higher-metallicity counterparts. This is also partly responsible for the high densities seen in simulations of Pop III stars. This higher-temperature hydrogen burning occurs in both the core and shell of the stellar model.

Another result of the initial metal-free composition is a lowered opacity. In stellar matter, the opacity, $\kappa\,[\mathrm{cm}^2\,\mathrm{g}^{-1}]$, will dictate how large the temperature gradient should be to transport energy by radiation (see Eq. (1.4)). In general, an high opacity leads to increased heat and gas pressure via momentum transfer, which will cause

[5] More massive stars than low mass stars compared to present day

affected layers to expand. In higher-metallicity stars, a large source of opacity is the presence of iron and other heave elements, as they have a higher effective cross-sectional area with more available electron energy states. Opacity increases with decreasing temperature and has the most noticeable effects in the stellar envelope. In Pop III stars, having a metal-free envelope leads to low opacities with high surface temperatures, and a retained compact structure resulting from the extra contraction on the main-sequence as mentioned above.

Having a metal-free envelope also will lead to either little or no mass loss in Pop III stars. Currently, we do not understand mass-loss well enough to have ab initio models, but rather empirical fits are typically used. Despite the uncertainties, we do understand that a major source of mass loss in massive stars is line-driven winds (Kudritzki & Puls, 2000; Smith, 2014). Unless sufficient metals can be transported to the stellar surface, Pop III stars are unlikely to experience a significant amount of mass loss during their lives due to this effect (Krtička & Kubát, 2006). In addition continuum-driven winds(those arising from electrion scattering and bound-free transition) may not play a influential role in Pop III stars(Ibid.). This ultimately alters how these stars will die (see Heger et al., 2003).

The details of the final fates massive stars are currently uncertain, let alone that of massive Pop III stars. In general, our understanding of the death of the first stars is displayed in Fig. 1.8.

Fig. 1.8 is a general guideline based on 1D calculations and does not account for physics effects which we know to be important such as neutrino-heated winds (see Heger et al., 2003). As discussed in 1.2.4, our predictive abilities regarding the ultimate fate of massive stars is still quite limited.

Briefly, stars of much higher mass than those considered in this thesis ($10^4 - 10^6\,M_\odot$) may contribute to black hole formation during the Epoch of Reionization either through mass accretion or direct-collapse of very massive stars (Bromm & Yoshida, 2011). These extremely short lived stars may have been the seeds to create the super massive black holes which now reside at the center of most galaxies (Woods et al., 2020).

1.3.3 The second stars

While the first stars in Universe remain elusive, the next generation of space-based telescopes, such as the James Webb Space Telescope (JWST), promise to provide

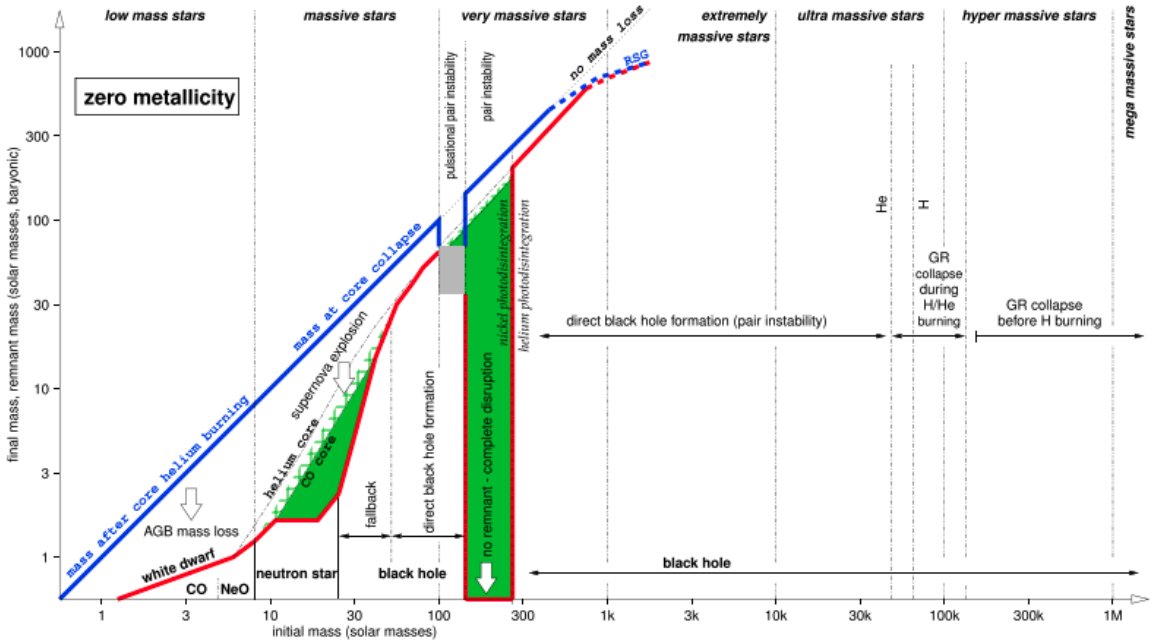

Figure 1.8: Final fate of massive Pop III stars by mass. From Woods et al. (2020)

important information regarding their lives and deaths. Currently, some of our best means of investigating the first stars involves observing the second generation of stars containing the chemical fingerprints of their predecessors. Simulators then either match this observational data to their predictions, or use it to constrain their model outcomes.

Metal poor stars are stars with less overall metals than found in our Sun. Metal-poor stars can potentially provide us with a great deal of information regarding the formation and evolution of our Milky Way Galaxy (and surrounding satellites). Stars with very low metallicities can also reveal information about individual nucleosynthetic events and can therefore both act as a diagnostic for nuclear astrophysics and have the potential to illuminate the nature of the first stars. Metal-poor stars are classified by their Fe content, thereby using Fe as a proxy for metals. There are very, extremely, ultra, hyper and mega metal-poor stars with [Fe/H][6] from < -1 to -6 (Beers & Christlieb, 2005). The typical assumption is that the lower down a star goes in metallicity, the more pristine it may be.

Carbon Enhanced Metal-Poor (CEMP) stars are stars with sub-solar (i.e., lower than the Sun) iron abundance and super-solar carbon abundance, more specifically [Fe/H] < -1 and [C/Fe] >1 (Beers & Christlieb, 2005). CEMP stars are often broadly

[6] $[A/B] = \log(A_*/B_*) - \log(A_\odot/B_\odot)$

classified into three groups: CEMP-s, with signatures of s process enhancement, and CEMP-no stars which have no overbundance (relative to the Sun) of either the s or r processes, and CEMP-r/s which contain signatures of both s and r process enhancement. Some CEMP-r/s stars may contain a superposition of both processes, Beers & Christlieb (2005) as was originally hypothesized and some may carry the signatures of the i process(Dardelet et al., 2014).

CEMP-s stars are believed to carry the abundance signatures of the s process from mass-transfer onto a binary companion. A significant fraction of CEMP-s stars have indeed been found to have signatures of binarity. Self-enrichment scenarios, where the observed chemical abundances come from within a single star itself, have also been suggested for these stars (e.g., Campbell et al., 2010).

CEMP-r/s (r+s, i) stars have signatures of both the s process and r process (based on Ba and Eu abundances). It has been suggested that some of these stars are the result of certain binary systems which could produce both signatures (Beers & Christlieb, 2005, and references therein). More recently, it has been found that some of these stars can't be explained by the superposition of the two processes (Roederer et al., 2016), and in this case, the i process becomes a likely candidate. Some of these stars have been matched to theoretical predictions of the i process (Denissenkov et al., 2019; Dardelet et al., 2014; Hampel et al., 2016). More theoretical and observational work is needed to disentangle this class of CEMP stars.

CEMP-no abundances are thought to be the nucleosynthetic result of core-collapse supernovae (CCSNe) in early-generation massive stars. As stated, these stars have no *overabundance* of either s or r process signatures, meaning that rather than not having any signatures, they don't have an overabundance as compared to the solar ratios. The abundances in CEMP-no stars have been typically attributed to core collapse supernova in early generations of massive stars Nomoto et al. (2013) and it has been suggested that the lower in [Fe/H] one goes, the more likely the chemical abundances observed are the result of a single first generation progenitor Frebel & Norris (2015). Arentsen et al. (2019) found that $\approx 32\%$ of a sample of 23 CEMP-no stars have radial velocity variations that suggest binarity. At this point it is unclear what role mass transfer may have played in the evolution and observed abundance patterns in these stars (i.e, how many were/are interacting binary systems).

CEMP-no stars are further divided into three sub-categories based on their apparent morphological groupings in C and Fe phase space. This is shown in Fig. 1.9. Groups I and II are reasonably well reproduced by CCSNe yields (Placco et al., 2016).

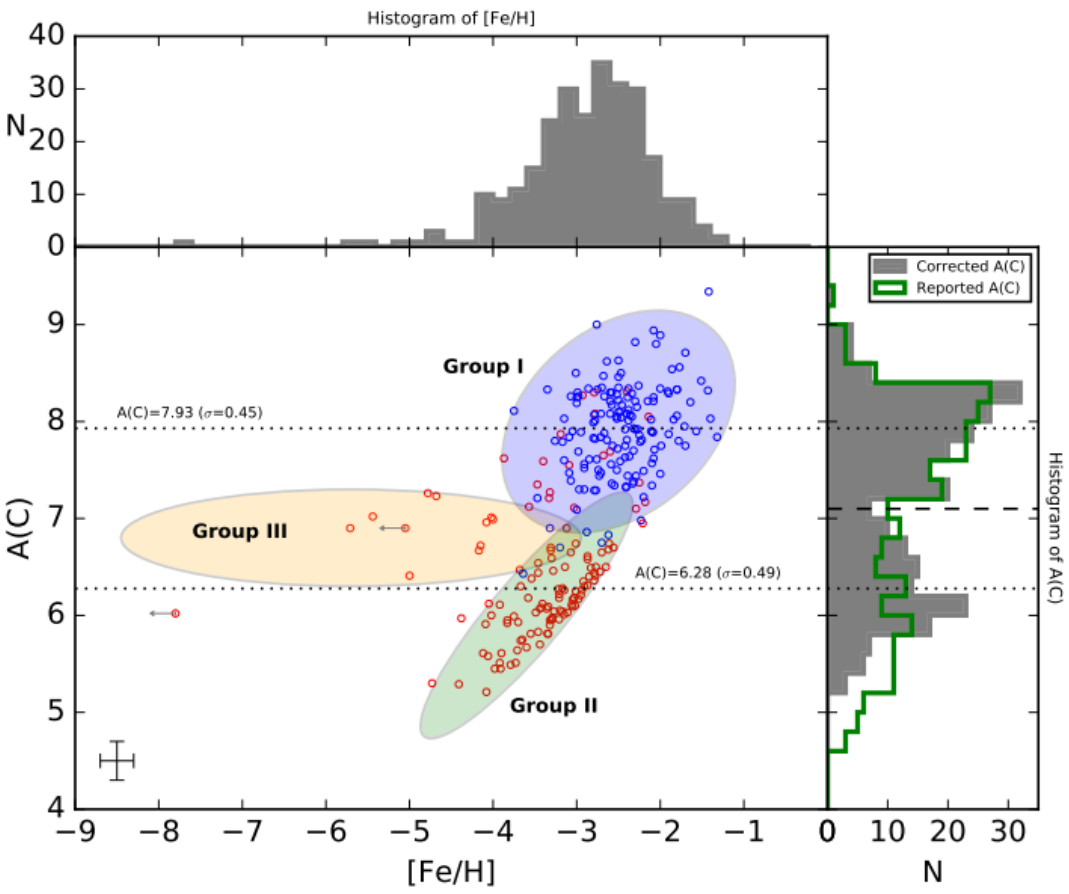

Figure 1.9: CEMP-no subclasses based on absolute C abundance and [Fe/H] from Yoon et al. (2016). Figure reproduced by permission of the AAS.

Group III CEMP-no stars, which are less common than the other groups and have lower Fe content, are not as well reproduced as is shown in Fig. 1.10. Part of the problem involves the *light-element abundance pattern*. This can be seen in stars HE 0107-5240, HE 1327-2326, HE 2139-5432 and HE 0057-5959 in Fig. 1.10 from Na-Si. These stars specifically exhibit higher [Na/Mg] ratios than are typically predicted by faint-supernova models.

Since these stars have very little Fe-group elements as compared to predictions from standard SNe models, 'faint' or 'low-energy' supernovae (SNe) models are often invoked to explain them. There have also been suggestions that these stars are the result of rapidly rotating massive stars with low (but non-zero) initial metallicity Choplin et al. (2016). Thus far, the models have been made to reproduce these stars but often do not mention how they can create the light element abundance

patterns discussed above, if they are able to (see Takahashi et al., 2014; Limongi et al., 2003; Umeda & Nomoto, 2003). Recent galactic chemical evolution models including inhomogenous mixing suggest that only Group II CEMP-no stars can be easily explained by faint or mixing and fallback SNe models (Komiya et al., 2020).

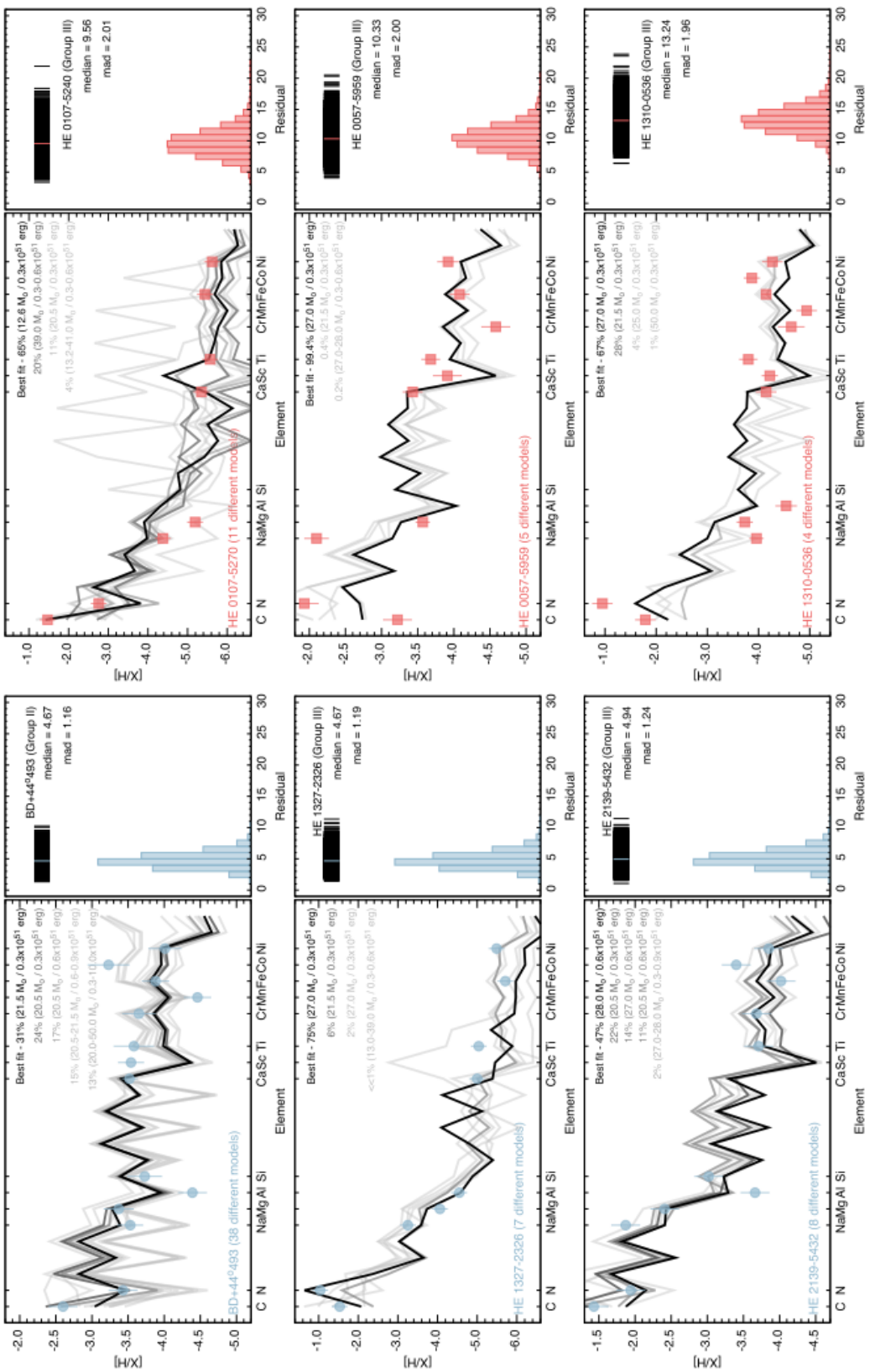

Figure 1.10: Abundances of CEMP-no group II and III with CCSNe predictions. Image from Placco et al. (2016). Residuals shown are from the χ^2 fitting used in the `starfit` code for 10,000 tested CCSNe models. Figure reproduced by permission of the AAS.

Chapter 2

Pop III i-process Nucleosynthesis and the Elemental Abundances of SMSS J0313-6708 the Most Iron-Poor Stars

Attributions: Falk Herwig and Marco Pignatari advised scientifically on the work presented in this chapter. All writing for the published letter was done by me with minor edits from the aforementioned. The writing of the erratum was conducted by myself with editorial contributions from Falk Herwig. The writing for the conference proceeding was conducted by myself. Co-authors on the proceeding were: Falk Herwig, Robert Andrassy, Paul Woodward, Marco Pignatari and Huaqing Mao.

The following work has been published in Monthly Notices of the Royal Astronomical Society. Minor edits for readability in the context of this thesis have been made.

2.1 Abstract

We have investigated a highly energetic H-ingestion event during shell He burning leading to H-burning luminosities of $\log(L_{\rm H}/{\rm L}_\odot) \sim 13$ in a $45{\rm M}_\odot$ Pop III massive stellar model. In order to track the nucleosynthesis which may occur in such an event, we run a series of single-zone nucleosynthesis models for typical conditions found in the stellar evolution model. Such nucleosynthesis conditions may lead to i-process neutron densities of up to $\sim 10^{13}{\rm cm}^{-3}$. The resulting simulation abundance pattern, where Mg comes from He burning and Ca from the i process, agrees with the general observed pattern of the most iron-poor star currently known, SMSS J031300.36-670839.3. However, Na is also efficiently produced in these i process conditions, and the prediction exceeds observations by $\sim$ 2.5dex. While this probably rules out this model for SMSS J031300.36-670839.3, the typical i-process signature of combined He burning and i process of higher than solar [Na/Mg], [Mg/Al] and low [Ca/Mg] reproduces abundance features of the two next most iron-poor stars HE 1017-5240 and HE 1327-2326 very well. The i process does not reach Fe which would have to come from a low level of additional enrichment. The i process in hyper-metal poor or Pop III massive stars may be able to explain certain abundance patterns observed in some of the most-metal poor CEMP-no stars.

2.2 Introduction

Pop III stars produced the first elements heavier than those created in the Big Bang and polluted the surrounding pristine gas (Nomoto et al., 2013). The most metal-poor stars we observe today may be the most direct descendants, or at least carry the most distinct signatures, of Pop III stars and therefore become a powerful diagnostic in our study of early cosmic chemical evolution (Frebel & Norris, 2015) .

Of the most iron-poor stars, the majority are classified as carbon enhanced metal poor -no (CEMP-no) (Beers & Christlieb, 2005). SMSS J031300.36-670839.3 (hereafter SMSS J0313-6708, Keller et al., 2014), is the most iron-poor star identified at present, with [Fe/H] ≤ -6.53, (Nordlander et al., 2017). Li, C, Mg and Ca have been measured and there are upper limits on several other elements. HE 1327-2326 (Frebel et al., 2006, 2008) and HE 1017-5240 (Christlieb et al., 2004) are the next two most iron poor stars known with [Fe/H] -5.96 and -5.3, respectively.

Low-energy or faint supernovae with strong fallback would have either very little

or no nucleosynthetic contribution from the supernova explosion (Keller et al., 2014; Takahashi et al., 2014; Marassi et al., 2014). However, many of the best fit models proposed for CEMP-no stars are within the mass range where Pop III and the lowest-metallicity stars are expected to collapse directly into black holes with no supernova explosion (Heger et al., 2003). Choplin et al. (2016) proposed that progenitors of such stars may have been massive, rapidly rotating, Pop III stars. Takahashi et al. (2014) found rotating Pop III models less favourable in reproducing the abundances of SMSS J0313-6708 than non-rotating models, but preferable for HE 1017-5240 and HE 1327-2326.

Overall, there is currently no clear consensus on either the production site or mechanism which would explain the observed abundances of SMSS J0313-6708, apart from the zero-metallicity nature of the progenitor. Here we are proposing a new nucleosynthesis mechanism that can operate in Pop III as well as hyper metal-poor massive stars.

H-ingestion events into the He-burning core or shell in Pop III and low-metallicity massive stars have been reported based on models with different stellar evolution codes and physics assumptions (Marigo et al., 2001; Heger & Woosley, 2010; Limongi & Chieffi, 2012; Takahashi et al., 2014; Ritter et al., 2017). The events affect the structure, evolution and nucleosynthetic yields of Pop III stellar models, but fundamental questions concerning the occurrence conditions and properties remain unanswered.

We investigate the possibility that nucleosynthesis patterns of CEMP-no stars SMSS J0313-6708, HE 1017-5240, and HE 1327-2326 contain the nucleosynthesis signatures of convective-reactive H-ingestion events. Such events would amount to a light-element version of the i process, a neutron capture process with neutron densities in the range 10^{13} – $10^{15}\,\mathrm{cm}^{-3}$, that is activated in convective-reactive, combined H and He-burning events (Cowan & Rose, 1977; Dardelet et al., 2014; Herwig et al., 2011; Hampel et al., 2016). We propose that this event may produce sufficient energy to expel a portion of the H/He convective-reactive layer of the star as discussed by Jones et al. (2016).

Section 2.3 describes the stellar evolution models, Section 2.4 the nucleosynthesis simulations and comparison with observations, and in Section 2.5 we conclude.

2.3 1D Stellar Evolution Model

We use the `mesa` stellar evolution code (Paxton et al., 2015, rev. 8118). Assumptions include the Ledoux criterion and semiconvection Langer et al. (1985) with efficiency parameter $\alpha = 0.5$. The custom nuclear network includes 82 species with A $= 1 - 58$. We neglect stellar mass loss because Pop III stars likely have inefficient line-driven winds (Krtička & Kubát, 2006). We ignore the effects of rotation.

The abundances or upper limits for Fe in the most iron-poor stars investigated here require the assumption of a low-energy supernova with strong fallback and little mixing. These stars are inconsistent with nuclear production of pair-instability supernovae making masses $\sim 140 - 260\,\mathrm{M}_\odot$ improbable (Keller et al., 2014). We have chosen an initial mass of $45\mathrm{M}_\odot$ which is expected to collapse into a black hole without SN explosion (Heger et al., 2003). We have explored other initial masses and they harbour similar thermodynamic conditions (Section 2.4). At this point we consider the stellar evolution simulations as guide for our nucleosynthesis calculations rather than a definitive solution.

We initialize with Big Bang abundances of Cyburt et al. (2016). The main-sequence and core-He burning phases follow previous descriptions closely (e.g. Marigo et al., 2001; Limongi & Chieffi, 2012). The time evolution of this model is shown in Fig. 2.1. Soon after the exhaustion of core He, a convective He-burning shell develops. After $\approx 2.5 \times 10^3\,\mathrm{yr}$ the He and H burning layer begin to interact and exchange material. H entering the He convection zone leads to energy generation at the interface of the layers. The entropy difference between the two layers before they come into contact is $\Delta S / N_\mathrm{A} k_\mathrm{B} \approx 7.5$, a factor of about $7-8$ less than in corresponding models of solar metallicity.

In the model, mixing occurs intermittently between the H shell and the He shell below, separated by a radiative layer with a radial extent of $2.7\lambda_P$, or pressure scale heights, from the base of the He shell. Just prior to the ingestion event the entropy difference has been reduced to $\Delta S / N_\mathrm{A} k_\mathrm{B} \approx 5$. From here H and a small amount of its associated burning products are mixed downward into the partially-burned He layer below. Nuclear energy production increases within minutes (Fig. 2.1), and the burning of H creates a split in the He-shell, similar to Herwig et al. (2011). 3D simulations are only starting to investigate this process with the necessary numerical effort (Herwig et al., 2014), but already show that violent, global instabilities are possible. The 3D behaviour is expected to be fundamentally different compared to

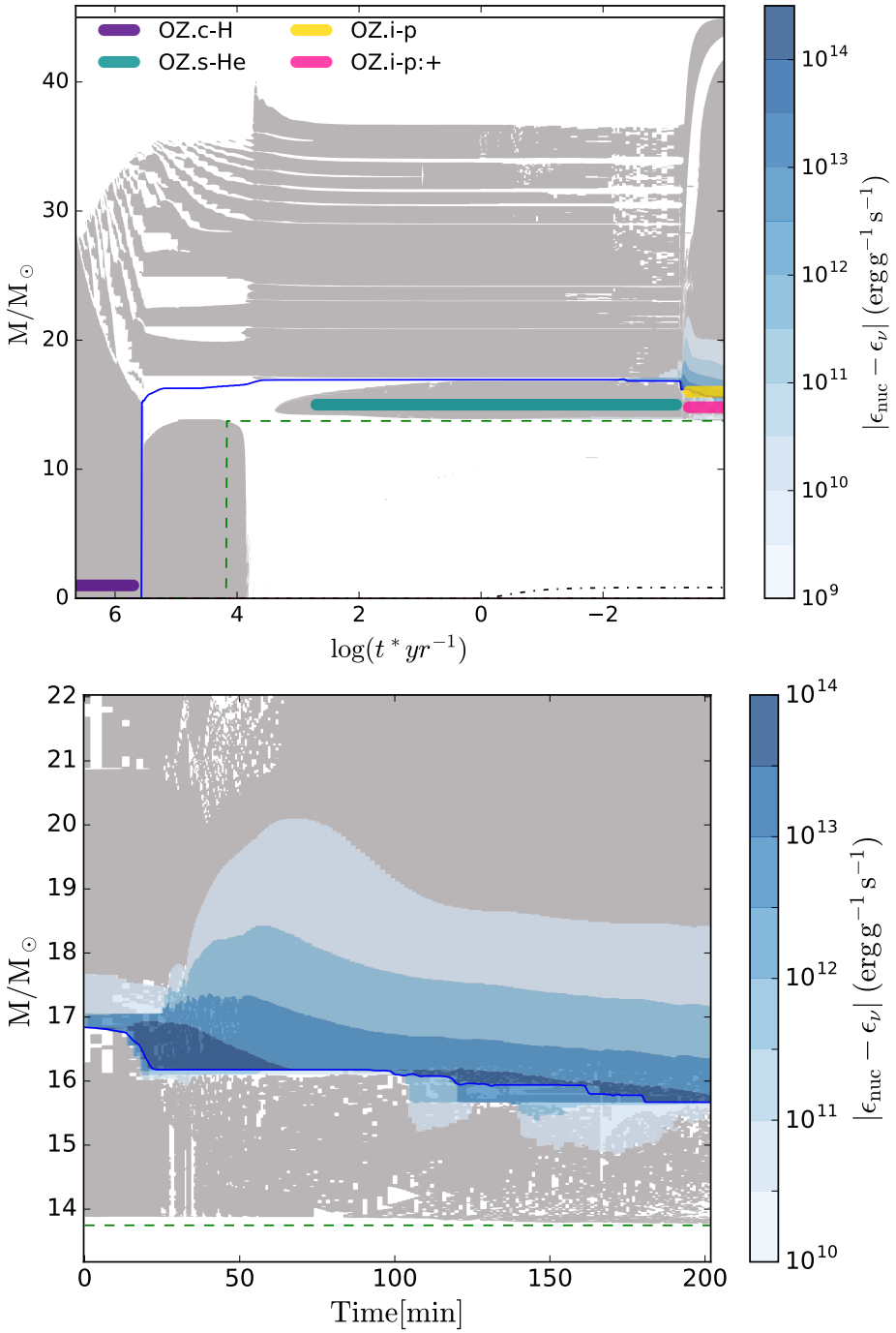

Figure 2.1: **Upper panel:** Evolution of convection zones (grey), nuclear energy generation (blue contours) and the H- (solid blue) and He- (green dashed) and C-free (black dashed) cores for the 45M$_\odot$ stellar evolution model. Purple, teal, yellow and pink lines schematically illustrate the regimes where single-zone calculations are preformed (Section 2.4). **Lower panel:** Zoom-in of H-ingestion event shown in linear time with $t = 0$ the beginning of the event.

what is seen in 1D stellar evolution models.

During this event, energy generation is dominated by $^{13}C(\alpha, n)^{16}O$. The luminosity in this region reaches $\log(L_H/L_\odot) \sim 13$. Following the approach of Jones et al. (2016) we calculate the maximum value $H = \epsilon_{nuc}\tau_{conv}/E_{int} \approx 0.26$, where ϵ_{nuc} is the specific energy generation rate of nuclear reactions, E_{int} is the specific internal energy, both measured within the upper portion of the split convection zone ($\sim 15.5-17.0 M_\odot$, Fig. 2.1). τ_{conv} is the convective timescale. Thus, a significant fraction of the binding energy of the layer is being deposited into this region of the star on a single mixing timescale, and, following the arguments of Jones et al. (2016), suggests a dynamic response that violate the assumptions of mixing length theory (MLT). MLT approximates convection through spatial and time averages over many convective turnover time scales and is applicable in non-dynamic, quiescent burning regimes. In the simulation presented here, it is expected that the large amount of energy generated from nuclear reactions will feedback into the flow in such a way that the MLT assumptions break down.

Towards the end of the lives of some massive stars, nonterminal, discrete mass loss events are detected as supernova type IIn or supernova imposters (see Section 4 of Smith, 2014). Arnett et al. (2014) suggest that these types of mass ejection events require 3D modelling, as MLT assumes a steady state whereas the late stages of massive stellar evolution are likely highly dynamic. 3D calculations with full 4π geometry performed by Herwig et al. (2014) demonstrate that under convective-reactive conditions, severe departures from spherical symmetry can occur. We hypothesise that something akin to a GOSH, or Global Oscillation of Shell H-ingestion, (Herwig et al., 2014) may occur in the model presented here. This must be verified by 3D hydrodynamic simulations. 1D calculations of similar H-ingestion events into the He burning shell in low-Z Super-AGB stars have been presented in Jones et al. (2016) where it is argued that H-ingestion events with similar H numbers could launch such outbursts. If so, even a relatively small amount of *i*-process enriched material could be ejected and enrich the surrounding ISM where then a second generation star forms, possibly with distinct abundance signatures. For now, the precise details of such a mechanism are beyond the scope of this letter.

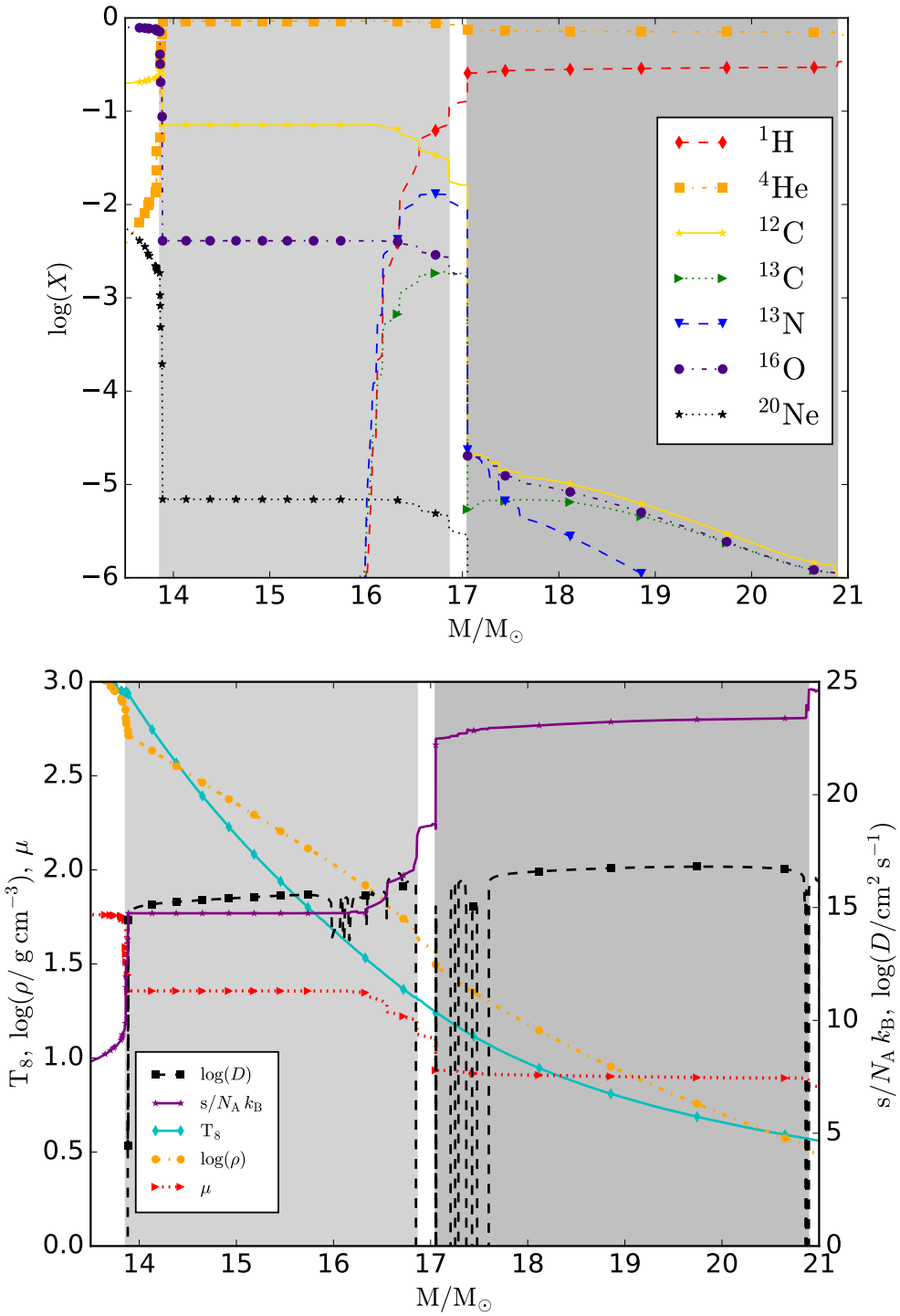

Figure 2.2: Grey areas show convective H and He-burning regions just before H begins mixing into to He shell. Abundances, temperature, density, mean molecular weight, entropy and diffusion coefficient for convective mixing shown 9 min later.

Table 2.1: Parameters for single-zone PPN calculations. Row 4 contains a single run with three output times.

Run ID	Burning phase	T (10^8K)	ρ (g cm^{-3})	Δt (yrs)
OZ.c-H	Core H	1.25	93.33	2.21×10^{4}
OZ.s-He	Shell He	2.6	330	1.28×10^{2}
OZ.s-He:+†	Shell He	2.95	487.1	4.45×10^{2}
OZ.i-p:t1,2,3	H-ingest.	2.0	191	$1,2,5\times10^{-2}$
OZ.i-p:+	H-ingest.	2.41	315.4	3.44×10^{-2}

†Single zone run representing more efficient and complete He burning. For details see section 2.4.

2.4 Nucleosynthesis Calculations

To study the nucleosynthesis in the H/He convective-reactive environment we employ separate nucleosynthesis calculations using the NuGrid single-zone PPN code (Pignatari et al., 2016). The single-zone method was chosen over multi-zone simulations, because the large H number of the convective-reactive event suggests that the 1D modelling assumptions of convection break down. Instead, one-zone simulations—although constituting a further simplification, allow studying the nucleosynthesis that may be possible in this event in isolation. The dynamic NuGrid network includes as required up to 5234 isotopes with associated rates from JINA Reaclib V1.1 (Cyburt et al., 2010) and other additional sources (see Pignatari et al., 2016). The general strategy is to approximate the nucleosynthesis through a series of three one-zone calculations which start with H burning followed by He burning and finally, we add in the last step a small amount of H to the partially completed He-burning nucleosynthesis calculation to estimate the nucleosynthesis due to H ingestion. The thermodynamic parameters for each of these three steps (Table 2.1) are taken to represent the conditions found in the stellar evolution simulation, as shown for the onset of the H-ingestion phase in Fig. 2.2.

Each of the one-zone simulation steps contributes to the final abundance distribution (Fig. 2.4). The H-burning simulation (OZ.c-H) starts with the same Big Bang abundances as the stellar evolution model. The OZ.c-H is evolved until it reaches the same CNO abundances as the stellar evolution model does at the end of H-core burning, which requires less time in the one-zone simulations because it does not include convective mixing. The output from this burning stage is used to initialize

the He-burning one-zone run. Two separate cases are considered (Table 2.1). OZ.s-He very closely follows the relatively small amount of He shell burning found in our stellar evolution model up to the point when the H and He shells start to interact.

The second scenario represents the case where He burning would have been able to advance further before the H/He mixing starts. The He-burning run OZ.s-He:+ adopts a higher temperature, but still within the range found in the He-burning shell (lower panel of Fig. 2.2) and runs for about 3.5 times longer than OZ.s-He. At this point the C, O and Mg are almost in the same proportions as in SMSS J0313-6708, similar to what is suggested by Maeder & Meynet (2015). The temperature and density were taken from the base of the He-burning shell just prior to the ingestion event. The OZ.s-He:+ case could be representative of a later H-ingestion event (into either the He burning core or shell) or a situation found in a model with different initial mass or different macroscopic mixing assumptions.

Each of the one-zone He-burning runs is followed by one or more one-zone models representing the H ingestion event. We add 1% H, by mass, to the output of the He-burning runs and renormalise all other isotopes. In these third one-zone models H burns rapidly in the $^{12}\mathrm{C}(p,\gamma)^{13}\mathrm{C}$ reaction, followed by β decay and neutron release in the $^{13}\mathrm{C}(\alpha,n)^{16}\mathrm{O}$ reaction, exactly the same as in the one-zone i-process calculations by Dardelet et al. (2014). The resulting nucleosynthesis is also similar in that high neutron densities typical for i process are reached and the nucleosynthesis path in the chart of isotopes includes n-rich unstable isotopes (Fig. 2.3). The one-zone models representing the H-ingestion episode are therefore labelled OZ.i-p (Table 2.1) with OZ.i-p:+ being the H-ingestion run following OZ.s-He:+.

We finally assume that the products of nucleosynthesis would be diluted by either or both the stellar envelope, which the material would have travelled through to reach the surface of the star, and subsequently, the ISM. The relative amount of dilution from the envelope and ISM individually is not yet clear. To directly compare the abundances of SMSS J0313-6708 we dilute the material such that the amount of i-process material is 0.15% for run OZ.i-p:t1 and 10^{-5} for run OZ.i-p:+ and the remainder has the Big Bang abundance distribution. These numbers are chosen to fit the Mg abundance for OZ.i-p:t1 and C for OZ.i-p:+.

Fig. 2.4 shows the results of the core-H (OZ.c-H), shell-He (OZ.s-He) and finally the i-process run at time t1 (OZ.i-p:t1, top panel) after dilution. The neutron densities rise to $\approx 6 \times 10^{13}$ cm^{-3} in both OZ.i-p:t1 and OZ.i-p:+ i-process runs. Run OZ.i-p:t1 has a C/Mg ratio much larger than observed because it reflects the beginning of

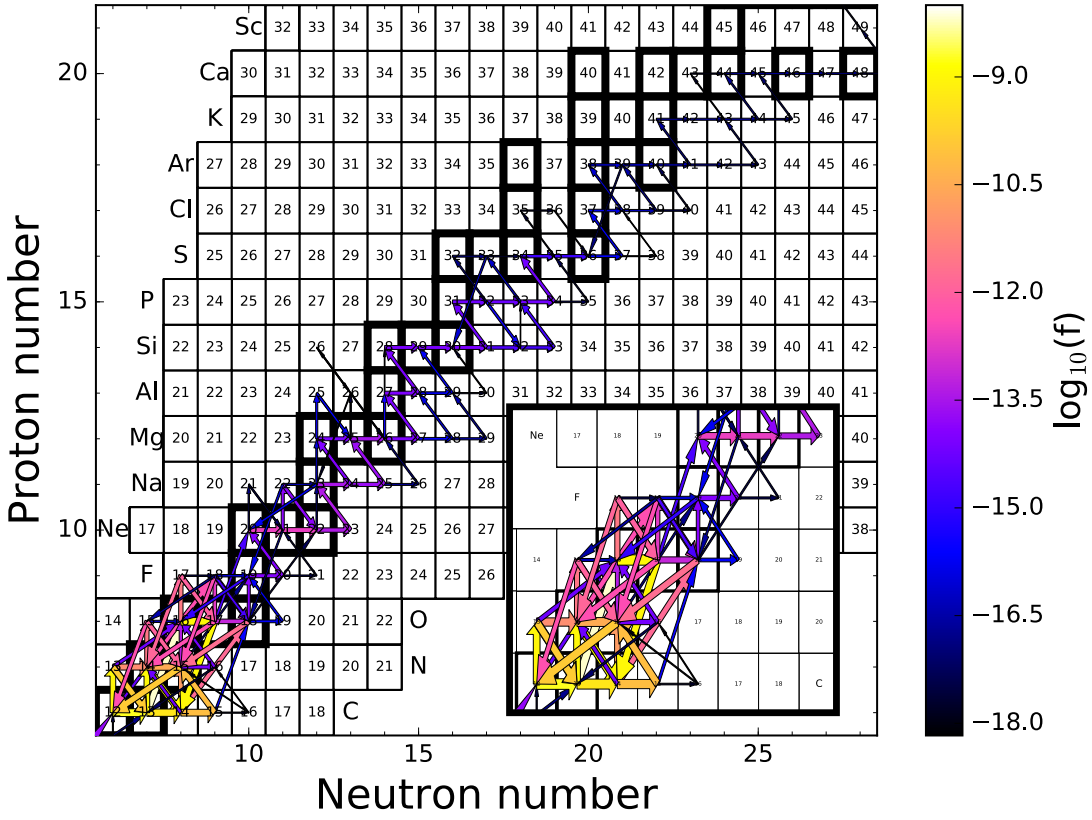

Figure 2.3: Nucleosynthesis fluxes showing the extent of the i process for the final model in run OZ.i-p:t1, $\log_{10}(\mathrm{f}) = \log_{10}(\mathrm{dY_i/dt})$.

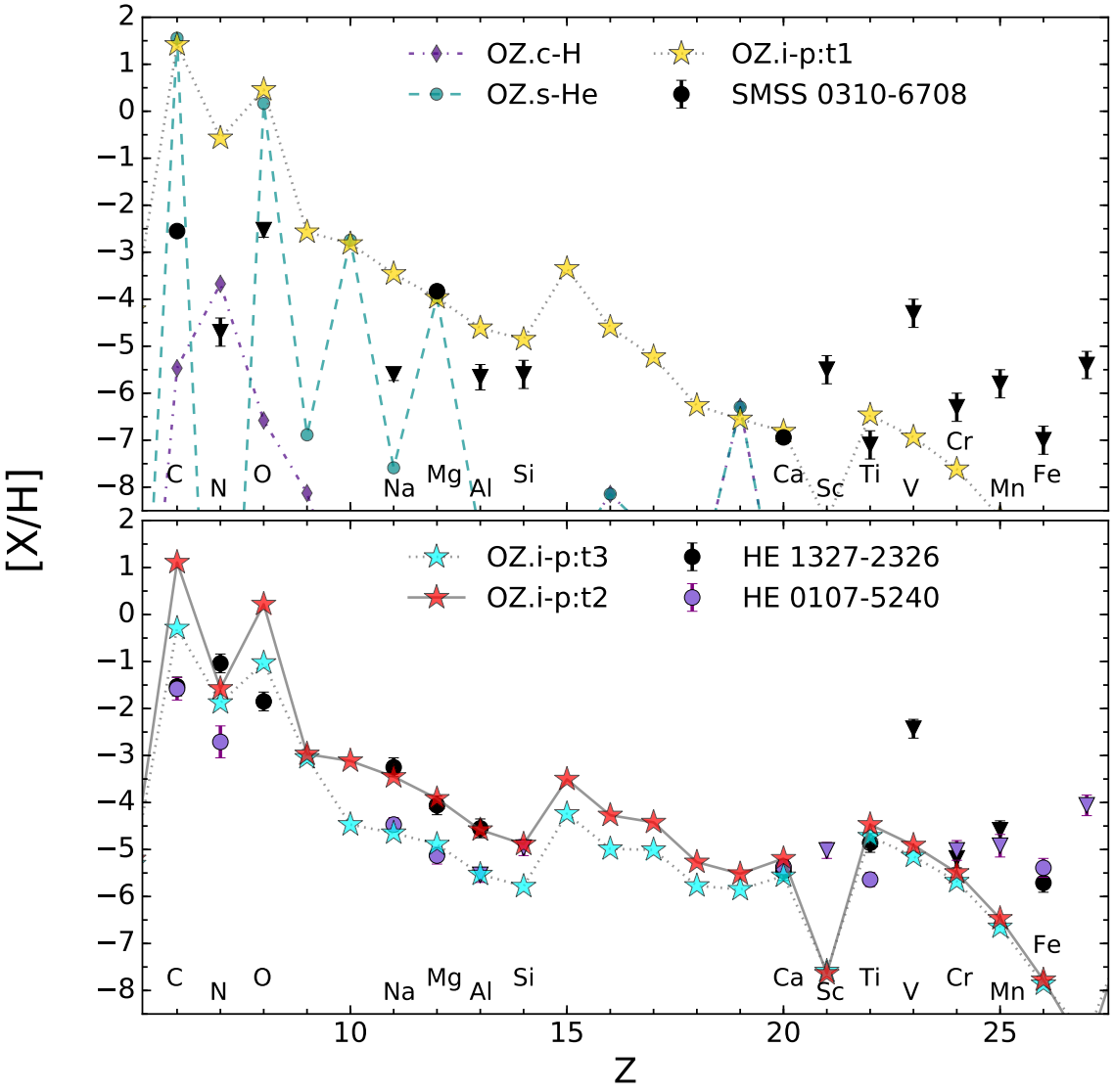

Figure 2.4: **Top Panel:** Abundances of SMSS J0313-6708 with upper limits shown as triangles Nordlander et al. (2017) compared to abundances from `PPN` runs OZ.c-H, OZ.s-He and OZ.i-p:t1 with dilution applied, see Section 2.4. **Bottom Panel:** Same for HE 1327-2326 and HE 1017-5240 after being diluted by factors 5×10^{-3} and 1×10^{-2} by mass, respectively.[1]

He burning. The exact time for H ingestion is poorly constrained, and using input abundances from more complete He burning can yield the observed C/Mg ratio, as is the case in run OZ.i-p:+. In the latter case much more Mg is produced in He burning which is reflected by much greater required dilution to compare with observations. In order to reproduce the observed Ca abundance from the n-capture reactions a higher neutron exposure of $\tau = 3\,\mathrm{mbarn}^{-1}$ was realized in this case.

According to Keller et al. (2014), Bessell et al. (2015), and Takahashi et al. (2014) observed abundances of Ca in SMSS J0313-6708 can be produced during H burning via breakout reactions. The production of Ca in our models by this reaction channel is at least 1dex lower than the observed Ca abundance in SMSS J0313-6708. Takahashi et al. (2014) report Ca production in H-shell burning at temperatures reaching $\log(T) = 8.66$ in models with masses initially in the range $80 - 140\mathrm{M}_{\odot}$. We do not find such high temperatures in any of our stellar evolution models, including tests with similar high and even higher initial mass. Pop III models of Limongi & Chieffi (2012) used by Marassi et al. (2014) are in better agreement with ours as they have similar H burning temperatures and do not produce appreciable Ca in quiescent burning phases.

In our simulations, Ca is primarily produced through n captures in i-process conditions in the form of ^{48}Ca. The production site of this isotope has been a long-standing question in the nucleosynthesis community (Meyer et al., 1996). Previous scenarios to make ^{48}Ca include anomalous CCSN conditions in parts of the ejecta (Hartmann et al., 1985), and the weak r-process (Wanajo et al., 2013).

It has been pointed out that H-ingestion events lead to Na production (Limongi & Chieffi, 2012). Na is overproduced in the i-process simulation compared to the observed abundance in SMSS J0313-6708 by > 2.5dex. A preliminary exploration of several nuclear physics uncertainties have not offered an obvious pathway to change this result and it seems unlikely that 3D effects would fundamentally do so either. Interestingly, the [Na/Mg] ratio of SMSS J0313-6708 is indicative of a strong odd-even effect often seen in yields of core collapse supernova (Prantzos, 2000), yet the upper limit of [Mg/Si] together with the low Al upper limit, and the high [Mg/Ca] at these low-metallicities can be accommodated by the i-process model. In our single-zone calculations Mg is produced in He burning. Na, Al, Si and Ca are produced during the H-ingestion i process phase. The α elements among these have two completely different nucleosynthetic origins.

We also compare our models with the next two most iron-poor stars known,

HE 1327-2326 and HE 1017-5240. Fig. 2.4, bottom panel, shows the model OZ.i-p:t2 and OZ.i-p:t3 which are from the same run as OZ.i-p:t1, except at later times when the neutron exposure has further increased. For the three successive runs $\tau \approx 2.5, 4$, and $8.75\,\mathrm{mbarn}^{-1}$. These simulations reproduce the observed sloping pattern of abundances and upper limits for Na, Mg, Al and Si very well. In this scenario, the composition of these CEMP-no stars could have been made by the contribution of a H-ingestion event, and at least one CCSN event contributing to the observed Fe-group elements. Interestingly, these models reproduce a similar decreasing abundance pattern from Ti, Cr to Mn that can be seen in some of the most iron-poor stars such as, CD-38°245, HE 1310-0536 or CS 22949-037 (Placco et al., 2016), which in our model is due to efficient absorption of neutrons around the magic number N = 28. This feature is often accompanied by the positive [Na/Mg] and [Mg/Al] ratios mentioned. Our preliminary tests show that both of these sloping abundance patterns for Na-Al and Ti-Mn can also be found if the initial metal abundance is hyper metal-poor instead of Pop III. The [Na/Mg] ratio could be as small as ≈ -0.3 dex in these conditions. But the presence Fe-group n-capture seeds, or even a too high neutron exposure with Pop III initial abundance, would lead to an efficient production of trans-iron elements with the *i*-process abundance signature, leading not to CEMP-no but to CEMP-i (or CEMP-r/s) star abundance signatures (Dardelet et al., 2014; Herwig et al., 2011; Hampel et al., 2016).

2.5 Conclusion

We compared Pop III *i*-process models with the three most iron-poor stars SMSS J0313-6708, HE 1327-2326 and HE 1017-5240. The Pop III *i*-process models are based on massive Pop III stellar evolution models which undergo a highly energetic H-ingestion event during He shell burning. MLT description of convection breaks down in this situation, and 1D models are therefore unreliable. 3D simulations are required. In the meantime we therefore use a series of single-zone nucleosynthesis calculations in an initial attempt to identify the nucleosynthetic signature of Pop III *i* process in isolation. The general abundance distribution of SMSS J0313-6708 is reproduced by our models, but Na is overproduced by > 2.5 dex, which likely rules this scenario out for SMSS J0313-6708. When comparing our models to HE 1327-2326 and HE 1017-5240, the high [Na/Mg] and [Mg/Al] ratios, which are difficult to reconcile with metal poor CCSN models, are well reproduced, and Pop III *i* process

becomes a promising candidate for at least a portion of the nucleosynthetic material of which these stars are made. Our models are able to recover the low observed [Ca/Mg].

Many details in this scenario remain uncertain and will be subject to further investigation. The greatest areas of uncertainty are the convective nature of the event in 3D, the single zone-treatment of the nucleosynthesis and the uncertain nuclear physics data of n-rich, unstable light elements.

2.6 Erratum

An erratum was published for the preceding work. This erratum was submitted due to an error in the final data presented which was the result of a bug in the data-handling tools I used. The bug in the code produced and used by the NuGrid group led to the final abundances plotted but being properly decayed. The correction led to slight changes in the abundance distribution, but did not affect our results or conclusions.

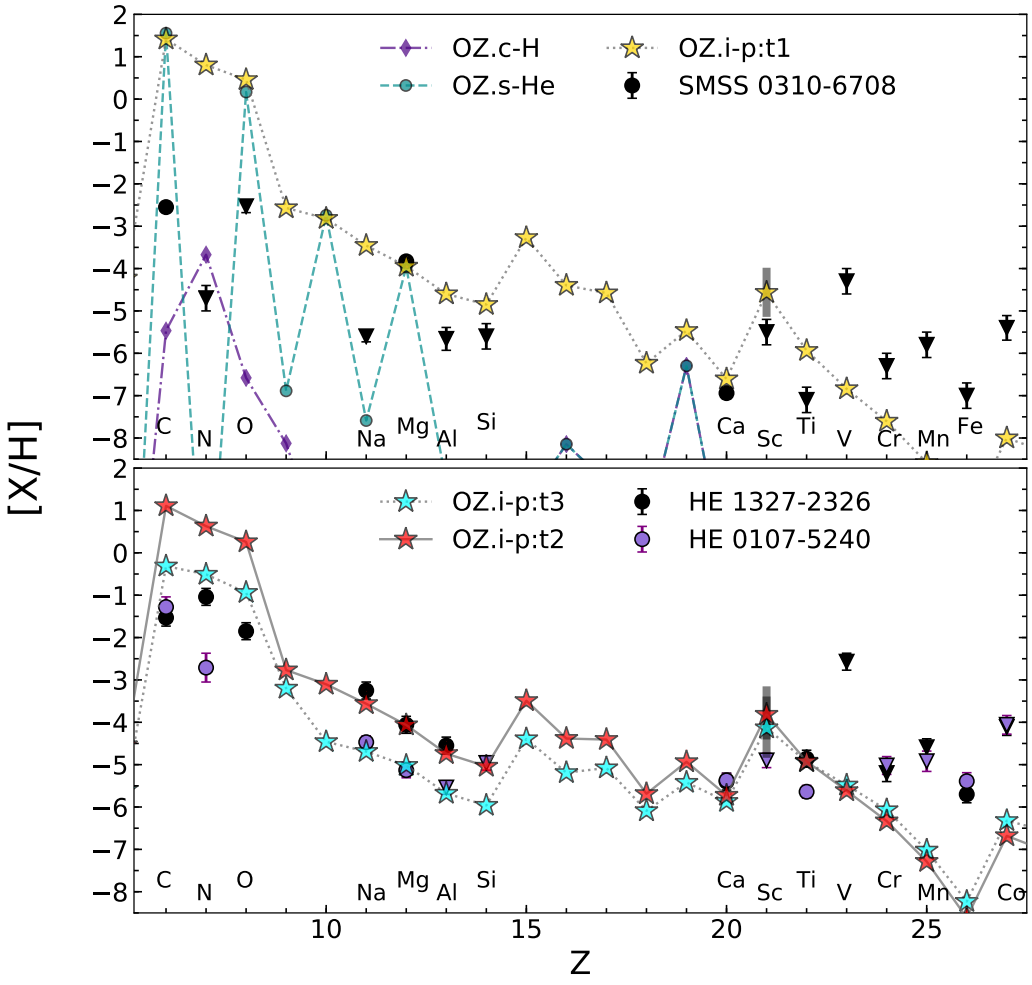

Figure 2.5: PPN simulations from Clarkson et al. (2019b)

2.7 Conference Proceeding

After attendance in the 2018 Nuclei in the Cosmos conference in L'Aquila, Italy, I wrote a conference proceeding on the updates in my project. I had two important findings that went above and beyond the findings presented in Clarkson et al. (2018). I ran two simulations based on an $80M_{\odot}$ Pop III stellar model with the same mixing assumptions used in Clarkson et al. (2018). These models include higher He-burning temperatures and densities than the $45M_{\odot}$ simulation presented in Clarkson et al. (2018). This better reproduces the [C/Mg] ratios found in these CEMP-no stars. I found that the i process in Pop III conditions would extend beyond the Fe-group elements and that this could be used to constrain the total neutron exposure, such that these heavy elements were not overproduced. This is shown in Fig. 2.6 Specifically, I found that the neutron exposure had to be lower than in simulations of Clarkson et al. (2018) by a factor of ~ 4 in order to satisfy the upper limits on heavy elements in these stars. I also included preliminary data on the results in 3 and a hydrodynamics simulation similar to those presented in 4.

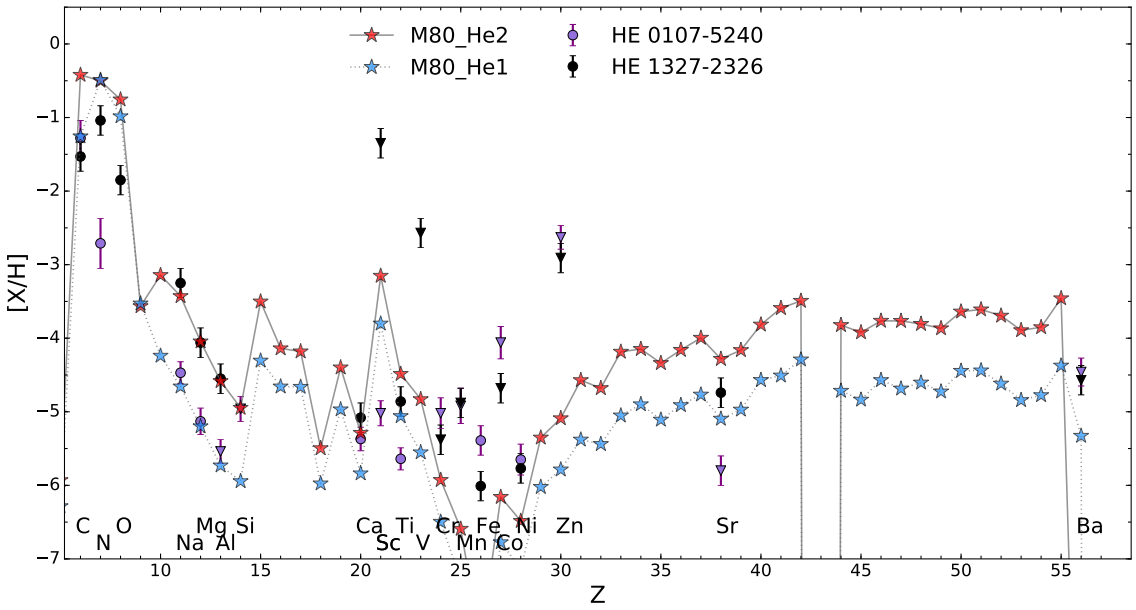

Figure 2.6: PPN simulation with CEMP-no abundances from Clarkson et al. (2019a)

Chapter 3

Convective H-He Interactions in Massive Population III Stellar Evolution Models

Attributions: Falk Herwig advised scientifically on the work presented in this chapter. All writing for the published letter was done by me with edits and minor contributions from the aforementioned.

This work is published in the Monthly Notices of the Royal Astronomical Society journal. Minor edits for readability in the context of this thesis have been made.

3.1 Abstract

In Pop III stellar models convection-induced mixing between H- and He-rich burning layers can induce a burst of nuclear energy and thereby substantially alter the subsequent evolution and nucleosynthesis in the first massive stars. We investigate H-He shell and core interactions in 26 stellar evolution simulations with masses $15-140\,M_\odot$, using five sets of mixing assumptions. In 22 cases H-He interactions induce local nuclear energy release in the range $\sim 10^9 - 10^{13.5}\,L_\odot$. The luminosities on the upper end of this range amount to a substantial fraction of the layer's internal energy over a convective advection timescale, indicating a dynamic stellar response that would violate 1D stellar evolution modelling assumptions. We distinguish four types of H-He interactions depending on the evolutionary phase and convective stability of the He-rich material. H-burning conditions during H-He interactions give $^{12}C/^{13}C$ ratios between ≈ 1.5 to ~ 1000 and [C/N] ratios from ≈ -2.3 to ≈ 3 with a correlation that agrees well with observations of CEMP-no stars. We also explore Ca production from hot CNO breakout and find the simulations presented here likely cannot explain the observed Ca abundance in the most Ca-poor CEMP-no star. We describe the evolution leading to H-He interactions, which occur during or shortly after core-contraction phases. Three simulations without a H-He interaction are computed to Fe-core infall and a $140\,M_\odot$ simulation becomes pair-unstable. We also discuss present modelling limitations and the need for 3D hydrodynamic models to fully understand these stellar evolutionary phases.

3.2 Introduction

Metal-poor and CEMP (Carbon-Enhanced Metal-Poor) (Beers & Christlieb, 2005) stars provide a wealth of information regarding the nature of early galactic chemical enrichment. It is often supposed that the most Fe-poor of these stars have been enriched by a single Population III (Pop III) star (Frebel & Norris, 2015). In order to replicate the abundances of some of the most Fe-poor stars it has been found that some degree of mixing between H- and He-burning layers during the stars lifetime is likely needed (e.g., Limongi et al., 2003; Maeder & Meynet, 2015), as this mixing activates nucleosynthetic pathways otherwise closed. While such nucleosynthesis appears necessary to reproduce the abundance patterns in many Fe-poor stars, as of yet, there has been no systematic investigation into the impact of such events on a

set of 1D Pop III stellar models.

1D stellar evolution simulations suggest that massive Pop III stars may have undergone mixing events between H- and He-burning layers. This was first described by Woosley & Weaver (1982) for a very massive Pop III stellar model. Marigo et al. (2001) found H-He interactions[1] between H shells and He cores but dismissed their results as *physically unsound* due to the lack of coupling of mixing and burning in their code at the time.

Heger & Woosley (2010) describe such events occurring in a $25\,M_\odot$ model after core C depletion in a set of Pop III massive stellar models used to produce supernova yields. They observed the convective He-burning shell and radiative envelope to mix. This was reported to produce large amounts of N due to the boost in CNO at the base of the H envelope as He-burning ashes were made available. In an $80\,M_\odot$ model during core He burning, they found the He core encroached upon the H shell, ultimately mixing H downward to create N which then convected downward, producing ^{22}Ne. They considered these events and the nucleosynthetic by-products as uncertain yet unavoidable.

In another set of supernova yields, Limongi & Chieffi (2012) note that their stellar models of massive, Pop III stars encounter interactions between H and He shells. They report such mixing for stellar models of 25, 30 and $35\,M_\odot$ again, typically increasing the abundance of primary N in the H shell in addition to the high [Na/Mg] reported in a previous work endeavouring to explain the most Fe-poor star at the time, HE 0107-5240 (Limongi et al., 2003).

Ritter et al. (2018) encountered H-He interactions in simulations of $1\,M_\odot - 25\,M_\odot$ from $Z = 0.006$ and $Z = 0.0001$ and report neutron densities from such events of $\log N_n \sim 11 - 12$ resulting from the activation of the $^{13}\mathrm{C}(\alpha, n)^{16}\mathrm{O}$ neutron source.

It has been suggested that nucleosynthesis patterns in some CEMP-no stars — CEMP with no overabundance of s- or r-process elements, may be the result of a late mixing process between H and He-layers, potentially resulting in the variety of $^{12}\mathrm{C}/^{13}\mathrm{C}$ ratios observed in CEMP-no stars (Choplin et al., 2016). In a study on the effect of rotation on 1D Pop III models, Ekström et al. (2008) reported H- and He-mixing during core He burning for both rotating and non-rotating models though attributed it to rotational mixing where there was a higher frequency of the mixing

[1]Throughout this work we refer to all events where H- and He-rich material mix as H-He interactions rather than proton/H-ingestion or any other name regardless of the stellar site, unless comprehensibility demands it.

event.

In the pursuit of understanding the chemical abundances of some CEMP stars, the i process has been suggested as a possible explanation. The i process is a neutron-capture process with neutron densities, $N_{\rm n}$, intermediate between those of the s and r processes. This process was originally discussed by Cowan & Rose (1977) for low-mass stars undergoing He shell flashes and has been invoked to explain several abundance patterns more recently including the post-AGB star V4334 Sagittarii and CEMP-r/s stars (e.g. Herwig et al., 2011; Dardelet et al., 2014; Denissenkov et al., 2019; Hampel et al., 2016, 2019). The i process occurs in convective-reactive regimes—when mixing and nucleosynthesis timescales are comparable. For this reason, the Damhöhler number, or Da has been used to describe i-process conditions as it is the dimensionless ratio of the nuclear reaction timescale relative to the mixing timescale (Herwig et al., 2011). i-process conditions are characterized by Da ≈ 1.

Jones et al. (2016) studied models of super-AGB stars of Z $= 10^{-5} - 0.02$. In these simulations the convective H-envelope is found to burn corrosively into core He-burning ashes after the second drege-up, similar to what has been seen in $9{\rm M}_{\odot}$ and $7{\rm M}_{\odot}$ models of García-Berro et al. (1997) and Herwig et al. (2012), respectively. After this corrosive burning phase a dredge-out event occurs (see also Ritossa et al., 1999; Gil-Pons et al., 2013; Doherty et al., 2014). This happens where He burning is sufficiently strong to induce convection in the He shell during the second dredge-up, and the descending H envelope and expanding He shell merge. Jones et al. (2016) found these shell merger events, where protons descend into the He shell reacting with C via the $^{12}{\rm C}(p,\gamma)^{13}{\rm N}$ reaction, lead to luminosities in excess of $10^9\,{\rm L}_{\odot}$ and posit that such an event would lead to the i process followed by mass-ejection events.

Clarkson et al. (2018, 2019b) investigated a H-He interaction in a $45\,{\rm M}_{\odot}$ Pop III stellar model, leading to i process conditions and compared nucleosynthesis results with the elemental abundances of the three most Fe-poor stars at the time, SMSS J031300.36-670839.3 (Keller et al., 2014), HE1327-2326 (Frebel et al., 2006), and HE0107-5240 (Christlieb et al., 2004). With luminosities of $10^{13}\,{\rm L}_{\odot}$, mixing length theory (MLT) (Böhm-Vitense, 1958) is unable to accurately predict the resulting nucleosynthesis and therefore, exploratory single-zone nucleosythesis calculations using temperatures and densities found in the He shell were performed. We found that the light-element signature—trends of high [Na/Mg], [Mg/Al] and [Al/Si]—are naturally reproduced by the i process. Here the odd-Z elements are made by n-captures as well as Ca. Similar trends were also recovered in Ti-Mn which has been seen in several

other CEMP-no stars.

Nucleosynthesis in an $80\,M_{\odot}$ model was investigated using the same methods and predict these events can produce elements heavier than Fe without violating observed upper limits in CEMP-no stars (Clarkson et al., 2019a). Similar to Jones et al. (2016), Clarkson et al. (2018) suggested that mass-ejection events might result from H-He interactions, not unlike the precursor events that lead to the circumstellar material observed in Type IIn SNe or other pre-supernova outburst events (see Smith et al., 2011). This scenario does not include a faint supernova, as Pop III stars with masses $\sim 40 - 100\,M_{\odot}$ are expected to collapse into a black hole directly with no supernova explosion (Heger et al., 2003). More recent studies including the neutrino-driven explosion mechanism paint a more complicated picture regarding the fate of massive stars of zero intial metallicity (e.g. Ebinger et al., 2020). Sukhbold & Adams (2020) suggest that the upper mass limit for a successful core collapse supernova explosion may be closer to $\sim 20\,M_{\odot}$, which seems to scale only weakly with metallicity (Sukhbold & Woosley, 2014), with lower metallicity stars producing more black holes, generally. The ultimate fate of these stars is currently an unsolved problem, requiring 3D hydrodynamic simulations including a number of physical ingredients (Couch, 2017; Müller et al., 2017).

Banerjee et al. (2018) also looked at mixing of H with He shells of massive Pop III and low-Z stellar models. During post-processing, to reproduce heavy-element abundances of CEMP-no stars, they induce H-He interactions by injecting protons to the top of the He shell. In doing so, they are able to reproduce the overall heavy element abundances in CEMP-no stars.

In low and intermediate-mass stellar models, interactions between H and He layers have been studied by a multitude of authors and are well documented in the literature. These events have been found to occur in several stellar sites for different metallicities, masses and evolutionary phases. The He-shell flash (e.g. Fujimoto et al., 1990; Cristallo et al., 2009; Suda & Fujimoto, 2010), hot dredge-up (Herwig, 2004; Goriely & Siess, 2004), and thermal pulses and interpulse periods (Hollowell & Iben, 1989; Lugaro et al., 2012) in Pop III and low-Z AGB stars, the He core flash (Campbell et al., 2010; Schlattl et al., 2001), and rapidly-accreting white dwarfs (Denissenkov et al., 2019) are all sites where H-He interactions have been found to occur.

Studies involving the impact of mixing assumptions in H-He interactions have been done for the case of low and intermediate mass stars. For these stars, early studies focused on the effects of mixing rate of protons into a He-rich environment and

splitting of the He-rich convection zone (Malaney, 1986, and references therein). More recently, the focus has moved to the influence of convective boundary mixing (CBM). Miller Bertolami et al. (2006) explored the influence of convective mixing theories and CBM in post-AGB models, finding that born-again episodes were altered by both considerations. Studies have also found that both CBM and mass can effect the depth of dredge up episodes (Herwig, 2004; Lau et al., 2009). Jones et al. (2016) studied CBM efficiency for the envelope and pulse driven convection zone in SAGB stars. They found that for all values of CBM efficiency H-He interactions were encountered frequently, with higher values generally leading to higher H-burning luminosities.

Convective shell interactions (CSI) between other burning shells during advanced burning stages in massive stars can lead to unique nucleosynthesis and asymmetries in 3D hydrodynamic simulations possibly aiding supernova explosions (Yadav et al., 2019; Andrassy et al., 2020).

In this work, we explore the impact of a range of commonly adopted convective boundary mixing assumptions on Pop III massive star evolution models. Thereby this work complements the recently emerged effort of the community to better understand the impact of macro- and microphysics uncertainties on model predictions. For example, Kaiser et al. (2020) investigated the impact of convective boundary mixing parameters on main-sequence (MS) and He-burning evolution for three different stellar mass massive star models at solar metallicity. Fields et al. (2018) have investigated the impact of nuclear reaction rate uncertainties for a $15\,M_{\odot}$ stellar evolution model. Sukhbold & Woosley (2014) included separate sensitivity studies on the impact of resolution and mixing, in the form of semiconvection and CBM, on the compactness parameter (O'Connor & Ott, 2011) in massive pre-supernova stellar models. In a similar vein, Davis et al. (2019) examined how a varying CBM parameter affects the late-time evolution of a $25\,M_{\odot}$ stellar model. Farmer et al. (2016) conducted a study on the effects of both network size and resolution in the evolution of solar metallicity massive stars. This group of studies illustrates a growing trend in the stellar evolution community to begin to quantify the uncertainties within 1D models.

Our aim in this work is to characterize the different types of CSI that may occur in massive Pop III stars and under which mixing assumptions they occur. This macrophysics impact study can serve as a guide for future targeted investigations of hydrodynamic instabilities through 3D simulations. In this way, future research may shed light on how massive stars evolve after a violent H-He interaction. For models which do not experience interactions we, follow the evolution to core collapse

or onset of the pair instability. Our macrophysics impact study also reveals insights into the general conditions of H burning in Pop III stars and we can outline observable implications, for example for the C and N elemental and isotopic ratios. Section 3.3 describes the methods used, in Sections 3.4 and 3.5 we present and discuss core and shell H burning and H-He interactions, respectively. In Section 3.6 we compare our models to previous findings and discuss our results. Conclusions are given in Section 3.7.

3.3 Methods and Models

We calculate a grid of 26 stellar models using `MESA` rev. 8118 (Paxton et al., 2015). Beginning with Big Bang abundances taken from Cyburt et al. (2016), we explore five initial masses and mixing assumptions with the addition of one model with no convective boundary mixing, for 26 models in total. We study 15, 40, 60 ,80 and 140 $M_\odot$ stellar models (Table 3.1). This choice of mass range reflects our current knowledge of the Pop III initial mass function (IMF) as derived from simulations (Susa et al., 2014; Stacy et al., 2012) and spans a large enough range to explore the effects of mass on both chemical evolution and H-He interactions.

In all `MESA` simulations, a custom network of 151 species up to Ni was included and is shown in Table 3.2. The JINA Reaclib database (Cyburt et al., 2010) is utilized, including both strong and weak reactions for the chosen isotopes, amounting to over 1,500 reactions. We chose this network in order to realize possible proton captures from hot CNO breakout reactions as reported by Keller et al. (2014) and Takahashi et al. (2014). This network follows neutron captures no more than one isotope off the valley of stability, and only goes to the iron group therefore, if the i process occurs, we do not follow neutron capture processes realistically. Note we do not include a full Si-burning network, although this will not affect the results presented in this work.

There is a great amount of uncertainty in how much, if any, mass loss would have occurred in Pop III stars (Krtička & Kubát, 2006). Here we do not include mass loss, although we do allow small amounts of mass from the stellar surface to be removed if the density drops below $10^{-12}\,\mathrm{g\,cm^{-3}}$. This is done to keep all computational cells within the given equation of state tables in this version of the `MESA` code. For the most part, stellar surfaces do not drop to such low densities.

For spatial resolution controls, we use `MESA`'s `mesh_delta_coeff`, δ_{mesh}, of 0.5 during the pre-main sequence, and reduce this value to 0.2 onwards. This parameter

globally refines the grid such that cell-to-cell changes in quantities such as P, T and $\epsilon_{\rm nuc}$ are within a desired threshold, i.e., resolution is increased for regions with steep gradients in these quantities. We also apply a minimum number of total cells using `max_dq`$= 10^{-3}$, which is the maximum fraction of the total mass within each cell. This leads to an average of approximately 5,000-7,000 cells after the pre-main sequence for our models with approximately $50-90$ cells per dex drop in H abundance at the base of the H shell. For timestepping, we similarly use a `var_control_target`, v_c, of 10^{-4} on the pre-main sequence and reduce this to 10^{-5} afterwards. This limits timesteps based on changes in variables such as, ρ, T and R and checks that there have not been large changes in other quantities like L, X_i and $\epsilon_{\rm nuc}$. For changes in composition, we further limit the timesteps using the `dX_nuc_drop_limit` controls for species with $A \leq 20$ and $X_i \geq 10^{-4}$. We choose a limiting value for `dX_nuc_drop_limit` of 3×10^{-3}, which is the largest drop in mass fraction allowed due to either nuclear burning or mixing.

In H-He interactions, the convective turnover time scale and the nuclear time scale of H-rich material reacting with ^{12}C from the He-burning shell are often similar. This regime poses a particular challenge to the stellar evolution code. Nuclear reactions with dynamically relevant energy release are operating on the same time scale as new fuel for these reactions is brought into the burning region by convection. The computationally most efficient way to solve the structure, mixing and nuclear network equations of stellar evolution is to solve each of these operators separately for each time step. This is a good approximation if the nuclear, mixing and dynamic time scales are all respectively very different. In H-He interactions or CSI simulations this operator-split approach would give inaccurate results unless the mixing time scale is well resolved. This is usually prohibitively costly and not practical. Several variations of solving two of the three operators jointly have been deployed. For example Herwig et al. (1997) adopted a joint-operator solution to the nuclear network and diffusive mixing. While this approach leads to a reasonable approximation of the abundance profiles, especially the profile of H, it leaves out the immediate impact of the energy release on the structure equations. The `MESA` stellar evolution code solves all the mixing, nucleosynthesis and structure equations jointly. This approach provides the most accurate 1D structure models for situations of nuclear energy feedback on convective time scales, such as in H-He interactions, as long as the fundamental 1D assumptions of spherical and time averaging are not violated.

As discussed in Section 3.2 for low and intermediate mass stars, it has been shown

that H-He interactions can be affected by mixing assumptions. There are many different prescriptions available for a variety of extra mixing processes beyond what is included in standard MLT, and therefore, a full survey would be impractical. To limit the scope of our study we chose a sample of more commonly used prescriptions for non-rotating stars.

We include either the Schwarzschild criterion or the Ledoux criterion for convection with some amount of additional mixing between convective layers. We employ this additional mixing in the form of convective boundary mixing (CBM) and/or semiconvection. CBM is intended to account for instabilities which occur at the boundaries of convection zones. This can include turbulent entrainment as seen in 3D hydrodynamical simulations (Woodward et al., 2015; Meakin & Arnett, 2007), or internal gravity waves (Denissenkov & Tout, 2003; Battino et al., 2016). In this work we use the exponential 'overshoot' prescription given in Herwig (2000) and refer to this as CBM throughout the work. For the CBM parameter, we use either a 'high' value of $f_{\rm ov} = 0.01$ or a 'low' value of 0.001. This can be compared to similar parameter studies, such as Davis et al. (2019) where $f_{\rm ov}$ ranges from 0.002 to 0.032. Kaiser et al. (2020) includes a detailed discussion of this free parameter and adopts values of $f_{\rm ov} = 0 - 0.05$. Additionally, Higgins & Vink (2019) found that a high value of CBM ($\alpha_{\rm ov} = 0.05$) in the form of step-overshoot was necessary to explain the extent of the main-sequence and high-end luminosity limits for red giant stars.

Semiconvection is a secular mixing process that occurs when a region within a stellar model is stable according to the Ledoux criterion and unstable according to the Schwarzschild criterion for convection. This overstable region will give rise to partial mixing as the convective velocities will be limited by the stabilizing μ gradient (Schwarzschild & Härm, 1958; Stothers, 1970). For all models using the Ledoux criterion, we include semiconvection using the prescription of Langer et al. (1985) with an efficiency $\alpha_{\rm semi} = 0.5$. This value of $\alpha_{\rm semi}$ is within the prescribed range given in Langer et al. (1985) and is chosen to avoid the splitting of the He burning core which occurs if the mixing speed is much lower (see e.g. Sukhbold & Woosley, 2014).

Table 3.1: Stellar models: Run ID, maximum central temperature during the main-sequence, maximum H shell burning temperature, main-sequence lifetime, interaction, interaction type, maximum $H-$number, and total change in mass coordinate of H-rich material.

Run ID[a]	$T_{\rm H,core,max}$ (10^8K)	$T_{\rm H,shell,max}$ (10^8K)	$\tau_{\rm MS\,(Myrs)}$	H-He interaction	H-He interaction type[b]	$H_{\rm max}$[c]	Δ M/M$_\odot$
`15Mled`	1.05	1.09	10.0	×	–	9.48×10^{-5}	0
`15Mledf-h`	1.05	1.06	10.19	✓	`Rad-Shell`	0.05	0.78
`15Mledf-l`	1.05	1.03	10.06	✓	`Rad-Shell`	0.88	0.94
`15Mschf-h`	1.05	1.18	10.22	✓	`Rad-Shell`	5.3×10^{-3}	0.85
`15Mschf-l`	1.05	1.21	11.1	✓	`Rad-Shell`	0.11	0.91
`40Mled`	1.27	1.58	4.46	✓	`Conv-Shell`	0.22	1.28
`40Mledf-h`	1.27	1.06	4.53	✓	`Rad-Core`	8.59×10^{-5}	2.48
`40Mledf-l`	1.27	1.29	4.50	✓	`Rad-Shell`	1.97×10^{-6}	0.26
`40Mschf-h`	1.27	1.23	4.63	✓	`Rad-Shell`	0.35	2.80
`40Mschf-l`	1.27	–	5.32	✓	`Rad-Core`	0.62	2.24
`60Mled`	1.33	1.89	3.52	✓	`Conv-Shell`	0.28	0.40
`60Mledf-h`	1.33	1.44	3.56	✓	`Rad-Shell`	0.74	1.77
`60Mledf-l`	1.33	1.28	3.53	×	–	5.9×10^{-4}	0
`60Mschf-h`	1.33	–	3.69	✓	`Conv-Core`	1.3×10^{-3}	23.24[d]
`60Mschf-l`	1.33	–	3.65	✓	`Conv-Core`	1.3×10^{-3}	22.91[d]
`80Mled`	1.36	2.34	3.07	×	–	4.05×10^{-4}	0
`80Mledf-h`	1.36	2.23	3.10	✓	`Rad-Shell`	0.74	3.12
`80Mledf-l`	1.36	1.28	3.07	✓	`Rad-Shell`	1.82×10^{-6}	0.39
`80Mschf-h`	1.36	–	3.37	✓	`Conv-Core`	0.07	35.6
`80Mschf-l`	1.36	1.44	3.46	✓	`Rad-Shell`	2.42e-05	0.16
`140MNoMix`	1.42	–	2.71	✓	`Conv-Core`	0.01	59
`140Mled`	1.42	2.18	2.48	×	–	7.27×10^{-4}	0
`140Mledf-h`	1.42	–	2.50	✓	`Rad-Core`	0.32	6.05
`140Mledf-l`	1.42	1.36	2.49	✓	`Rad-Shell`	1.64×10^{-7}	1.45
`140Mschf-h`	1.42	–	2.76	✓	`Conv-Core`	0.01	73.61[d]
`140Mschf-l`	1.42	–	2.74	✓	`Conv-Core`	3.05×10^{-5}	71.21

[a]Run IDs represent the mass, criterion for convection, and boundary mixing parameters used, e.g. `15Mledf-h` is a 15M$_\odot$ model with the Ledoux criterion for convective stability with semiconvection and our larger value of CBM. See section 3.3 for details on the models.

[b]Naming used refers to either a convective (C) or radiative (R) He-rich shell or core region that the convective H shell is interacting with.

[c]H as defined in Eq. (3.2).

[d]See Section 3.5.4 for a description of `60Msch-` and `140Mschf-h` interactions.

Table 3.2: Nucleosynthesis network used in `MESA` simulations.

Element	Z	Element	Z
H	1-2	P	27-32
He	3-4	S	29-37
Li	6-7	Cl	31-40
Be	7-9	Ar	33-42
B	10	K	36-43
C	11-13	Ca	37-48
N	12-15	Sc	40-45
O	14-18	Ti	41-53
F	16-19	V	47-52
Ne	18-22	Cr	49-54
Na	20-23	Mn	53-55
Mg	21-26	Fe	54-58
Al	23-27	Ni	56
Si	25-31		

3.4 Hydrogen Burning

3.4.1 Core H Burning

Given their initial primordial composition, massive Pop III stars begin H-burning via p-p chain reactions. These reactions are energetically insufficient to maintain complete equilibrium at temperatures over $\approx 1.5 \times 10^7$K, where CNO is the dominant energy source above these temperatures in higher metallicity stars. The star contracts until temperatures are high enough ($\sim 10^8$ K) to initiate 3α reactions, thus producing a ^{12}C mass fraction of $\sim 10^{-10}$—sufficient to activate the CNO cycle (Ezer & Cameron, 1971). The time it takes for CNO to activate is inversely proportional to the initial mass of the star, with less massive stars having more of the main-sequence (MS) lifetime supported by p-p reactions and more massive stars generating the C necessary to supply CNO much earlier. This can be seen in Fig. 3.1 where red dots indicate the time at which CNO overcomes p-p chains as the dominant source of nuclear energy generation in the core. This has very important consequences for the structure of the star. It is overall more compact and the temperature for H-burning becomes closer to that of He-burning. This in turn leads to a smaller temperature difference between H- and He-burning layers than would be seen at higher metallicities. In Fig. 3.2 around 5.3 Myr this manifests itself as a smooth transition from H- to He-core burning.

In all of our simulations there are small convection zones above the H-burning

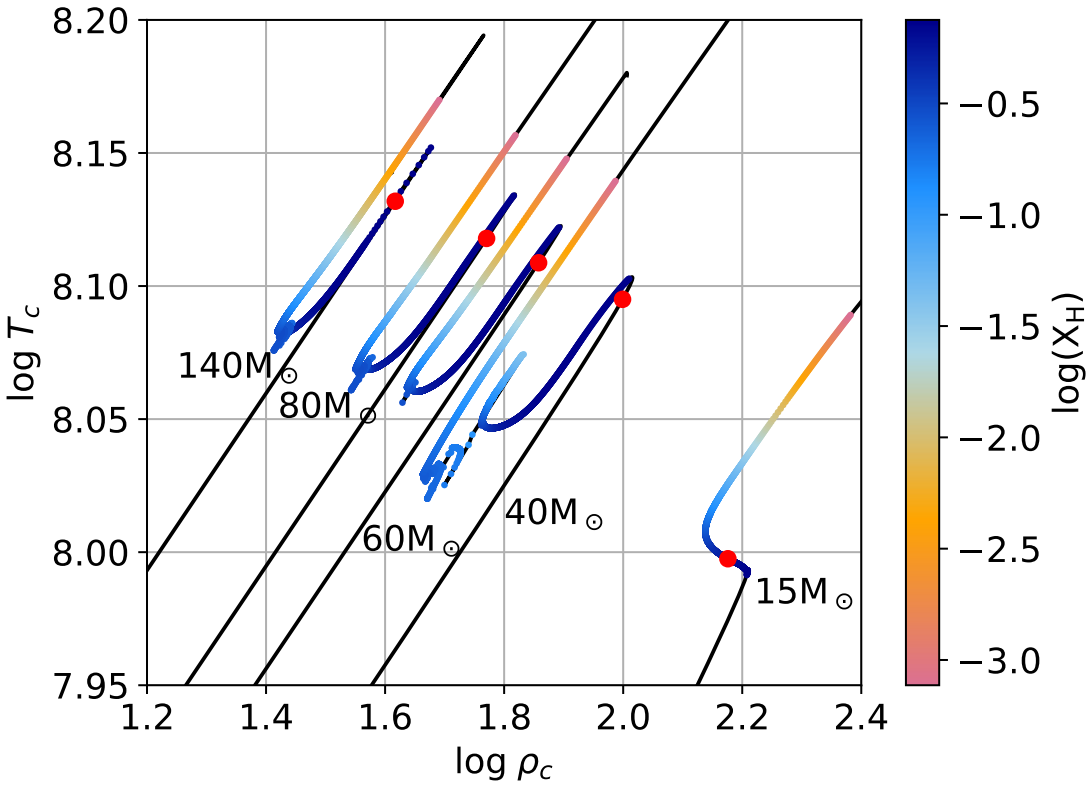

Figure 3.1: $\rho_c - T_c$ diagram for `schf-h` models using the Schwarzschild criterion for convection and our higher adopted value of CBM, where mixing of material into the H core occurs during the MS phase in models $\geq 40\,M_\odot$ **(see 3.4.1)**. Colours indicate the logarithm of the mass fraction of H remaining in the centre of the star. Red dots show the point in evolution at which CNO reactions overtake p-p chains as the dominant energy source in the centre.

core. These small convective 'fingers' present early in the MS phase—as soon as the H core begins receding—and descend downward during the MS (e.g. Fig. 3.2 above the convetive H core). These convective regions above the H-burning core are the result of composition changes induced by the receding core which ultimately produces a staircaising effect on the composition profiles (see, e.g. Schwarzschild & Härm, 1958; Langer et al., 1985; Heger et al., 2000). There is a small amount of p-p chain burning activity in these regions.

In simulations with masses $\geq 40\,M_\odot$, these convective fingers penetrate into the receding H core, injecting fresh hydrogen fuel from above. They are found in Fig. 3.2, above the H core, and in all other Kippenhahn diagrams presented in this work. The

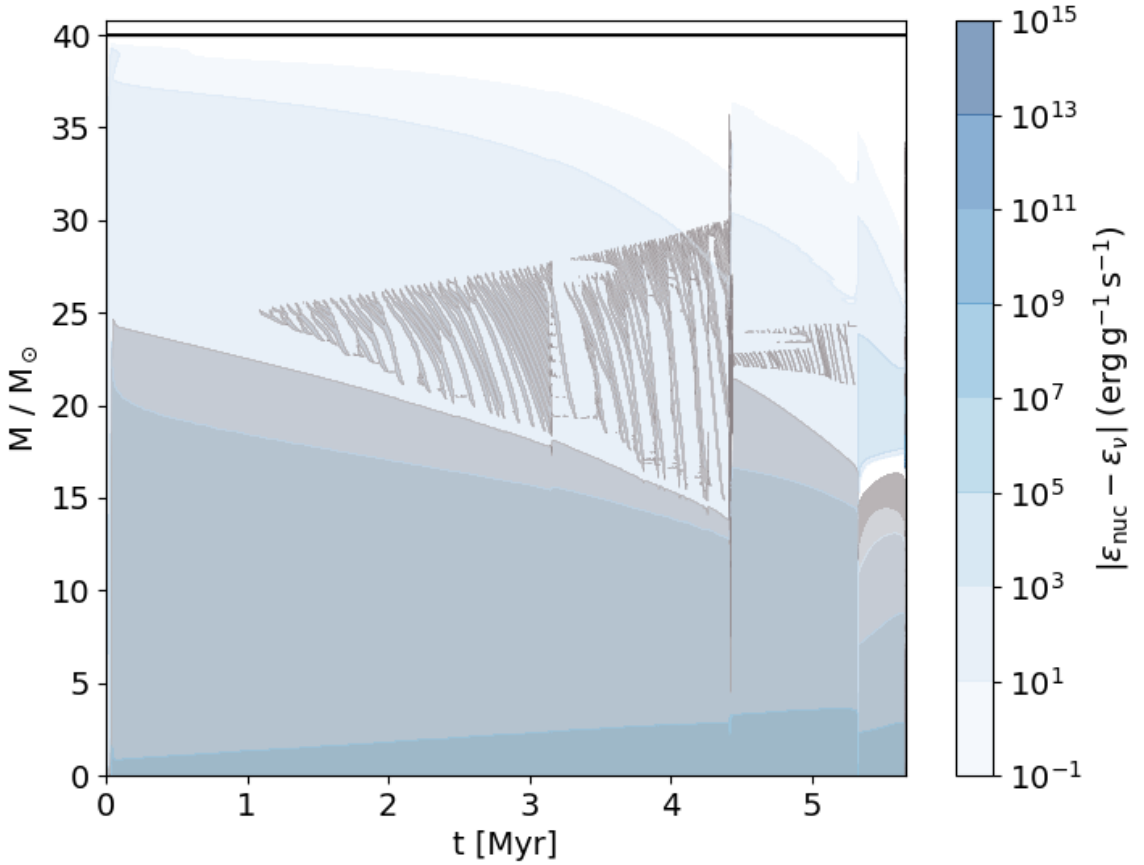

Figure 3.2: Kippenhahn diagram of the MS and beginning of He-burning in the `40Mschf-h` model with the Schwarzschild criterion for convection and $f_{\rm ov} = 0.01$. Gray areas indicate convection, blue contours show specific energy generation. An MS mixing event can be seen at $t \approx 4.4\,\mathrm{Myr}$.

most extreme examples found in our simulations are those with greater CBM and without the regulating effects of semiconvection—the `-schf-h` cases. This can be seen as jumps shown in Fig. 3.1 for all masses $\geq 40\,\mathrm{M}_\odot$ near the minimum $\rho_\mathrm{c} - T_\mathrm{c}$ value on the MS. In the `40Msch-f` model, within the span of $\approx 30,000\,\mathrm{yr}$ the mass fraction of H increases from 0.05 to 0.17 and the convective core expands both in mass and radial coordinates. 30,000 yr later, more mixing occurs and X_H increases to 0.25, further extending the MS lifetime, which can be seen at $t \approx 4.3\,\mathrm{Myr}$ in Fig. 3.2. This also causes a sudden increase in the luminosity. Similar behaviour was described by Farmer et al. (2016); Sukhbold et al. (2018); Kaiser et al. (2020). Farmer et al. (2016) found this in a solar metallicity model with an initial mass of $30\,\mathrm{M}_\odot$ using `MESA`. They found that this event appeared when using a high mass resolution but not their adopted low-resolution. Their adopted high and low mass resolutions for

this portion of the study are $\Delta M = 0.01$ and $0.02\,M_\odot$ per cell, respectively, and also include models with a maximum mass resolution of $0.005\,M_\odot$ per cell. For comparison, our mean mass resolution on the MS of the `40Msch-f` model is 0.008 $M_\odot$ per cell. Kaiser et al. (2020) found the presence of convective fingers decreased in frequency with $f_{\rm ov} \gtrsim 0.01$ and did not occur in stars of $15\,M_\odot$ at or above approximately this value. In our models, we find convective fingers in all of our simulations although core penetration does not happen in our $15\,M_\odot$ models. The difference in outcomes may relate to the differences in opacity and/or temperature gradients in Pop III vs. solar metallicity stars and/or our smaller range of CBM values.

While CBM itself will supply fresh H and increase the overall MS lifetime, the drastic H-mixing events in the models presented here can lead to MS lifteimes up to 20% longer relative to simulations of the same mass without them (see Table 3.1). This is greater than the $\approx 5\%$ increase reported by Farmer et al. (2016) which may be due to the difference in our maximum CBM parameter of 0.01 and their value of 0.001. Moreover, in our simulations the convective fingers above the H core are present in most models using CBM but is less extreme when semiconvection and the Ledoux criterion are used. These relevant physics choices are used by Farmer et al. (2016) in all simulations. While including Ledoux and semiconvection at this evolutionary stage appears more physical, we do not find there to be any other notable impact from these dramatic MS mixing events on the behaviour of later H-He interactions and regard them as numerical artefacts.

A comparison of the `15Mschf-h` and `40Mschf-h` models indicates that this mixing on the MS may be related to the overall compactness, temperature gradients above the H cores and the associated nuclear feedback. More specifically, a $15\,M_\odot$ Pop III star has lower central temperatures than its more massive counterparts, and thus, more time on the MS spent in p-p chain burning (17% vs 0%) and lower energy generation from CNO reactions. Simultaneously, the $15\,M_\odot$ simulation has nearly 2 times higher core and overall densities during the MS. Overall, the `15Mschf-h` model is a more compact star with steeper entropy gradients which may act to inhibit the mixing on the MS seen in higher mass models.

3.4.2 Shell H-Burning

H-burning products that will carry over to subsequent stellar generations are produced primarily in H-burning shells. In Pop III stars, H-burning shells tend to be hotter

than in their higher metallicity counterparts for reasons presented in Section 3.4.1. All simulations presented in this work have convective H-burning shells for at least a portion of the post He-core burning phase.

Table 3.1 lists the maximum H-shell burning temperatures found in our grid of models. This is the maximum temperature at the lowest mass coordinate where the H mass fraction is at least 10^{-4}. If there is a H-He interaction, the maximum H-burning temperature reflects how far into the He shell the H-rich material descends by the end of the simulation. This distance the H-burning shell has advanced into the He-rich region, $\Delta M/\mathrm{M}_{\odot}$, is also reported in the final column of Table 3.1.

In simulations over $15\,\mathrm{M}_{\odot}$, the H-shell temperature increases over time. The `15Mled` and `15Mledf-l` runs both have the maximum temperature at the beginning of H-burning and decrease by about $10^7\,\mathrm{K}$ by the end of the simulation. Otherwise, the maximum temperatures are found either at the end of the simulation in those that do not have an H-He interaction, or during a H-He interaction. For the `140Mled` run, the maximum temperature of the H shell is measured prior to encountering the pair instability, as is described below in Section 3.5.5.

H-He interactions can have significant effects on the physical conditions and nucleosynthesis within H-burning shells. The details of the nucleosynthesis are described in Section 3.5 and Section 3.5.6.

3.4.3 Hot CNO

The activity of hot CNO cycling, and possible breakout therefrom, may have important implications for the abundances found in the second generation of stars. Core- and shell-H burning conditions can be investigated relating to CNO breakout in the four models that do not experience a H-He interactions.

The first hot CNO cycle occurs when protons preferentially capture on the ^{13}N nucleus before it can decay into ^{13}C, which begins at temperatures of $\sim 1 \times 10^8\,\mathrm{K}$ (Wiescher et al., 2010) for sufficiently high densities. This leads to the bypass of the ^{13}N β^+ decay, and energy generation is controlled by the β^+ decays of ^{14}O and ^{15}O, the slowest reactions in the cycle. During core contraction on the MS in each of our four simulations without a H-He interaction, the conditions become hot and dense enough such that hot CNO conditions are temporarily met. This is indicated by the production of ^{14}O from the $^{13}\mathrm{N}(p,\gamma)$ reaction, with a lifetime, τ_p, that becomes shorter than the beta decay lifetime. Hot CNO conditions last for $\sim 1\%$ of the total

MS lifetime and $< 1\,\mathrm{yr}$ at most during H-shell burning in our simulations. Therefore, cold CNO dominates over hot CNO for both core and shell H burning in the `15Mled`, `80Mled`, `140Mled`, and `60Mled-l` simulations.

While hot CNO cycles are effectively closed at these temperatures (Iliadis, 2007), all our `MESA` simulations show small amounts of elements with charge $Z \geq 10$, being produced during H burning. The greatest of these is Ca, owing to its doubly magic nature, with an average mass fraction of no greater than about 10^{-12} in the H-rich envelope. 98% of the Ca in the H-burning shell in the four simulations we examine is produced during the MS. Table 3.1 shows our highest H-burning temperature is found in the `80Mled` model where the peak temperature is reached during the last day of simulation time. Fig. 3.3 shows the most abundant elements and Ca for the final time step. All of the simulations presented in this work have convective H-burning shells. Post core-He burning in the `80Mled` model, the H-rich convection zone extends from $\approx 35\,\mathrm{M}_\odot$ to $\approx 70\,\mathrm{M}_\odot$. After core-O burning, this convection extends nearly to the surface of the model, bringing with it any H-burning material present.

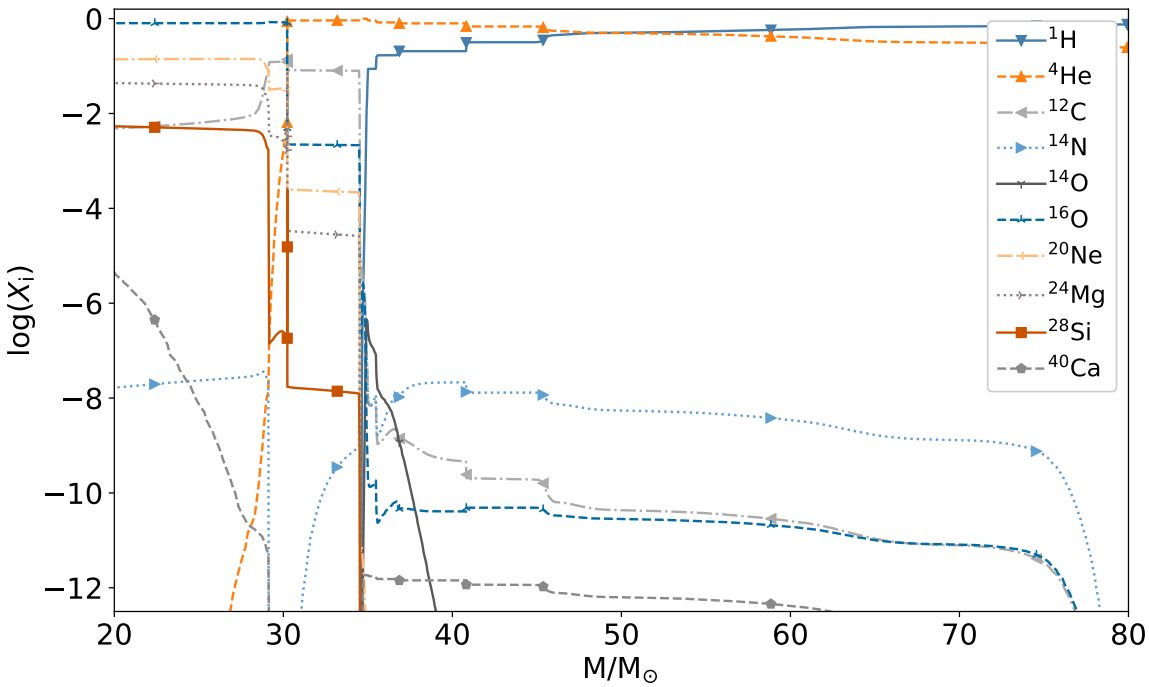

Figure 3.3: Mass fractions of the most abundant species and Ca for the final model of the `80Mled` model with the Ledoux criterion and semiconvection. Plot extends from the middle of the C-shell to the surface.

Hot CNO breakout reactions are reported by Keller et al. (2014); Nordlander et al. (2017) and Takahashi et al. (2014) as the production site for the Ca in Pop III stellar evolution models. Those yields have been used to match the abundances observed in Ultra Metal-Poor CEMP-no stars. Clarkson et al. (2018) found that the i process was the primary source for Ca in their simulations.

Table 3.3: Single-zone calculation parameters.

Description	$T\,(10^8\mathrm{K})$	$\rho\,(\mathrm{g\,cm^{-3}})$
`80Mled` H-core average	1.19	39.8
`80Mled` H-core maximum	1.36	65
`80Mled` H-shell maximum	2.34	1.77

To determine the sequence of breakout reactions and reactions leading to the production of Ca, we have run three constant temperature and density single-zone calculations using the `PPN` code (Pignatari et al., 2016). These calculations use the same network as described in Clarkson et al. (2018) but are run with the time-weighted average temperature for core H burning, maximum temperature for core H burning, maximum temperature for H-shell burning, and corresponding densities. The temperature and densities used are given in Table 3.3.

For both of the core H burning `PPN` runs, we find that the small amount of breakout that occurs, flows primarily through $^{16}\mathrm{O}(p,\gamma)^{17}\mathrm{F}(\beta^+\nu)^{17}\mathrm{O}(p,\gamma)^{18}\mathrm{F}(\beta^+\nu)^{18}\mathrm{O}(p,\gamma)$ $^{19}\mathrm{F}(p,\gamma)^{20}\mathrm{Ne}$ with a small contribution from proton captures and subsequent decays on $^{17}\mathrm{F}$ and $^{18}\mathrm{F}$. Here it should be noted that the flux, $\mathrm{d}Y_i/\mathrm{d}t$, of the $^{18}\mathrm{F}(p,\alpha)^{15}\mathrm{O}$, $^{18}\mathrm{O}(p,\alpha)^{15}\mathrm{N}$ and $^{17}\mathrm{O}(p,\alpha)^{14}\mathrm{N}$ reactions are $\approx 10-4,000$ times greater than competing breakout reactions and decays under these conditions. More importantly, the flux through the $^{19}\mathrm{F}(p,\alpha)^{16}\mathrm{O}$ is $\approx 5,500$ times greater than through the competing $^{19}\mathrm{F}(p,\gamma)$ channel, keeping most material within the CNO. For the small amount of material that can make it past F, proton captures and decays along the valley of stability lead to a small production of Ca with mass fractions no greater than 10^{-12}.

Investigating the maximum H-shell temperatures from our `80Mled` simulation, we find a somewhat different story. In addition to the aforementioned reactions, $^{15}\mathrm{O}(\alpha,\gamma)^{19}\mathrm{Ne}$ occurs at these temperatures, although the competing flux through the decay of $^{15}\mathrm{O}$ is $\sim 10^7$ times greater, making its contribution completely negligible. As in the previous two simulations described, material passes through $^{17}\mathrm{F}(\beta^+\nu)$ and $^{18}\mathrm{F}(p,\gamma)^{19}\mathrm{Ne}$, but at these higher temperatures, some is able to bypass $^{19}\mathrm{F}$, when decays and proton captures lead this flow to $^{21}\mathrm{Ne}$ and $^{23}\mathrm{Na}$. The fluxes through

breakout reactions we have discussed are in the range $\sim \times 10^{-23} - \times 10^{-18} \mathrm{s}^{-1}$. Any occurring hot CNO breakout during shell H-burning has little impact on the Ca abundance due to the limited time prior to collapse. Takahashi et al. (2014) reported temperatures over 4.5×10^8 K leading to hot CNO breakout in a 140 $M_\odot$ simulation during shell H burning. We cannot confirm this result as the single 140 $M_\odot$ simulation we have without a H-He interaction, the `140Mled` case, becomes pair-unstable. The maximum temperature in the H shell before the instability occurs is 2.18×10^8 K.

To determine wether this Ca production can explain the Ca abundances in the most Fe-poor stars, we compare the [Ca/H] value of -6.94 given in Nordlander et al. (2017) for the most Ca-poor star currently known, SMSS 0313-6708 (Keller et al., 2014) with calculated values from `MESA` simulations presented here. Performing a simple calculation, we use solar abundances from Asplund et al. (2009) and assume a faint supernova. We calculate abundances using:

$$X_{\mathrm{total}} = \frac{\int_{M_\mathrm{B}}^{M_\mathrm{tot}} X dm}{\int_{M_\mathrm{B}}^{M_\mathrm{tot}} dm} \tag{3.1}$$

Where X is the mass fraction of a given isotope, M_tot is the mass coordinate corresponding to the surface of the star, and M_B is the mass coordinate corresponding to the base of the H envelope. We do not include nucleosynthetic contribution from the explosion or any subsequent mixing. We also do not include any dilution from the ISM and therefore, our estimates represent the maximum [Ca/H] value that can be obtained by these simulations given the aforementioned assumptions. We find [Ca/H] values of -7.92, -7.72 and -8.91 for the final models of our `80Mled`, `60Mledf-l` and `15Mled` simulations, respectively. Therefore, the observed Ca abundance is between ~ 0.8 and nearly 2 dex larger than the largest amount of Ca made by hydrostatic H burning in these models.

If the branching ratio for $^{19}\mathrm{F}(p,\gamma)/^{19}\mathrm{F}(p,\alpha)$ were a factor of $\approx$ 10 higher, this would help relieve the tension. In our `PPN` simulation using the maximum shell temperature from the `80Mled` model, increasing the $^{19}F(p,\alpha)$ rate by a factor of 10 results in an increase in the Ca abundance of 1 dex. Though recent measurements of the $^{19}F(p,\alpha)$ rate (Lombardo et al., 2019) and investigations into $^{19}F(p,\gamma)$ (Couture et al., 2008), which have not been adopted in this work, both suggest a lower branching ratio than used in this work by at least a factor of 10, which we expect to lower the abundance of Ca created in simulations.

3.5 H-He Interactions

We investigate the occurrence and behaviour of convective H-He interactions in our stellar evolution models. Table 3.1 lists which type of interaction occurs in each simulation. 22 out of 26 simulations have H-He interactions. In all cases the H-burning layers are convective. The H-burning convective shell can interact either with core or shell He burning. The He-burning core or shell can be either radiative (`Rad`) or convective (`Conv`). In our simulations we find examples of all of these four combinations, which we label `Rad-Shell` for H-shell material mixing with a radiative He-shell, `Conv-Shell` for a convective He-shell, and likewise `Rad-Core` and `Conv-Core` for H-rich material interactions with the radiative region above the He-burning core or with the convective core itself, respectively.

We define H-He interactions as a region where $X_{\rm H}$ increases rapidly (over several time-steps) to $> 10^{-4}$ due to mixing over any radial portion of a He-rich layer. This choice is made to properly recover H-He interaction properties. When protons are being mixed into convective He layers they are transported downward and able to react with the ashes of the He-rich fluid. For example, in the `80Mscf-h` case, described in Section 3.5.4, where protons are mixed into a convective He core, energy generation from CNO reactions dominates over that from triple-α reactions by several orders of magnitude if the H mass fraction is at least $> 10^{-4}$. Therefore, we use this value for consistency in all calculations and measurements requiring the location of the 'base' of the H-rich material.

We describe the evolution of four models in detail, one for each mode listed in Table 3.1, and briefly describe other simulations of note. In order to gain insight into the energetic feedback from nuclear reactions during a H-He interaction, we adopt the H number as given in Jones et al. (2016) defined as:

$$H = \epsilon_{\rm nuc}\tau_{\rm conv}/E_{\rm int} \tag{3.2}$$

This number is an estimate of the energy being deposited into the flow from nuclear reactions relative to the specific internal energy. The convective advection timescale, $\tau_{\rm conv}$, is the shortest timescale over which energy can be transported by convection. This is calculated as the pressure scale height at the base of the convective H-rich layer divided by the maximum local convective velocity. This is then compared to the local internal energy, $E_{\rm int}$. For a general equation of state, $\phi E_{\rm int} = -E_{\rm g}$. For

the case of an ideal gas $\phi = 2$, and for a photon gas $\phi = 1$. As with most massive stars, massive Pop III stars have a non-negligible radiation contribution to their equation of state. In the absence of other considerations, this shows that it becomes increasingly easy to unbind material with an increasing contribution of radiation to the total pressure. Therefore, the H number can be interpreted as an indication of how far from hydrostatic equilibrium the simulation is. It should be noted that when these numbers are calculated, many models have already violated the assumptions of MLT, and H numbers are to be taken as instructive. In general, convective shell interactions with larger H numbers are in principle more likely to lead to ejections compared to cases with lower H number. However, the 3D fluid-dynamics of the event would be an additional determining factor. For example, dynamic instabilities such as the global oscillation of shell H-ingestion (GOSH) reported by Herwig et al. (2014) could lead to focused non-spherical ejections into a confined solid angle. This would require only a fraction of the binding energy of the complete 4π shell of mass ΔM for successful partial ejection. Given these uncertainties, we refrain from making specific predictions regarding which H numbers will lead to mass ejection.

When H-He interactions begin, time steps rapidly decrease and the simulations fail to converge. Up to this point, the models describe the sequence of events leading up to these interactions. We do not include any 'stellar engineering' parameter modifications to continue the evolution through the violent phases, as in most cases the assumptions of 1D stellar evolution are no longer appropriate, for example in the case of high H number.

To determine whether convective-shell interactions were caused, as opposed to influenced, by any type of boundary mixing we ran one simulation, `140MNoMix`, that uses the strict Schwarzchild criterion. Also in this case a `Conv-Core` interaction is observed.

Some commonalities can be found in these simulations not specific to any of the cases described below. For example, H-He interactions are initiated during core contraction phases from the beginning of core He burning to the onset of core O-burning. We also find that H always moves downward first, but in many simulations C and other He-burning products move upward into the H shell as well. This can boost mass fractions of CNO elements, having implications for the distribution of observed $^{12}C/^{13}C$ ratios in second generation stars (Choplin et al., 2017). Energy generation and the H number tend to depend on the amount of He burning that has occurred in the He-rich layer, as this dictates the ^{12}C abundance which interacts with the protons

from the H-shell.

3.5.1 Convective H Shell and Radiative He Shell

`Rad-Shell` interactions take place in nearly half of the models presented in this work. This interaction type takes place sometime after core He-burning and in it, a convective H-burning shell descends downward into a previously H-free radiative He burning shell. Notably, this interaction type is only seen in models with CBM included.

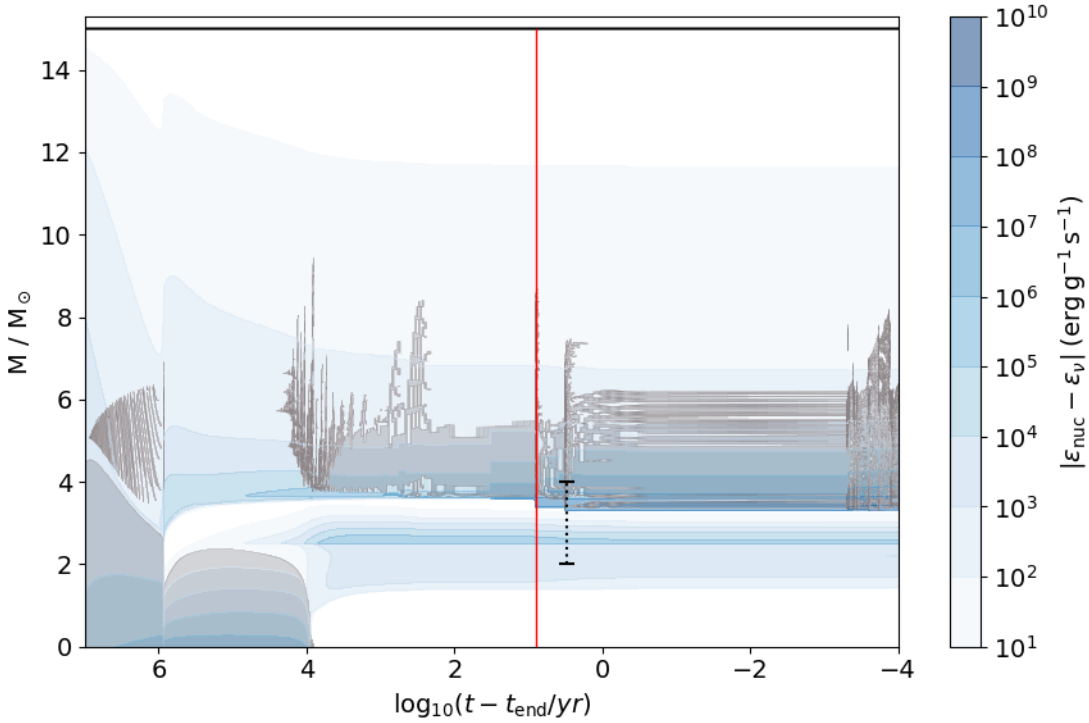

Figure 3.4: Kippenhahn diagram of the total calculated evolution of the `15Mschf-h Rad-Shell` case, using the Schwarzschild criterion for convection and $f_{ov} = 0.01$. Colours are the same as in Fig. 3.2. The red line indicates the beginning of the H-He interaction and the black dotted line indicates where the profiles in Fig. 3.5 are taken.

We use the `15Mschf-h` simulation as a representative case for this type of interaction. Fig. 3.4 shows the total evolution of the simulation until ~ 5 min before the simulation ends. As with all the $15\,M_\odot$ simulations, convective mixing into the H core, as described in Section 3.4, does not occur on the MS. At the end of core He burning the inner regions of the star contract to initiate core C burning, creating a convective H shell atop a radiative He shell. As the H shell begins developing, sev-

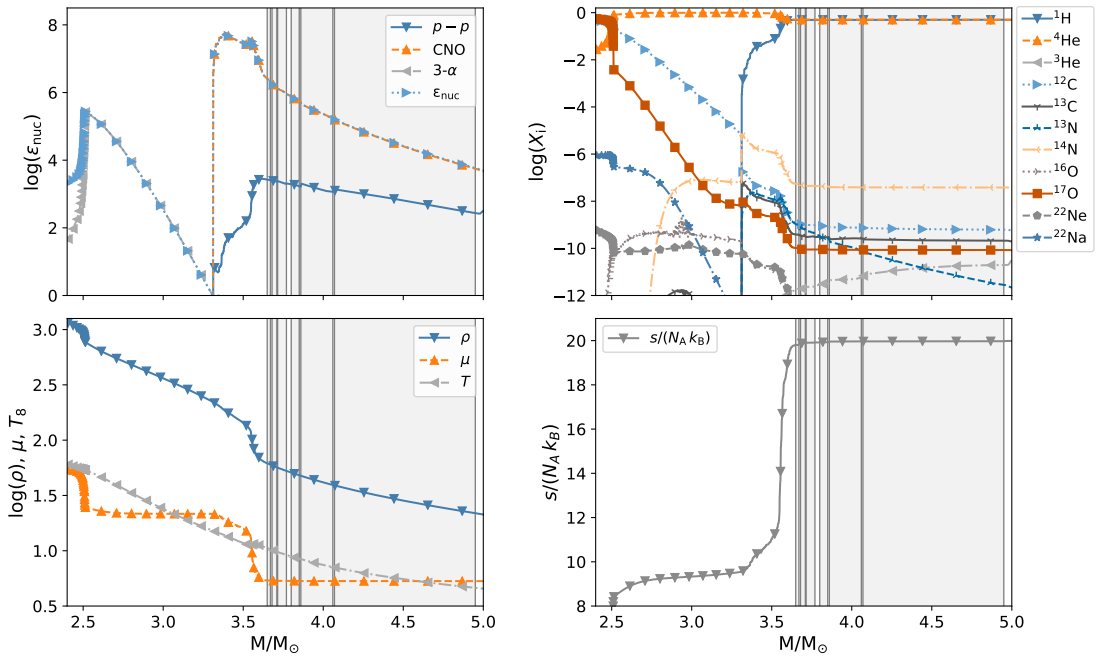

Figure 3.5: `15Mschf-h` as an example of an `Rad-Shell` He interaction. **Top left**: Total specific energy generation and that from CNO, p-p and tri-α reaction groups. **Top right**: Mass fractions of several abundant species. **Bottom left**: Temperature ($T_8 \equiv T/10^8\,\mathrm{K}$) , mean molecular weight and density profiles. **Bottom right**: Specific entropy. Profiles taken $\approx 5\,\mathrm{yr}$ after H-He interaction begins, times for which are indicated in Fig. 3.4 as black dashed and solid red lines, respectively. Grey areas show regions unstable to convection. See A for profiles of diffusion coefficients.

eral small, convectively unstable regions merge, spanning over $1\,\mathrm{M}_\odot$ in Lagrangian space. As this happens, the He shell temperature increases and energy generation from triple-α reactions causes the region to expand and push toward the H-burning convection zone. Simultaneously, over the course of $\approx 2 \times 10^4\,\mathrm{yr}$ the H shell descends inward until it reaches the top of the previously H-free core (at $\log(\mathrm{t} - \mathrm{t_{end}}) \approx 3.5$ in Fig. 3.4). The effective CBM region at the base of the H shell during this time is $\approx 0.07\,\mathrm{M}_\odot$. Small amounts of protons begin to mix at the top of the expanding He shell, and C and O are mixed upwards into the H-shell. Abundances of ^{12,13}C, ^{13,14}N and^{16}O increase in mass fraction by about 1 dex within 1000 yrs. The addition of catalysts to the H-rich material creates non-equilibrium CNO abundances which are nearly restored within 6 months. This upset and partial restoration to equilibrium continues for the 8 yr duration of the simulation as new ^{12}C is introduced to the H-

rich material. Fig. 3.5[2] also shows that within about 5 yr, much of the ^{12}C which was mixed into the H shell has been converted to ^{14}N, and this ^{14}N is also mixing down into the He shell. Elements heavier than O are not produced in the H-burning layer at mass fractions $> 10^{-12}$. With both values of CBM this interaction type happens in 15$M_\odot$ simulations using both convection criteria. H-He interaction does not occur for this mass in models without any CBM. For a timespan of 600 yr, ingression of the proton rich material into the previously H-depleted radiative layer reaches down 0.06 $M_\odot$. This creates a small shelf in the entropy profile likely due to the change in mean molecular weight and CNO energy generation, as can be seen in the early stages at a $M/M_\odot \approx 3.5$ in Fig. 3.5. The convective H-rich material then penetrates downward in mass coordinate to 3.34 $M_\odot$ and then 3.3 $M_\odot$ within 3.2 yr before the simulation stops. In this time, the specific energy generation from CNO in the region has increased from $\sim 10^6$ erg g^{-1} s^{-1} prior to the event to $10^{8.6}$ erg g^{-1} s^{-1} at the final model.

Also of note is the `40Mschf-h` case presented in Section 3.4.1. In this simulation, unlike the `15Mschf-h` case and most others of this type, the H-rich material eventually penetrates all the way to the bottom of the radiative He shell releasing large amounts of energy, as indicated by the maximum H number of 0.35 listed in Table 3.1 and $\epsilon_{\rm nuc}$ contours in Fig. 3.6. The H-shell boundary moves from a mass coordinate of 18.5 $M_\odot$ to 17 $M_\odot$ over a time span of 502 yr at which point the energy generation at the base of the H shell is $\sim 10^9$erg g^{-1} s^{-1} and the ^{12}C abundance is $X_{^{12}\rm C} = 10^{-4.6}$. Within another 35 yr, the H-shell boundary moves downward another 0.3 $M_\odot$ where the mass fraction of ^{12}C abundance is now $X_{^{12}\rm C} = 0.31$ and the specific energy generation has increased to $\sim 10^{13}$erg g^{-1} s^{-1}. In this case, the temperature is 1.1×10^8 K at the maximum H-penetration point.

Table 3.1 shows that H can vary dramatically between simulations with `Rad-Shell` interactions. The primary difference in the simulations which have lower vs higher values of H seems to be the abundance of ^{12}C in the He shell the hydrogen is able to interact with. In the `15Mschf-f` model the mass fractions of ^{12}C and protons where they meet are $X_{^1\rm H} \approx 3 \times 10^{-3}$ and $X_{^{12}\rm C} \approx 2 \times 10^{-6}$. If H only penetrates the upper layers of a radiative He shell, one does not expect the very high energy generation created when it reaches the bottom of the shell, where C is much more abundant,

[2]Note that grey regions in all panel plots of this type throughout this work show the approximate location of convection zones. Once a H-He interaction has begun, convective regions as reported by `MESA` often break up into many small, frayed zones. Therefore, we plot the innermost and outermost points of the largest zones. For profile of diffusion coefficients See Appendix A

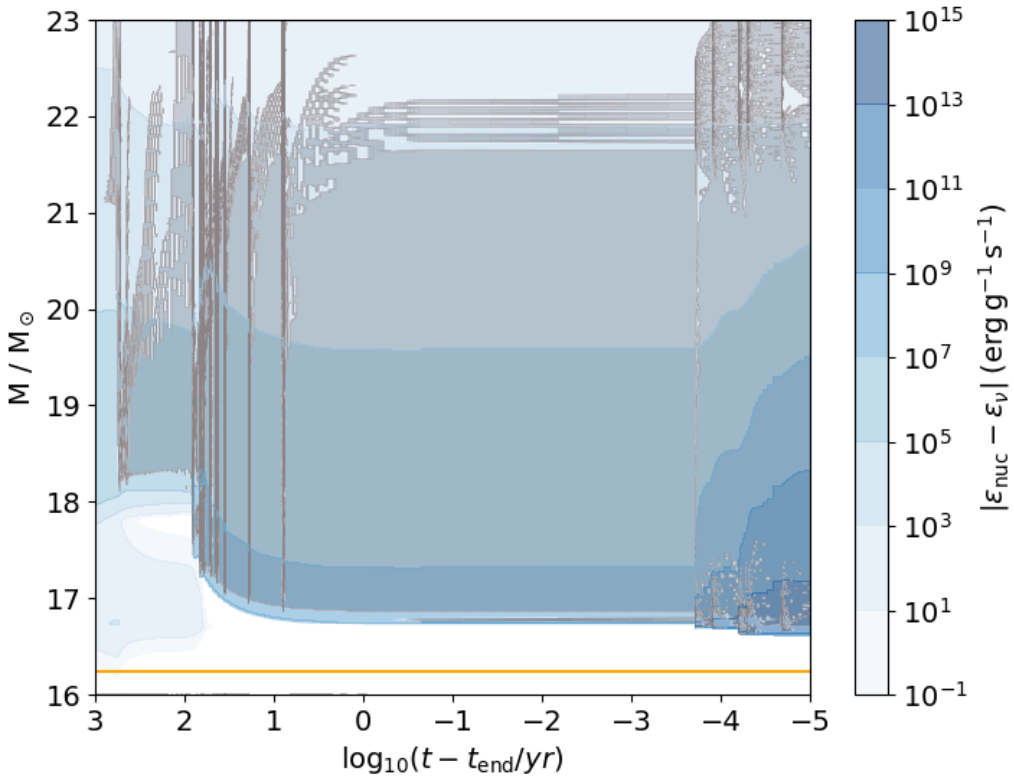

Figure 3.6: Zoom-in Kippenhahn diagram of H-He interaction in the `40schf-h Rad-Shell` case which includes the Schwarzschild criterion for convection and f_{ov} = 0.01. Colours are the same as in Fig. 3.2. The convective region is H-rich and the orange line shows the He-free core boundary.

such as in the `40Mschf-h` case.

The `Rad-Shell` interaction type bears similarity to dredge up events seen in AGB and super-AGB stars. Herwig (2004) showed that in models with assumed CBM, protons mixing inward and reacting with ^{12}C causes the peak energy generation to be below the convective boundary, and ultimately leads to corrosive penetration into the radiative core. This same effect is shown in Fig. 3.5 and occurs in all our `Rad-Shell` interactions. Jones et al. (2016, and references therein) show that not applying CBM at the lower boundary of the convection zone still results in a dredge-out episode. Furthermore, they demonstrated that CBM can lead to inward corrosive burning.

3.5.2 Convective H Shell and Convective He Shell

The `40Mled` and `60Mled` simulations undergo an interaction between a convective H-burning shell and convective He-burning shell. In both, the H-He interaction occurs as carbon is exhausted in the core. This is the same mode of interaction reported in Clarkson et al. (2018) for a $45M_{\odot}$ model. For this type of H-He interaction the `40Mled` model is used as a representative example and the overall evolution is shown in Fig. 3.7. After core He-burning, the inner regions of the star contract, igniting a convective He burning shell and the core begins burning C. As this happens, the H-burning shell is temporarily halted in its downward descent by the expansion of the He-burning shell below. 3000 yr after the He-burning shell becomes convective, a small portion of the convective He shell splits. This splitting can be seen in Fig. 3.8 at $M/M_{\odot} \sim 14.2$. A similar small convection zone is located at the base of the H-shell. It is uncertain at this time whether such splitting of convection zones is simply an artefact of 1D mixing assumptions or if similar features may be also be found in 3D hydrodynamic simulations. Approximately three weeks after this split forms, H-burning shell material begins mixing into the radiative layer separating the two convection zones, or intershell region, as indicated by the increase in nuclear energy generation at the base of the H shell along with an increase in the abundances of ^{1}H, ^{13}C and ^{13}N in the intershell, and later at the top of the He shell. In this case, H is initially ingested into the intershell region and 7 yr later, He-burning products mix upward into the H shell as well, indicated by an increase in CNO nucleosynthetic products seen in the top right panel of Fig. 3.9. Only 12.6 min after the event begins, the energy generation rate from CNO reactions has increased to $\log \epsilon_{\rm CNO} = 11.6$. At later times protons have to some extent mixed through much of the He shell.

After the initial interaction, small entropy steps within the intershell mix, leaving a new, ever descending barrier for the remainder of the simulation, which is 5.6 hr. In the bottom right panel of Fig. 3.9, this entropy barrier can be seen in addition to the fact that this barrier is not preventing mixing between the H and He-rich layers. As a reminder to the reader, the `40Mled` model does not include the effects of CBM. The peak specific energy generation in the H-He interaction is $\log \epsilon_{\rm CNO} = 13.25$.

This interaction type is among the more energetic which can be seen in the maximum H numbers reported in Table 3.1, 0.22 and 0.28. The high energy generation is the consequence of protons being convectively mixed into the He burning shell, rather than a slow corrosive type burn as seen in `Rad-Shell` models where H-rich material

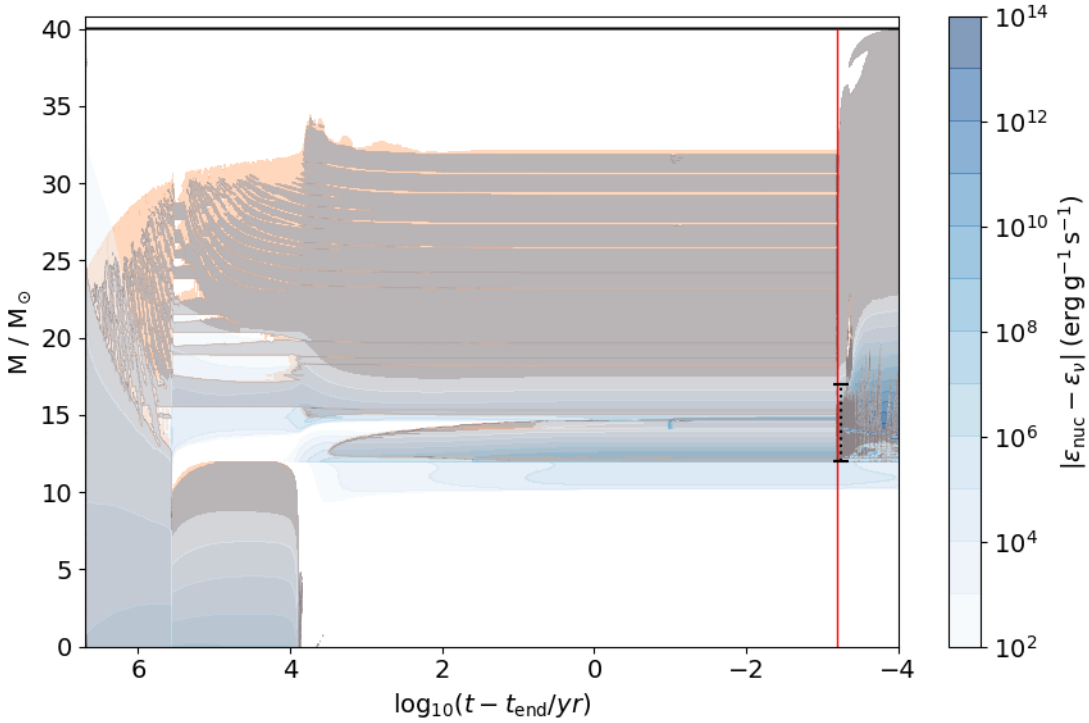

Figure 3.7: Kippenhahn diagram of the whole calculated evolution of the `40Mled Conv-Shell` case, using the Ledoux criterion for convection and $\alpha_{\rm semi} = 0.5$. Colours are the same as in Fig. 3.2 and peach areas show where semiconvection has been applied. The red line indicates the beginning of the H-He interaction and the black dotted line indicates where the profiles in Fig. 3.9 are taken.

encroaches into a radiative He-burning layer.

The presence of convection in the He shell leads to a higher C abundance at the top of the shell, as compared to a radiative He shell, and causes the downward mixing of protons to higher temperatures. The i process occurs when H is convectively mixed into a C-rich environment on a timescale comparable to the decay of ^{13}N. It begins with the ^{12}C$(p,\gamma)^{13}$N reaction. ^{13}N then β^+ decays to ^{13}C while being transported to higher temperatures where the ^{13}C$(\alpha,n)^{16}$O is strongly activated. In these simulations we treat the emergence of the neutron source consistently with the mixing processes. We also include n-capture reactions at least one isotope away from the valley of stability up to V. Since n-capture reactions for heavier and trans-iron element are missing the resulting neutron density is an upper limit. However, the main source of uncertainty comes from the treatment of convective mixing and the stellar evolution response in 1D. Denissenkov et al. (2019) demonstrated that the entrainment rate of

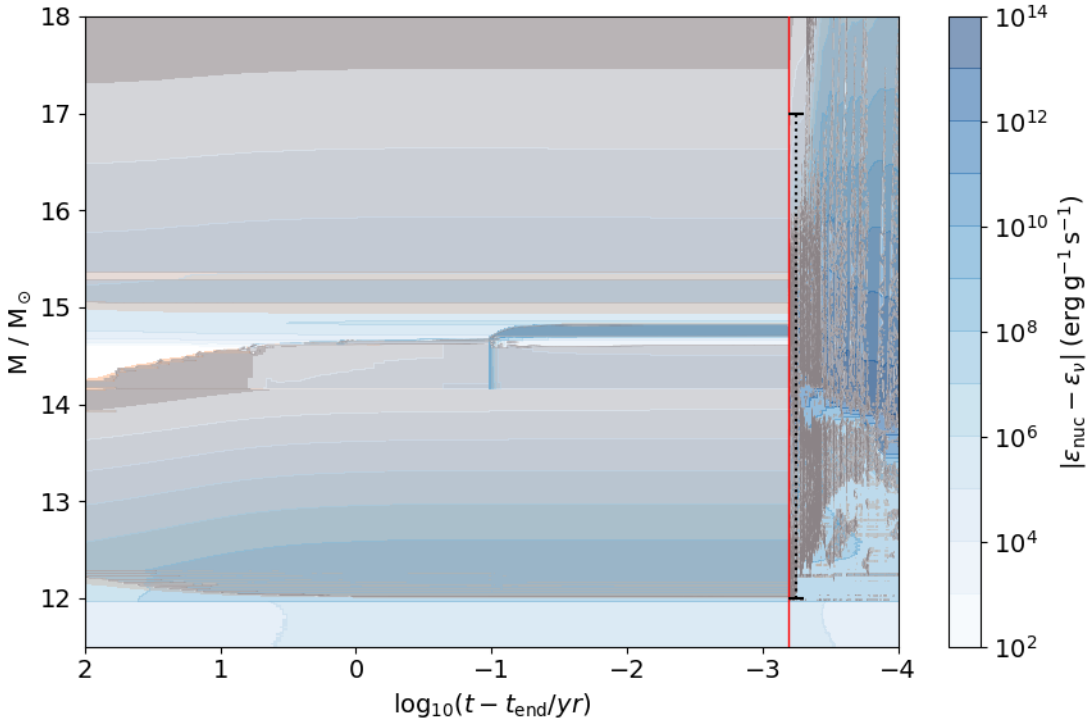

Figure 3.8: Zoom-in of Fig. 3.7. Colours are the same as in Fig. 3.2 and peach areas show where semiconvection has been applied. The red line indicates the beginning of the H-He interaction and the black dotted line indicates where the profiles in Fig. 3.9 are taken.

H into the He shell will strongly influence the neutron density for the i process in the case of rapidly accreting white dwarfs, therefore we report a number only indicative of what the neutron density might be.

3.5.3 Convective H Shell and Radiative Layer Above He Core

This interaction type occurs in 3/26 simulations and is characterized by H-rich material entering the radiative layer above the convective He-burning core in the later stages of core He-burning. While similar, this differs from `Conv-Core` interactions in that it occurs at a later evolutionary phase and the H-rich material never enters the convective core. Similar to the `Rad-Shell` models, it occurs only in models with CBM. The `140Mledf-h` simulation, which used the Ledoux criterion for convective stability, semiconvection and our higher value of CBM is described for this case and the overall evolution is shown in Fig. 3.10. During core He-burning, a small H-burning

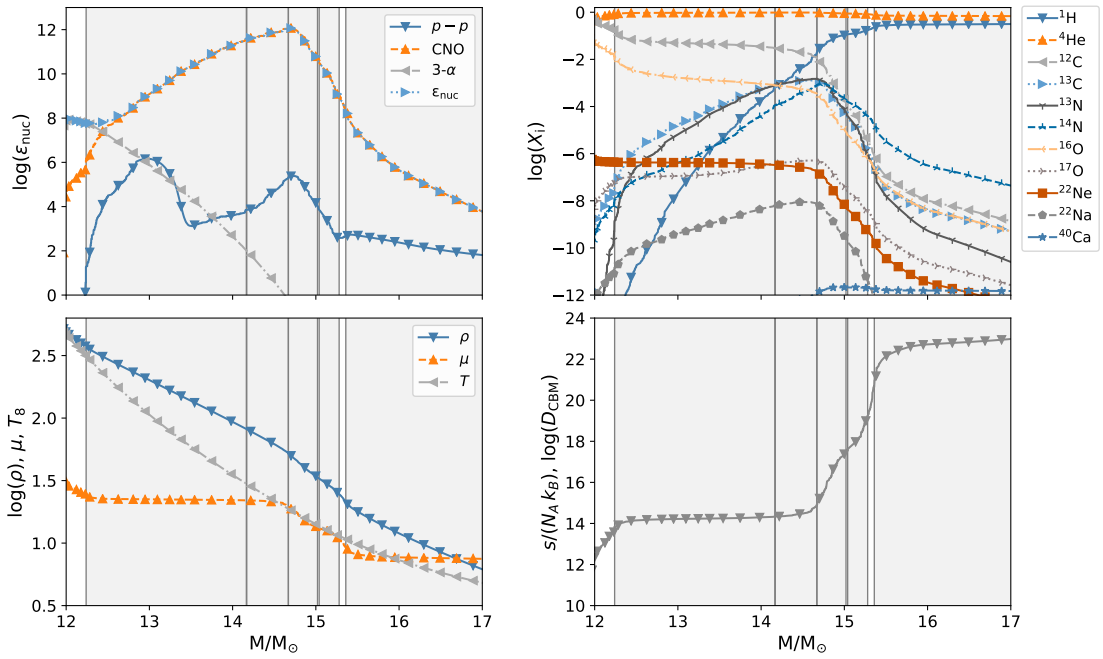

Figure 3.9: Profiles for the `Conv-Shell` interaction `40Mled` model with the Ledoux criterion for convection and semiconvecton included. **Top left**: Total specific energy generation and that from CNO, p-p and tri-α reaction groups. **Top right**: Mass fractions of several abundant species. **Bottom left**: Temperature, mean molecular weight and density profiles. **Bottom right**: Specific entropy. Profiles shown are 40 min after the H-He interaction begins in the `40Mled` model, times for which are indicated in Fig. 3.7 as black dashed and solid red lines, respectively. Grey areas show regions unstable to convection. See A for profiles of diffusion coefficients and similar profile plot before interaction occurs.

convection zone, as described in Section 3.4.1, descends downward over the course of 1.8×10^5 yr. In this time, the core contracts by about $0.2 R_\odot$ and the base of the H shell has a relevant CBM region of $0.1 - 0.6\,M_\odot$. The H shell begins to descend into the previously H-free region, with protons mixing into the radiative layer atop the He core. The convective core moves down in tandem with the shell for 4.5×10^5 yr. Shortly after, core convection effectively ceases, which can be seen in that last hour of the simulation in Fig. 3.10. The ceasing of core convection is seen in all three `Rad-Core` interactions.

Just before core convection stops, the CBM region at the base of the H shell begins to extend over the region which was previously the convective core. Then, convection in the H shell brings He-burning ashes upward. The introduction of large amounts of C and O into the H shell from the He shell pushes the CNO cycle out of equilibrium. In this simulation, energy generation from CNO increases up to $\log \epsilon_{\rm CNO} = 12.5$. We do not see a return to CNO equilibrium for the duration of the simulation. A similar chain of events takes place in the `40Mschf-l` simulation although in the `40ledf-h` simulation, the H shell never descends low enough to bring up material from the previously convective core. In the `140Mledf-h` simulation, the upward mixing of He-core material triggers Ne-Na and Mg-Al cycles in the mixing region. Evidence for this can be seen in the top left panel of Fig. 3.11 showing nuclear energy generation from reactions involving Na, Ne and Mg and the top right panel shows this mixing and nucleosynthesis 54 min after the event has begun. ^{22}Na has a half-life of 2 yr and is being produced in-situ in the convective mixing region. Based on elemental ratios for the region at the end of the simulation, this nucleosynthesis does not remove the odd-even effect as is observed in some of the most iron-poor stars (e.g. HE1327-2326 and HE0107-5240) but may somewhat lessen it. It is also interesting to note that if such an interaction were to occur and the core were to remain convective, the i process may be effectively triggered, although 3D hydrodynamic investigations are needed to confirm this. In Maeder & Meynet (2015); Choplin et al. (2017) Ne-Na and Mg-Al cycles are discussed in massive Pop III and low-Z stars as being a result of rotational mixing processes. Our simulations show that convection-induced mixing processes may lead to similar nucleosynthesis. Overall, further investigation is required to properly understand the full nucleosynthetic outcome in such scenarios.

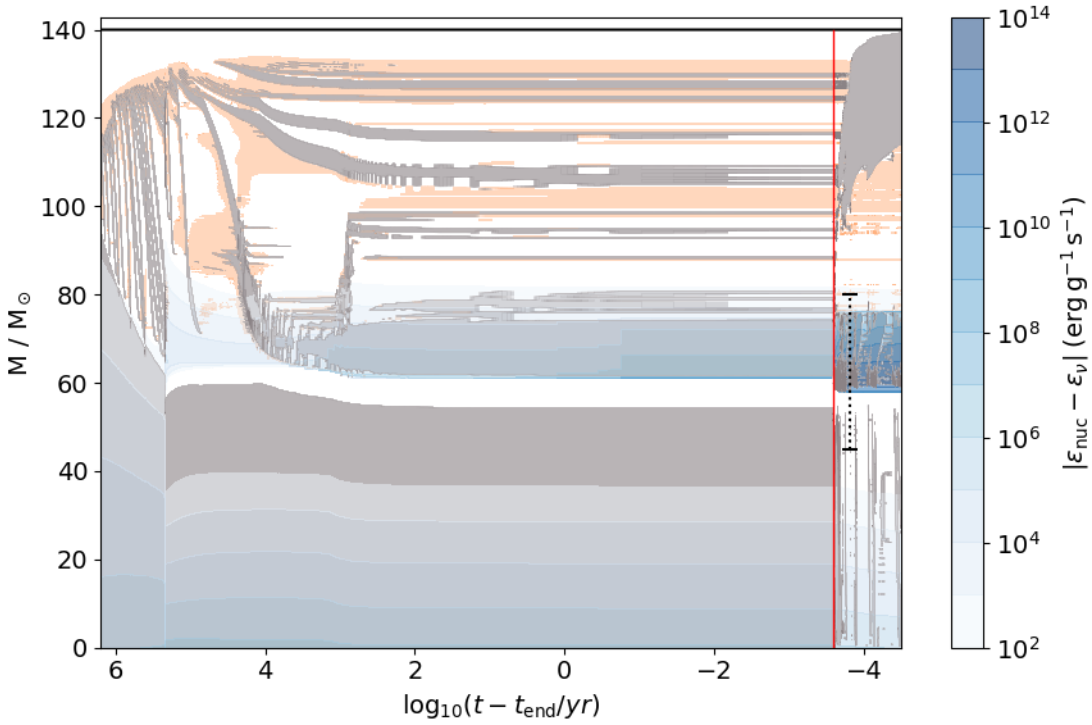

Figure 3.10: Kippenhahn diagram of the 140 $M_\odot$ `Rad-Core` model with the Schwarzschild criterion for convection and $f_{ov} = 0.01$ (`140Mledf-h`) case. Colours are the same as in Fig. 3.2 and peach areas show where semiconvection has been applied. The red line indicates the beginning of the H-He interaction and the black dotted line indicates where the profiles in Fig. 3.9 are taken.

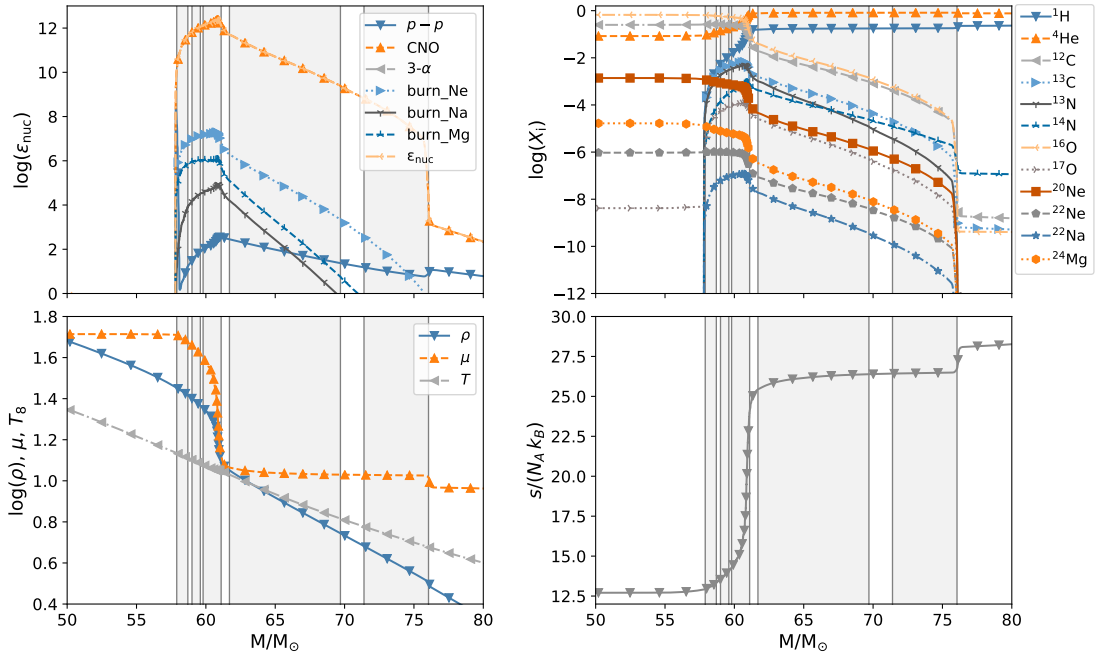

Figure 3.11: Profiles for the `Rad-Core` He interaction `140Mledf-h Rad-Core` case, with the Ledoux criterion for convection, $\alpha_{\rm semi} = 0.5$, and $f_{\rm ov} = 0.01$. **Top left**: Total specific energy generation and that from CNO, p-p and tri-α, Na, Mg and Ne burning reaction groups. **Top right**: Mass fractions of several abundant species. **Bottom left**: Temperature, mean molecular weight and density profiles. **Bottom right**: Specific entropy. Profiles taken 54 min after the H-He interaction begins, times for which are indicated in Fig. 3.10 as black dashed and solid red lines, respectively. Grey areas show regions unstable to convection. See A for profiles of diffusion coefficients.

3.5.4 Convective H Shell and Convective He Core

There is also the case of H-He interactions where the H-rich material enters the convective He-burning core, which comes in second for frequency in 5/26 cases. All of these occur in simulations with $M \geq 60\,{\rm M}_\odot$ using the Schwarzchild criterion for convection including CBM. We describe the `80Mschf-h` case, though all cases displaying interaction between a convective H-burning shell and convective He-burning core begin in a similar fashion. At the beginning core He-burning, the H-burning layer above the core shows little convection, as seen in Fig. 3.12, although it is near the threshold for convective instability. Core He-burning proceeds for 1.5×10^3 yr, the H-shell becomes convective and then within 40 yr, H-burning material enters into the H-free core. In this case, and in others of this class, there is no distinct entropy barrier formed (Fig. 3.13) as the H-rich material enters into the H-free region. Rather, the

existing barrier at the top of the He core is gradually smoothed, with small entropy steps forming in the previously radiative intershell. 10 minutes before the interaction, the He-core has a relevant CBM region of about 0.67 $M_\odot$. In this case, CBM does not play a role in mixing at the base of the H shell as the Lagrangian motion of the H shell is much faster than CBM can effectively mix.

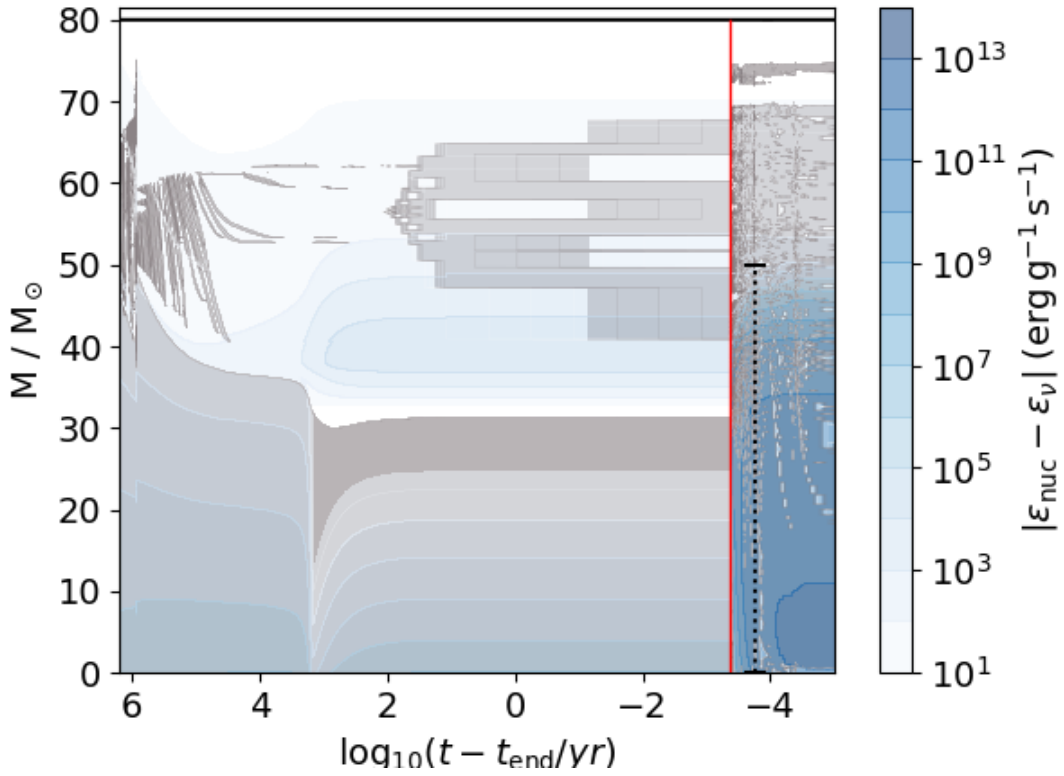

Figure 3.12: Kippenhahn diagram of the 80 $M_\odot$ `Conv-Core` model with the Schwarzschild criterion for convection and $f_{ov} = 0.01$ (`80Mschf-h`). The red line indicates the beginning of the H-He interaction and the black dotted line indicates where the profiles in Fig. 3.13 are taken. Colours are the same as in Fig. 3.2.

All interactions of this type occur at the beginning of core He-burning meaning that there is little C in the core at this point, from $X_{^{12}C} \sim 10^{-6} - 10^{-3}$—levels too low for the i process to play an important role in such interactions. In Table 3.1 it can be seen that the `60Msch-` and `140Msch-f` cases show no change in mass coordinate for the interaction. For these three simulations we do not use $X_H = 10^{-4}$ as the H-free boundary because the H shell and He core merge completely and the value of Δ M/$M_\odot$ = 0 in Table 3.1 would result from our measurement choices. In the

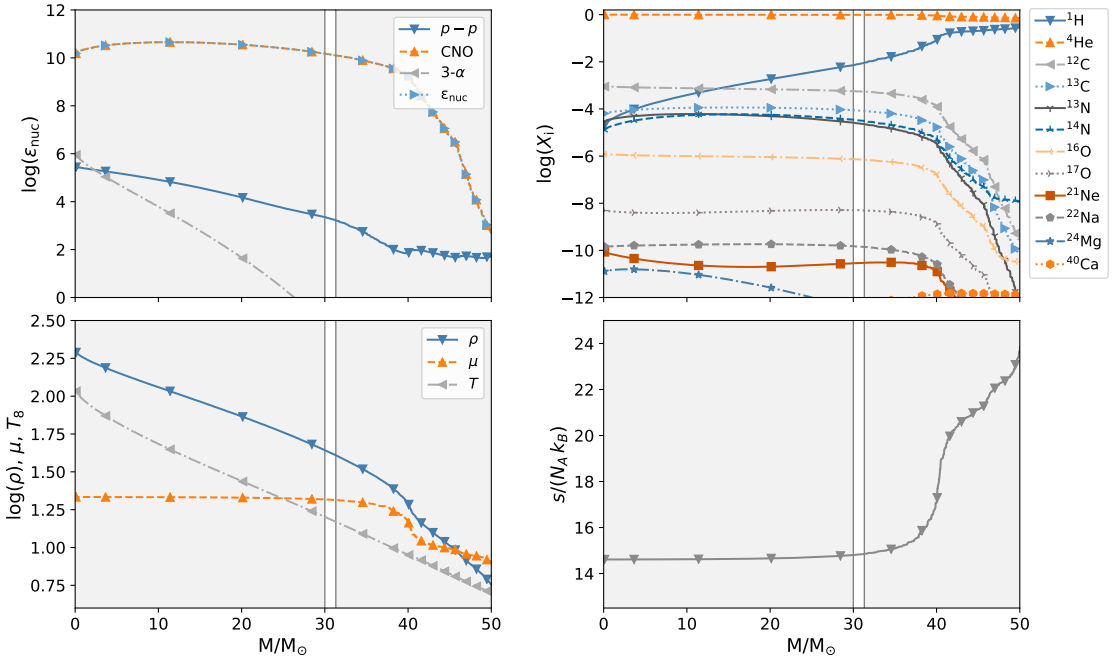

Figure 3.13: Profiles for the `80Mschf-h Conv-Core` case, with the Schwarzschild criterion for convection and $f_{\rm ov} = 0.01$. **Top left**: Total specific energy generation and that from CNO, p-p and tri-α reaction groups. **Top right**: Mass fractions of several abundant species. **Bottom left**: Temperature, mean molecular weight and density profiles. **Bottom right**: Specific entropy. Quantities are shown 1.75 hrs after the H-He interaction begins, the time and mass coordinates for which is indicated in Fig. 3.12 as a dashed black line. Grey areas show regions unstable to convection.See A for profiles of diffusion coefficients.

`60Msch-` and `140Msch-f` models, the H abundance never drops below 10^{-4} in the core. Therefore for these simulations, $X_{\rm H} = 10^{-3}$ was used to compute Δ M/M$_\odot$.

The weak s-process has been reported in the literature to happen in massive stars of both solar and low metallicity as the result of rotational mixing carrying ^{14}N from the H shell into the He core where α captures will transform it to ^{22}Ne thus providing for the ^{22}Ne$(\alpha, n)^{25}$Mg neutron source (Pignatari et al., 2008; Hirschi et al., 2008). This is controlled by relatively slow mixing and burning—quite different from what occurs in our C core interactions. In the `80Mschf-h` case we see no evidence of significant upward mixing of C and O before the mixing event as is reported in Frischknecht et al. (2016). The `80Mschf-h` simulation has a peak neutron density after the interaction of $\log N_{\rm n} \sim 11$. It may be that lower ^{12}C mass fractions can lead to s-process neutron densities with C as a seed as opposed to Fe, but further studies must be conducted to confirm this.

3.5.5 No H-He Interaction

The four simulations that do not undergo any kind of H-He interaction are `15Mled`, `80Mled`, `140Mled` simulations, and the `60Mledf-l` simulations. The first three of these cases have semiconvection with no CBM included, and the `60Mledf-l` simulation has semiconvection plus the lower of our chosen CBM values. Additionally, they all use the Ledoux criterion for convection which includes the stabilizing effect of the gradient in μ. Clearly this is not always sufficient in preventing a H-He interaction, because the `40-` and `60Mled`, and all other than the $60\,M_\odot$ `-led-l` simulations do experience some kind of H-He interaction. These cases are run until the point of Fe-core infall, except for the `140Mled`. As mentioned in Section 3.4.2, the `140Mled` simulation becomes pair unstable. Fig. 3.14 shows an example of the `15Mled` simulation which has no H-He interaction during its evolution.

Zero-metallicity stars of $\sim 140\,M_\odot$ likely end their lives as pair instability supernova (Heger et al., 2003). For the `140Mled` stellar model, all analysis in this work is reported for times before the onset of core O-burning, when the star becomes pair unstable. The adiabatic index, Γ_1 falls below 4/3 in the C-shell leading up to core O-burning, in an off-centre manner with central temperatures rising to over 3×10^9 K. Additionally, the condition that He core masses $\gtrapprox 60\,M_\odot$ should explode as pair instability supernova (Woosley et al., 2002; Langer, 2012, and references therein) agrees with our result as this model has a He core mass of $\approx 64\,M_\odot$. From the onset of the instability (dynamic phase) we do not include subsequent evolution in our analysis. For the `140Mled` model, Table 3.1 only displays H-shell temperatures to the onset of the instability.

3.5.6 C and N Ratios

As described in the preceding subsections, H-He interactions have a variety of effects on the nucleosynthesis that takes place within the H-He region, ranging from moderate to large increase in CNO cycle activity resulting either from downward mixing of protons such that the $^{12}C(p,\gamma)^{13}N$ is triggered effectively, the upward mixing of CNO catalysts boosting the overall CNO activity, or a combination thereof.

In Clarkson et al. (2018) we suggest that with a high H number, it may be possible to eject material from the H-He interaction region prior to the star's death. In this section we use the same assumption as Clarkson et al. (2018) to demonstrate CNO ratios from H-He interactions. Despite the different physical assumptions, our

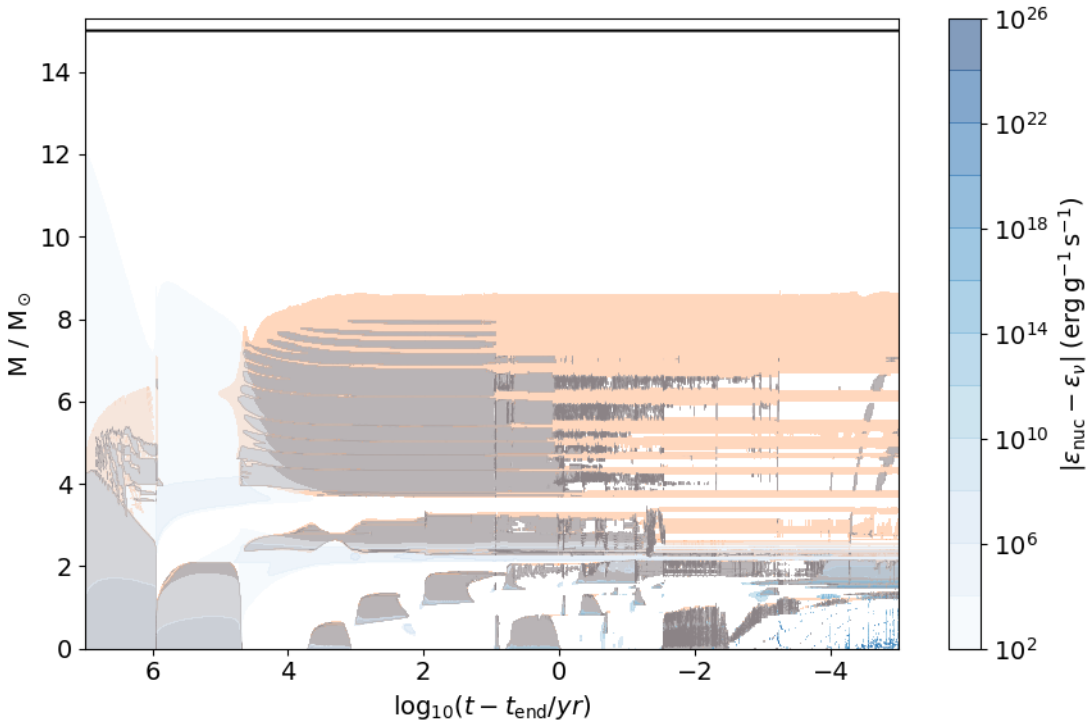

Figure 3.14: Kippenhahn diagram of the 15 $M_\odot$ model with the Ledoux criterion for convection, and semiconvective mixing included (`15Mled`) where no H-He interaction takes place during the evolution. Colours are the same as in Fig. 3.2 and peach areas show where semiconvection has been applied.

integration procedure is the same as one would employ when assuming a faint supernova with no mixing or nucleosynthetic contribution from the shock (c.f., Takahashi et al. (2014); Choplin et al. (2017)). This is the same calculation used in Section 3.4.3, using Equation 3.1. Here, due to the uncertainties in the duration of a H-He interaction, we measure the abundances at different times throughout the interaction, not just at the end of the simulation.

Fig. 3.15 shows the range of $^{12}C/^{13}C$ and [C/N] values in simulations explained in Section 3.5 with the addition of the `60Mledf-l` and `80Mled` simulations. The latter two are shown as examples of the C and N ratios that would result from a faint supernova with no mixing or explosive nucleosynthesis in simulations with no H-He interaction for comparison. We also show the high H number `40Mschf-h` and `80Mledf-h` simulations.

During a H-He interaction, timesteps can vary by many orders of magnitude and each interaction has a unique duration in physical time. Therefore, to sample the C

and N abundances during a H-He interaction, we use a linear spacing in time steps, of 10 points from just before the H-He interaction begins to when there is ~ 5 min of simulation time left, as we do not expect any significant changes in the abundances on timescales smaller. We calculate CNO abundances for two different cutoff assumptions. The green and blue points in Fig. 3.15 are calculated from innermost point where the mass fraction of protons in the H-He layer is 10^{-4}, at the typical region of maximum energy generation. Pink and yellow points have been sampled somewhat deeper, where the proton mass fraction is 10^{-8}. We assume the material taking part in the interaction becomes unbound. The point where the simulations end in this work does not necessarily represent when the event would stop in reality. This is when the 1D calculations are no longer able to continue and suggests the transition to dynamic, 3D behaviour.

Therefore, Fig. 3.15 displays the range of possible C and N ratios during such an event. The `60Mledf-l` and `80Mled` simulations are shown as examples of simulations that do not experience a H-He interaction and we apply the same procedure to calculate abundances but from the end of core He-burning. For the `60Mledf-l` simulation, no point can match the observations because the H envelope material remains in CNO equilibrium. The `80Mled` simulation experiences hot CNO cycling in the final stages of it's evolution and initially has similar CNO equilibrium ratios as many of the other models. Later, the [C/N] ratio increases by almost 2 dex due to partial hot CNO cycling. The $^{12}C/^{13}C$ ratios make H-burning conditions in this model incompatible with the observations as hot CNO burning generally lowers this value. This may be partially alleviated by the inclusion of He-shell material (^{12}C), though a full investigation is beyond the scope of this work. We compare our simulations to observed CEMP-no stars from the literature with measured $^{12}C/^{13}C$ ratios. While well aware of the shortcomings in modelling the time-evolution of H-He interactions in 1D, the CNO ratios shown illustrate that H-He interactions in massive Pop III stars can display a range of values for $^{12}C/^{13}C$ and [C/N], which results in the isotopic and elemental abundance ratios found in stars believed to be the second generation of stars. We do not include any contribution from the interstellar medium because pristine Big Bang abundances would have virtually no effect on C and N isotopic or elemental ratios.

In the bottom left of Fig. 3.15, there is a clustering of points representing the CN equilibrium ratios for conditions within massive Pop III stars. During a H-He interaction, when H-burning material moves deeper into the He layer, the overall [C/N]

ratio rises as the mass coordinate of the H-rich front lowers, as there is simply a much larger mass fraction of C as compared to the H-shell CNO abundances. Similarly, the $^{12}C/^{13}C$ generally increases as the mass coordinate of the H-rich front lower as there is a high ^{12}C abundance in the He shell. Both of these general trends are complicated by the simultaneous mixing and nucleosynthesis taking place and neither evolve monotonically. This is exemplified by the `40Mled` data. A black dotted line is included to Fig. 3.15 to guide the eye. Following blue to green points from the 'early' point at $^{12}C/^{13}C \sim 0.5$ and [C/N] ~ -2.1, ^{12}C increases as the H-burning front moves downward. This leads to large values for both of these ratios. Then, both ratios begin to fall creating a loop-like pattern governed by first the $^{12}C(p,\gamma)$ reaction, leading to a lower $^{12}C/^{13}C$ ratio. This is followed by $^{13}C(p,\gamma)$ which leads to a lower [C/N] ratio. In the future, these ratios may help to constrain the duration, depth and timing of H-He interactions, which as of now, are uncertain parameters.

In some of the cases presented in this work, such as the `40Mled` simulation, protons mix down into the He-rich region where there is a relatively large abundance of C. In this situation, the $^{12}C(p,\gamma)^{13}N$ takes place, ^{13}N is transported downward to higher temperatures where it decays in the presence of α particles. Here CNO cycling does not take place as the timescale for the $^{13}C(\alpha,n)^{16}O$ reaction is many orders of magnitude shorter than that of $^{13}C(p,\gamma)$, where there are very few protons at the bottom of the He-shell. In other cases presented here, the variety in CN ratios relates to the mixing of protons with large amounts of ^{12}C and ^{16}O, which boosts CNO activity. In many of our simulations, the CN ratios are never able to return to equilibrium values and the points in Fig. 3.15 show how this mixing and burning can evolve in time.

3.6 Discussion

The structural properties of Pop III stars seem to lend themselves to H-He interactions. The cause of H-He interactions has been associated with relatively small temperature gradients (Limongi & Chieffi, 2012) and entropy differences (Heger & Woosley, 2010) between H and He layers in Pop III stars. Shallow temperature gradients are the result of the higher temperatures found in H-burning. All other state variables constant, a higher H-burning temperature would lead to a higher entropy in the H-burning shell, yet the smaller gradient in temperature leads to a less stiff boundary. The latter is also the case for the shallow density gradients found between

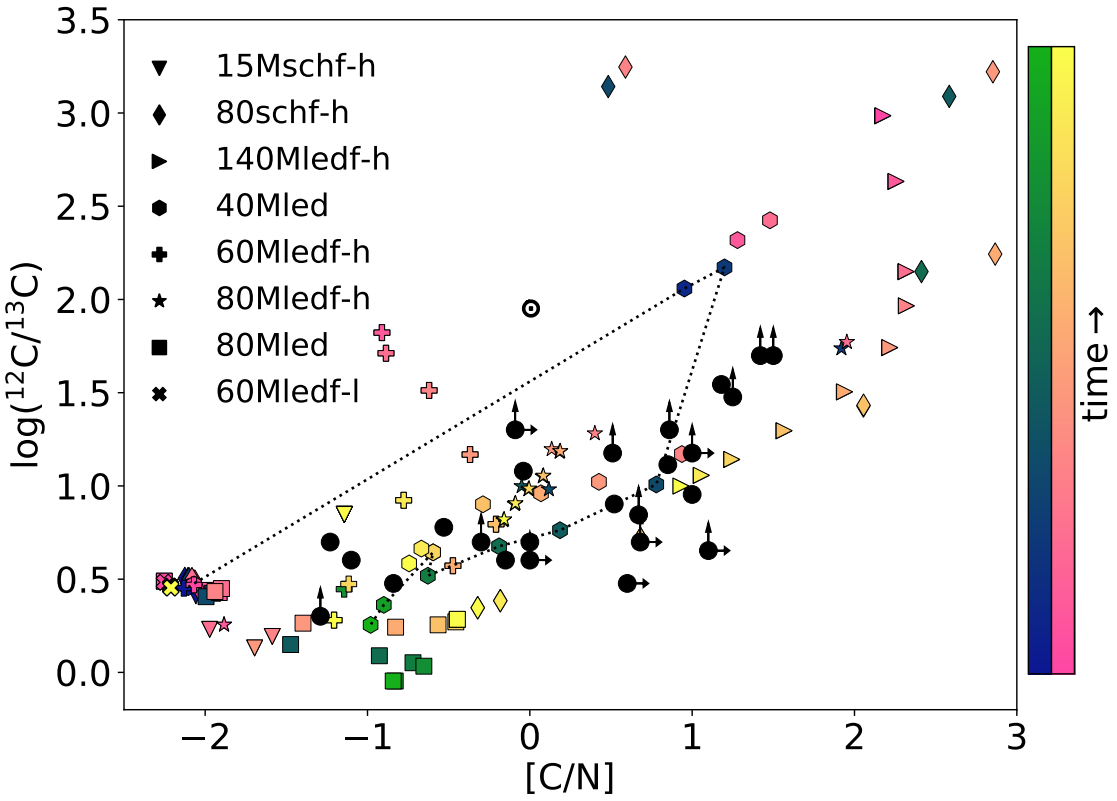

Figure 3.15: C isotopic and CN elemental ratios from observed CEMP-no stars are shown in black. Data are taken from Beers et al. 2007, Plez & Cohen 2005,Norris et al. 2013, Norris et al. 2010, Yong et al. 2013, Roederer et al. 2014, Hansen et al. 2015 and Masseron et al. 2010. Blue and green symbols show ratios in the H-He region or H-shell for models which do not experience a H-He interaction. Pink and yellow symbols sample abundances deeper within the region. The choice of data points is described in the text of Section 3.5.6 and the calculation for each abundance is given in Equation 3.1. The black dotted illustrates one of two paths taken by the `40Mled` case. Simulation data point colours change as an indication of time with pink and blue being earlier in a H-He interaction and yellow and green being later. Note that in some simulations, points at the same time for different depths can largely overlap. The solar ratios are indicated by the $\odot$ symbol.

H and He layers in Pop III stars. The overall smaller entropy differences between the two layers are primarily due to the higher densities in the H envelope, which are orders of magnitude higher than in post-MS solar metallicity massive stars. Pop III stars also have a much lower envelope opacity than solar metallicity stars. All of this is the result of an initial zero metallicity which results in a hotter, more compact star.

Choplin et al. (2017) explore the nucleosynthesis which may occur in massive stars of metallicity $Z = 10^{-5}$. The authors highlight production of H-burning material in the form of CNO and elements with $Z = 10^{-13}$ amplified by the upward mixing of ^{12}C and other isotopes from the He shell into the H-burning shell due to rotational mixing. For some models, an ad hoc enhanced shear diffusion coefficient is used in order to initiate H-He interactions at specific times. They then relate [C/N] and $^{12}C/^{13}C$ to observations. In general concurrence with our results presented in Section 3.5.6, they found that H-He interactions occurring in massive Pop III stellar models reproduce the CN ratios found in CEMP-no stars.

Choplin et al. (2017) suggest that the final $^{12}C/^{13}C$ ratio depends on their selected timing of the mixing event relative to the end of the stars life. This is true if one were to assume that the star does not eject material with these signatures prior to Fe-core infall, thus terminating the CNO cycle. In addition, we also find that the downward mixing of protons into the He-shell also terminates the CNO cycle by cutting off the supply of protons. Both of these effects lead to a variety of CN ratios in our simulations. Additionally, it appears that secular mixing process such as rotation (Choplin et al., 2017; Maeder & Meynet, 2015), or semiconvection (this work) cannot simultaneously reproduce many of $^{12}C/^{13}C$ and [C/N] ratios observed in CEMP-no stars.

H-He interactions are less likely in stars of increasing metallicity than in their zero-metallicity counterparts and due to both the differences in structure such as a higher opacity and entropy barrier between the H and He shells, and H-burning nucleosynthesis. Despite this, they have been reported in simulations at low-Z and have been reported in super-AGB stars by Jones et al. (2016) and massive stars by Ritter et al. (2018).

H-He interactions occur *not infrequently* in simulations of massive Pop III stars by Limongi & Chieffi (2012). This is confirmed by our findings for any given set of parameters. They also note that differences have been found in results for H-He interactions from various authors but do not specify what they are. While we cannot know at this time how much of these differences are due to different physics or implementations of stellar physics and numerical methods, our results show that there are multiple modes of H-He interactions, and more than one kind can be present using the same code and macro-physics assumptions. In an attempt to explain the CEMP-no star HE 0107-5240 the same authors report that H-He interactions lead to C, N, and Na relative to Mg in ratios consistent with the mixing of protons into

He shell (Limongi et al., 2003)—although the nucleosynthetic process responsible was not described.

Banerjee et al. (2018) present yields of i-process nucleosynthesis from parametrised post-processing calculations using $20 - 30\,M_\odot$ stellar evolution models. They focus on what in this work we call `Conv-Shell` interactions—where H is *ingested* into a convective He shell below. They only consider stars of $> 20\,M_\odot$ because, as they state, those less massive will not undergo any ingestion because He shells in these stars never expand to the base of the H-rich layers. They also state that at masses $> 30\,M_\odot$ proton ingestion events will not happen because H has already been depleted in the shell. We have found that other types of H-He interactions can occur without a convective He shell, but a convective He region allows for the i process to occur. In our `140Mledf-h` and `40Mschf-h` simulations, shown in Figs. 3.6 and 3.10, where H-rich material corrosively burns and descends into a radiative He core and -shell, respectively, the material is able to descend far enough into the He shell by the end of the simulation that protons and ^{12}C mix at mass fractions of $\sim 10^{-2}$ and ≈ 0.3, respectively. This can lead to high H numbers although our simulations do not indicate that the i process can take place in such scenarios.

In Banerjee et al. (2018) all shell interactions were initiated by hand using ad-hoc diffusion during nucleosynthesis post-processing. As the authors state, this is done as they wanted to avoid a splitting of the convection zone. In 1D simulations the i process may be prevented or suppressed by the formation of an entropy barrier (Clarkson et al., 2018; Herwig et al., 2011). At this time it is not clear how such a barrier would evolve in 3D. Additionally, the stellar evolution simulations in Banerjee et al. (2018) were post-processed and do not include the effects of the energy generation due to the H-He interaction on the 1D model, which is orders of magnitude greater than in quiescent H-shell burning. This 1D prediction has been shown in the present work, and in Clarkson et al. (2018) for a similar scenario where luminosities can reach $\log(L/L_\odot) \sim 13$. Inspection of the Kippenhahn diagrams shown in Figs. 3.7 and 3.8 of the `40M-led` simulation, shows that the energy generation from nuclear reactions has a significant effect on the structure of the star for the remainder of the simulation.

Mixing of H-rich material into He cores and shells has been reported by Yoon et al. (2012) for both rotating and non-rotating stellar models of $20 - 500\,M_\odot$. As in the work presented here, calculations are terminated for H-He shell interactions shortly after the onset. They found that models with shell interaction can produce

up to 1000x more ^{14}N in the H shell as compared to models that do not have a shell interaction due to upward mixing of CNO catalyst but still less than those with chemically homogeneous evolution as a result of rotation. They do not describe the nucleosynthesis in the He shell as they did not have mixing and burning equations coupled, and in convective-reactive scenarios, Da goes to unity. Furthermore, they observe convective H shells in several models that extend downward and interact with the He-burning core. They describe two modes of interaction for H-He core interactions—both of which begin with a descending envelope as we have described in Sec. 3.5.4 and Sec 3.5.3. The difference in the two relates to the primary direction of material during the interaction. In some models, once the H shell descends, material moves downward into the He core and in others, material moves primarily upwards into the H shell boosting the CNO cycle as core convection has turned off. These reports appear very similar to our `Rad-Core` and `Conv-Core` simulations.

Hirschi (2007) found that in simulations of very low metallicity rotating massive stars, primairy N production was enhanced by H-He interactions leading to the upward mixing of CNO catalyst from the He-burning core into the H shell. This enhanced N production was found to better reproduce the observations of CNO abundance ratios evolution in metal-poor halo stars (Chiappini et al., 2006). Pignatari et al. (2015) argued that H-He interactions followed by SN explosions at low metallicity should be at least partly responsible for the solar ^{14}N/^{15}N value and may play a greater role at low-Z. We have found that a boost in CNO can occur during the H-He interactions presented in this work, for example in the `15Mschf` and `140Mledf` models. Total yields are dependent on the final fate of the star but using the same assumptions made in 3.5.6 we can derive an estimate of the N yield. For the `15Mschf` model, at the final timestep the total integrated N yield is $4 \times 10^{-7}\,\mathrm{M}_{\odot}$. For both the `40Mled` and `140Mledf` models we find a total N yield of $\approx 0.04\,\mathrm{M}_{\odot}$. The `80Mschf` model gives $2.5 \times 10^{-4}\,\mathrm{M}_{\odot}$. This value can be compared with the `80Mled` model presented in 3.4.3, which does not encounter a H-He interaction. The `80Mled` model has a much lower final N yield of $6.7 \times 10^{-7}\,\mathrm{M}_{\odot}$. Two major caveats are worth noting for our estimations. First, it should be noted that we do not calculate beyond the H-He interaction and it is currently unclear what the long-term evolution of such models would be. If the simulations were to evolve longer, this may increase N production in some models by allowing CNO time to equilibrate. Second, we assume the complete ejection of the envelope, although if a GOSH or similar instability were to occur in some cases without a supernova explosion, it may be that only a fraction

of this material is ejected. In this case, our estimates represent upper limits. Given the uncertainties in the final fates of these stars, these numbers should be taken as illustrative estimates as opposed to definitive predictions.

The results from 1D stellar evolution during events of this nature violate the assumptions of MLT (Jones et al., 2016). One of the issues is the fact that the timescale for mixing and burning becomes comparable and at the same time, large amounts of energy are released that can modify the convective morphology of the layer. At this point the details of how these interactions will evolve are unclear and modelling assumptions must be made. For the case of low-metallicity, low-mass stars Cristallo et al. (2009) do not alter the result of stellar evolution simulations predicting a split in the convection zone forms. Banerjee et al. (2018) for the case of massive low or zero metallicity assume in the post-processing of H ingestion into the He-shell convection zone a continuous mixing and burning without feedback into the stellar structure. Herwig et al. (2011) also allowed mixing to continue past the time where the split of the convection zone would have occurred, guided by elemental abundance observations of the post-AGB star Sakurai's object.

Using 3D hydrodynamical simulations, Herwig et al. (2014) found that the ingestion and burning of H into the He-shell convection zone lead early-on to the formation of an entropy shelf in spherically-averaged profiles in the upper half of the He-rich convection zone. 3D hydrodynamical simulations of a low-Z AGB star by Stancliffe et al. (2011) do not find a split in the convection zone, although they caution this could be because their simulations were not evolved beyond 4 hr star time. It is not clear currently what the long term evolution of a H-He interaction is and how they may compare in different stellar environments. Despite this, 3D simulations suggest that some aspects of these events are recovered in 1D simulations, such as the location of H-burning and high energy generation which leads to Da ~ 1 (Herwig et al., 2014). In 3D hydrodynamic simulations, this combustion leads to a dynamic, non-spherically symmetric response within the star, which would violate assumptions of MLT, and at least temporarily, hydrostatic equilibrium. To properly understand if and how these events unfold and answer questions about e.g. how the entropy barrier evolves in time for massive Pop III stars, these events must be simulated in 3D.

3.7 Conclusion

We have investigated the occurrence, variation and types of H-He interactions in massive Pop III stars with a variety of masses and mixing assumptions. This study demonstrates that using several reasonable assumptions regarding macrophysical mixing processes, the unique structural properties of Pop III stars, which result from their initial composition, lend themselves to H-He interactions in 1D stellar evolution models. We have found that there are four distinct modes of interaction depending on the evolutionary stage and whether or not protons mix with convective He-burning material. Only loose trends can be found with respect to either mass or mixing prescription. For example, interactions involving radiative He layers occur only when using CBM and core interactions become more frequent over $40\,M_{\odot}$. H-He interactions correlate with contractions at the onset of, or during core He burning, at the beginning of core C burning or at the beginning of core O burning.

Energy production in these events depends primarily on the amounts of ^{12}C and protons in the He and H shell respectively and is dominated by CNO reactions in all simulations. In `Rad-Shell` and `Conv-Core` simulations, the H number tends to be lower. Later in core He burning, `Rad-Core` interactions can take place which are generally more energetic as higher amounts of C and O mix into the previously radiative intershell region above the core. This mixing can also bring Ne and Mg from the core triggering Ne-Na and Mg-Al cycles, which to our knowledge, has only been reported in works including rotation. Lastly, `Conv-Shell` interactions, which have been identified as a possible i-process site, are typically highly energetic, resulting from more advanced convective He-shell burning.

We have also found that as a H-He interaction unfolds, ^{12}C/^{13}C and [C/N] ratios can take a wide range of values owing to both downward mixing of protons and upward mixing of He-ashes. We have shown that the ^{12}C/^{13}C and [C/N] ratios found in our simulations are consistent with observed CEMP-no stars, stars believed to carry the chemical signatures of the first stars.

We have explored multiple frequently-used mixing prescriptions to better understand the parameter space in which these events occur and how they occur. As such, the frequency or behaviour of H-He interactions presented in this work should not be considered as representative of the frequency or behaviour in the first stars. Given the 3D hydrodynamic nature of these events is not yet well understood, this work should serve as a roadmap for future 3D hydrodynamic simulations to investigate

H-He interactions which may have taken place in the first generation of stars.

Acknowledgements

We would like to thank Raphael Hirschi for his helpful comments while refereeing this work. OC would like to thank Pavel Denissenkov, Sam Jones, and Etienne Kaiser for comments on drafts of this work and Michael Wiescher for valuable input on nuclear physics aspects. FH acknowledges funding through an NSERC Discovery Grant. Simulations were carried out on the Compute Canada Arbutus cloud computer as part of a computing resource allocation to Falk Herwig. This work benefited from support by the National Science Foundation under Grant No. PHY-1430152 (JINA Center for the Evolution of the Elements). This work was made possible by the open source `MESA` stellar evolution code.

Data Availability

The data underlying this article will be shared on reasonable request to the corresponding author.

Chapter 4

3D Hydrodynamic Setups and Simulations

Attributions for hydro simulations: The `PPMStar` code was written by Paul Woodward at the University of Minnesota. Simulations presented in this section were run by myself, and others were run by Falk Herwig and Paul Woodward and myself. Setup scripts discussed were created by myself with guidance from and minor modifications made by Falk Herwig. All `PPMStar` code modifications were done by Huaqing Mao and Paul Woodward at the University of Minnesota except minor modifications to include two convective burning shells were made to the `PPMStar` code by myself under the guidance of Robert Andrassy. The idea of using three fluids for the problem below described was conceived of by Paul Woodward and Falk Herwig.

4.1 Abstract

In this chapter I describe the problem of modelling the evolution of H and He shells in massive Pop III stars using the `PPMStar` 3D hydrodynamics code. Two setup scripts are presented and the general results and challenges found in simulations are presented.

4.2 Introduction

As stated in Chapters 2 and 3 interactions between H and He shells can create a convective-reactive environment. Such an environment occurs when the mixing timescale is similar to the relevant nuclear timescale. Modern stellar evolution codes such as `MESA` have the mixing and nuclear processes coupled in order to better resolve these and similar types of events. Nevertheless, mixing length theory (MLT) is a local, time-independent theory that typically assumes the star is in hydrostatic equilibrium (see Eq. (1.1)), and that mixing happens over some characteristic length scale, l_m, which is usually on the order of a pressure-scale height, H_p. Furthermore, in 1D stellar evolution codes, mixing of chemical species is done via a diffusion equation, which in `MESA` includes a diffusion coefficient estimated based on the previous time step's value, rather than recalculating for every iteration, which over time can potentially lead to errors in the mixing, especially when rapid changes occur. H-He interactions drive rapid changes, which is already problematic due to the fact that MLT use averages over space and time. Additionally, in 1D models it is nearly always assumed there is symmetry in the up and down flows within a convection zone.

3D hydrodynamics codes will generally avoid all of these shortcomings and provide the ability to evolve a 3D flow in the convective-reactive regime, including the boundary and it's associated mixing. In this, we have natural perturbations and instabilities due to convection, without using models including free parameters to treat convection and boundary mixing. In order to model a star in 3D, one must select an initial state and configuration. Typically what is done is one maps a 1D model to a 3D grid. When mapping 1D stellar evolution simulations to a 3D Cartesian code, one must make decisions on how to map the quantities of interest cell-by-cell. If deviations do occur, how much is acceptable? How do you map one boundary condition to another? What other kinds of assumptions need to be made in your model based on code constraints? There is also the conundrum resulting from the fact that you

are using a model based on MLT and all its associated assumptions to construct a model that is meant to be free of those assumptions. What impact does that really have? While this mapping poses unique challenges, little has been written on the topic. Chen et al. (2013) focused on conservation of physical quantities, such mas mass and energy, in constructing 3D models primarily for supernova explosion simulations. Zingale et al. (2002) discuss methods to maintain hydrostatic equilibrium when mapping from 1D to 3D codes, particularly in the case that discretization is not the same (e.g., cell-face quantities vs cell-averaged). They also point out that poorly chosen boundary conditions, not matching those of the 1D model, can lead to spurious velocities, along with inadequate resolution and source terms resulting from initialization method.

The `PPMStar` code has been used for stellar evolution simulations for over a decade and has evolved simulations of Post-AGB stars Herwig et al. (2011, 2014); Woodward et al. (2015), rapidly accreting white dwarfs Denissenkov et al. (2019), C-O shell mergers Andrassy et al. (2020), oxygen-burning shells Jones et al. (2017) and main sequence H-burning cores in massive stars (Herwig et al., 2020, in prep.). Beyond what is described in Chapter 1.2, the `PPMStar` code uses a two-fluid scheme to model boundary mixing. For both fluids, 10 higher-order moments are used to compute the fractional volume within each cell at each time step (Woodward et al., 2015). This allows one to track each fluid with greater detail than they would be in standard PPM schemes. In all previous `PPMStar` simulations mentioned, only a single convection zone has been modelled. For the Pop III H-He interaction case, both convection zones should be simulated if we want to properly understand the mixing. Another critical ingredient in properly understanding the evolution of H-He shell interactions is the equation of state (EOS). For massive stars, including those of Pop III, radiation pressure is a non-negligible effect. In the He shell of a massive Pop III star, the total pressure can often be more than 50% due to radiation. In most of the published `PPMStar` simulations, an ideal gas EOS is used as radiation plays a much smaller role in low mass stars. This will lead to changes in the mixing behaviour we are interested in and makes modelling nucleosynthesis less straightforward. These challenges and others will be described in the following sections.

Here I present the two scripts codes I created to map 1D stellar evolution models to the 3D `PPMStar` code. One has now been used for a multitude of simulations. The other is for future multi-fluid simulations. I also describe the simulations which have been run with an earlier mapping script and the first of he recent scripts and the

challenges presented, with their solutions or possible solutions if not yet implemented. The simulations presented here are, to my knowledge, the first full 4π double-shell stellar convection simulations.

4.3 Passive Double Shell Simulations

Robert Andrassy and I created two setups[1]. The first was for H-core burning in a $25\,M_\odot$ solar metallicity star, and the other for the $45\,M_\odot$ Pop III stellar model presented in 2. Only the latter will be discussed here. Using the $45\,M_\odot$ model we extracted the temperature, density and mean molecular weight in the region of interest using profiles and constructed a setup using a script written by Falk Herwig. This setup script used state variables at the base of a single convection zone along with the mean molecular weight of each fluid, μ, to integrate an initial model assuming an ideal gas in hydrostatic equilibrium. These simulations are an example of a convective H shell interacting with a convective He shell discussed in 3.5.2.

For these simulations, I made minor modifications to the `PPMStar` code to create two burning shells. When running simulations in the `PPMstar` code, the user can either drive convection using a constant heating applied to the base of the convection zone or use the burn module, which allows users to add nuclear reactions based on a two fluid setup. At the base of the He shell we added heating to drive convection, which is typically done, and at the top of the H shell, we included a cooling term, which was conceived of by Falk Herwig. The main reason for this choice was that heating (or cooling) is added at a fixed grid location (doesn't expand with the fluid) and could lead to severe inaccuracies if the boundary moves through the course of the simulation. Such a passive simulation, not including any nuclear reactions is shown in Fig. 4.1. This image is taken at around 2 days simulation time.

The versions of the `PPMStar` used in this chapter track two fluids to high precision. In constructing these models, and within the code, a series of equations are applied, which conserve mass and species. They are as follows:

$$FV = FV_1 + FV_2 = 1; \text{where } FV_i = V_i/V \tag{4.1}$$

$$V = V_1 + V_2 \tag{4.2}$$

[1]Throughout this section, setup means the result of mapping from 1D to 3D

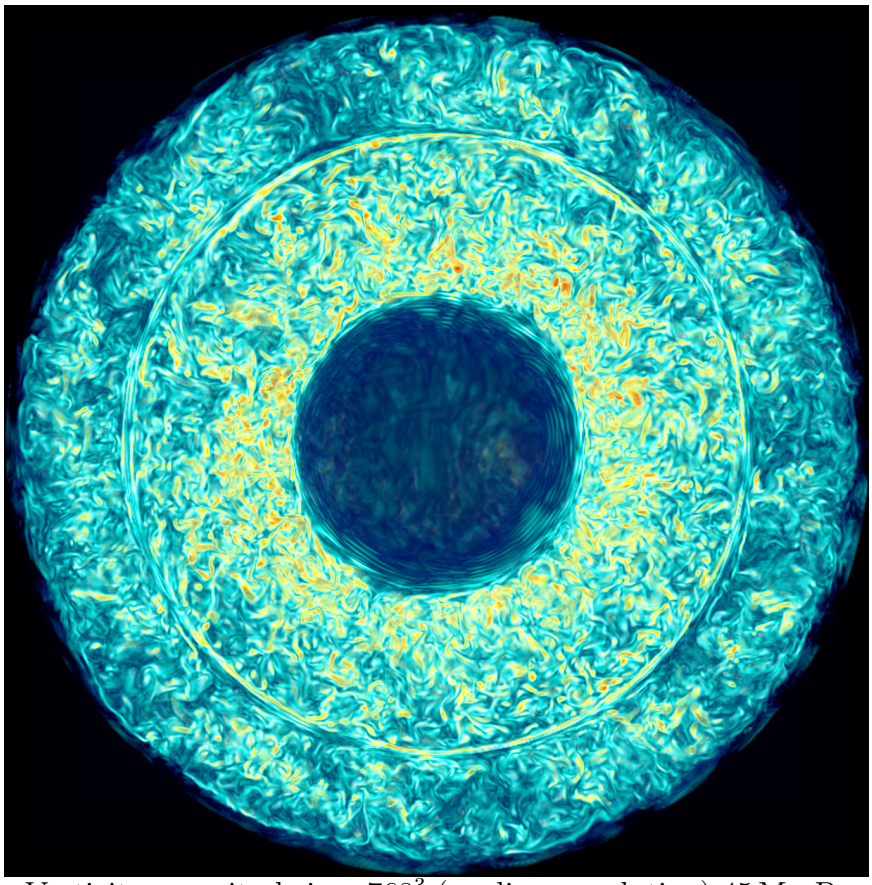

Figure 4.1: Vorticity magnitude in a 768^3 (medium resolution) $45\,\mathrm{M}_\odot$ Pop III passive burning simulation.

$$m = m_1 + m_2 \tag{4.3}$$

$$\rho_i = \frac{m_i}{V_i} \tag{4.4}$$

$$\rho = \frac{m}{V} \tag{4.5}$$

$$X_i = \frac{m_i}{m} = \frac{\rho_i F V_i}{\rho} \tag{4.6}$$

$$\mu_i = \frac{\rho_i}{\rho_j}\mu_j \tag{4.7}$$

In Eq. (4.1) FV is the fractional volume. This is the quantity the code explicitly

tracks in advecting each fluid. All other quantities have their typical meaning. Typically in astronomy mass fractions, X_i, represent isotopes such that $\sum_i X_i = 1$. Here, X_i is the mass fraction of all species in fluid i, so for each fluid $X_i = \sum_j x_j$, where x_j is each individual isotope and $X_1 + X_2 = 1$. These individual isotopes are not explicitly tracked in the code but are important for calculating the mean molecular weight.

Falk Herwig created a burn module for the `PPMStar` code that recovers the most important nuclear reaction in the case of the born again scenarios in post-AGB stars, the $^{12}\mathrm{C}(p,\gamma)^{13}\mathrm{N}$ reaction. This module utilizes the fact that He-rich material is where almost all C will be and H-rich material, of course, is where H is. The module is given the amount of C and H in each fluid and burns the fluids contemporaneously with the hydrodynamics step, depositing the associated energy into the flow. This is also to around first-order the most important reaction in the case of H-He interactions in Pop III stars. When using the ideal gas setup and the fluid you are simulating is not strictly an ideal gas, deviations in state variables are bound to occur. In the case of Pop III H-He interactions, this is important when you want to model a T-dependant nuclear reaction, such as $^{12}\mathrm{C}(p,\gamma)^{13}\mathrm{N}$. Fig. 4.3 shows the correction to the temperature as seen by the burn module. This is done in order to compensate both for the equation of state used, and the high concentrations of H and C in the boundary region are a result of using only two fluids in the simulation, which is shown in Fig. 4.4. These higher than desired concentrations come from the fact that Eq. (4.1) dictates that the sum of the mass fraction must be unity and one also must properly model the mean molecular weight, which is important for convective mixing. Therefore, it is impossible that the fluids not meet at high ratios somewhere.

Fig. 4.2 is an example of a simulation run with the above setup style. For this simulation I also included energy generation from the $^{12}\mathrm{C}(p,\gamma)^{13}\mathrm{N}$ reaction. In the top panel, one can observe the vigorous burning in the He shell. In the bottom panel, the He-shell material begins to pierce through into the H shell. This simulation should only be viewed as an indication of what may happen during a H-He interaction as the equation of state used in this simulation has been approximated as an ideal gas, which is addressed in 4.4.1 and the two-fluid assumption leads to an overestimation of the energy generation, which is described and addressed with possible solutions in 4.4.3.

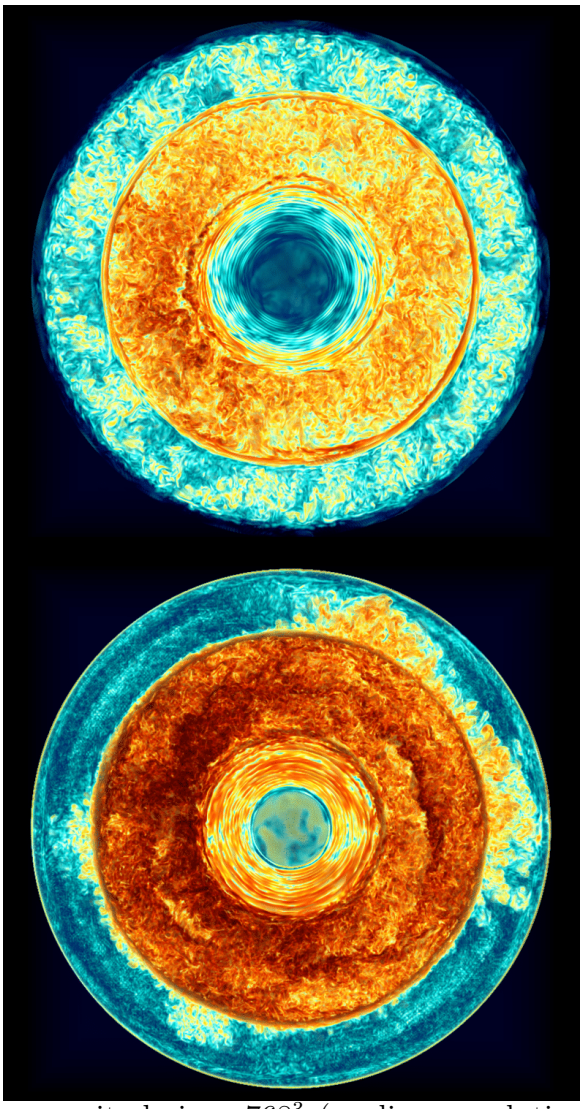

Figure 4.2: Vorticity magnitude in a 768^3 (medium resolution) $45\,M_\odot$ Pop III test simulation of a He and partial H shell at $t = 3.44$ (top) and 4.34 (bottom) days, simulation time.

4.4 Setups

4.4.1 GASRAD EOS

In order to better model H-He interactions with a convective He shell, the correct equation of state is necessary. This physical consideration was implemented into the `PPMStar` code by PhD student Huaqing Mao at the University of Minnesota. Instead of taking profiles directly from `MESA` as initial conditions for hydro simulations, which

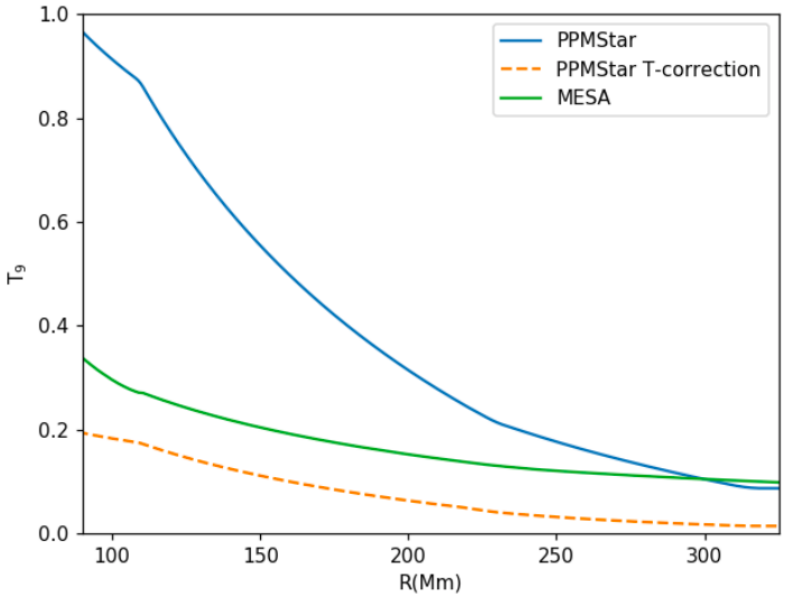

Figure 4.3: Temperature correction for L28 simulation compared to original setup and `MESA` profile. The green line shows the T profile in the original `MESA` simulation. The blue line is the `PPMStar` T profile using an ideal gas equation of state and the orange line is the corrected profile.

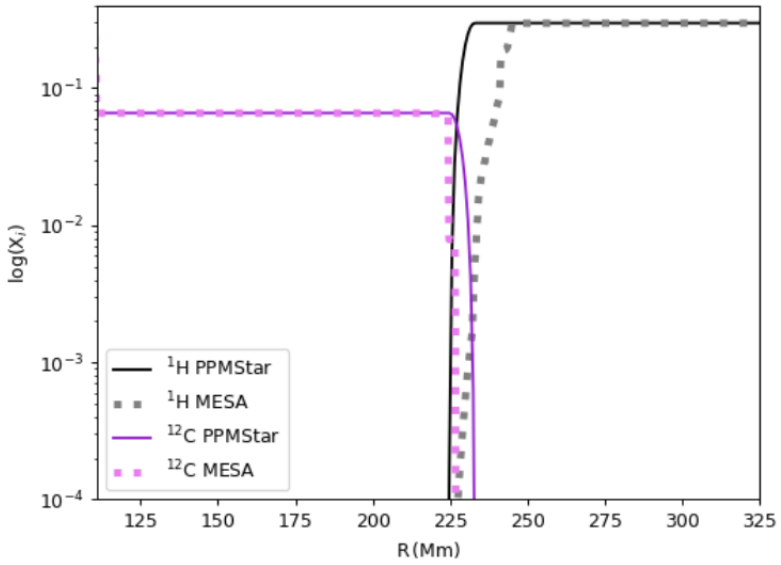

Figure 4.4: Example of mass fractions from two fluid hydro setup compared to MESA profiles.

can often include various artifacts, I produced a script to read in data from `MESA` and create self-consistent initial conditions, adopting the correct equation of state.

Appendix B shows the code and output from it.

The steps contained within the setup script are described in Fig. 4.5. The left column shows steps used in all scripts and the right column shows additional steps for multifluid simulations. The final portion of this script was the prototype for the setup of the initial stratification used in `PPMStar`. The equations used are as follows:

$$S = S_{\rm gas} + S_{\rm rad} = c_{\rm v} \log T - \frac{\mathcal{R}}{\mu} \log(\rho) + \frac{4}{3} \frac{aT^3}{\rho} \tag{4.8}$$

$$P = P_{\rm gas} + P_{\rm rad} = \frac{\mathcal{R}}{\mu} \rho T + \frac{1}{3} a T^4 \tag{4.9}$$

Eq. (4.8) is the entropy of a mixture of an ideal gas and radiation and Eq. (4.9) is the pressure for the same mixture. All variables have their typical meaning and $\mathcal{R}$ is the gas constant and μ is the mean molecular weight.

Below, Eq. (1.1) and Eq. (1.2) are repeated here in Eulerian coordinates for reference:

$$\frac{\partial P}{\partial r} = -\frac{Gm(r)\rho}{4\pi r^2} \tag{4.10}$$

$$\frac{\partial m}{\partial r} = 4\pi r^2 \rho(r) \tag{4.11}$$

The above equations are a system of four non-linear equations, one of which contains transcendental functions. We use the values we have chosen of S and μ along with r, based on the 1D model to describe the stratification as we are interested in boundary mixing, although in principle any two variables in these equations could be used in their place. We also store lower boundary values of P and m. To solve this system of equations, the initial conditions are passed into a solver for Eq. (4.11) and Eq. (4.10), which uses the Runge-Kutta method. The Runge-Kutta method is a fourth-order explicit method. An ideal gas EOS is used to determine initial 'guess' values of ρ and T at the base of the He shell, which are refined by calling a Newton-Rhapson method. The updated values are used to solve the full system of equations. In `PPMStar` the values produced by the Runge-Kutta step are interpolated onto the simulation grid. The logical flow of this code is shown in Fig. 4.6.

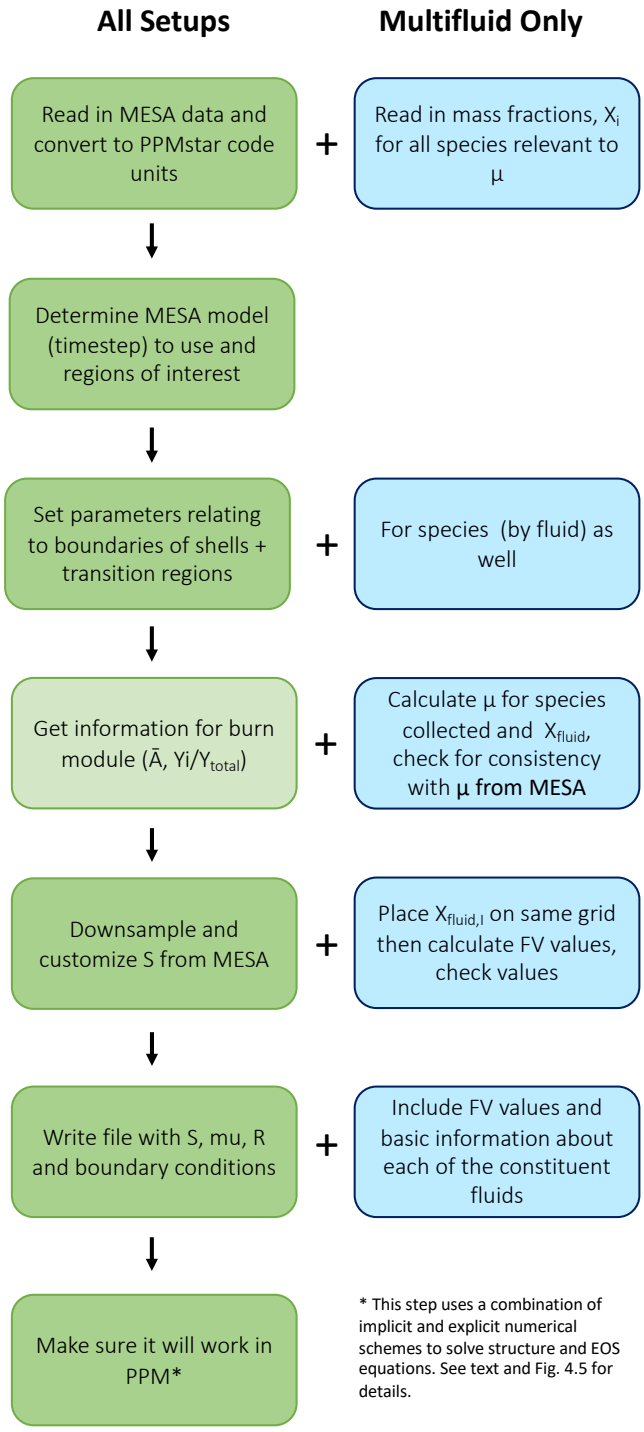

Figure 4.5: Flow chart describing hydro setup scripts.

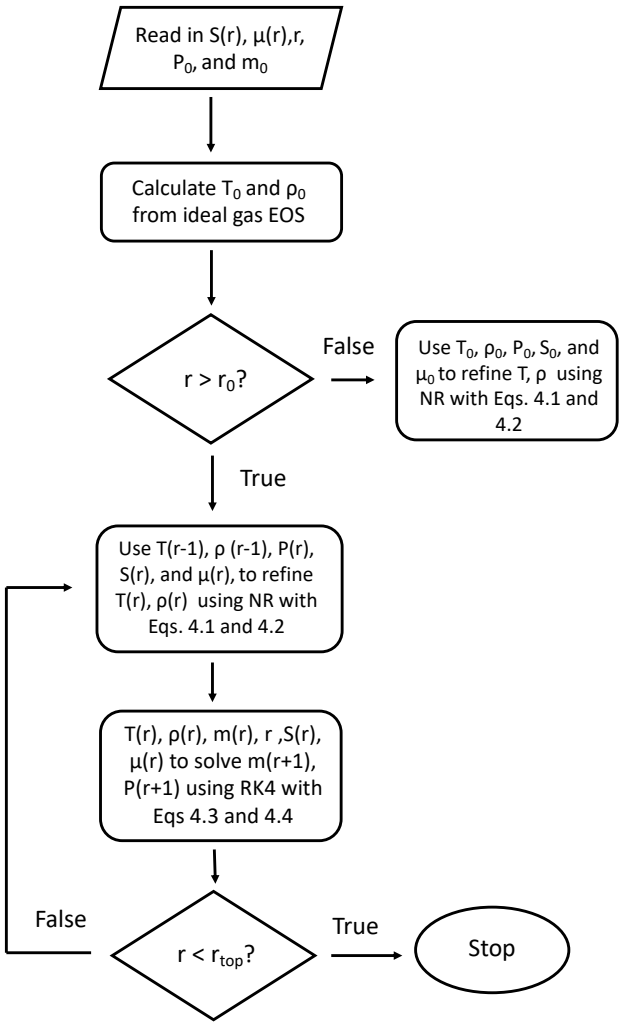

Figure 4.6: Flow chart showing prototype of final step in setup scripts. This was created as a prototype for `PPMStar` to initialize the setup based on the setup file produced.

The customization step in Fig. 4.6 (5th step) glosses over a complicated, almost philosophical topic. In this step one must make physical modelling choices for which there is no first-principles solution. The conundrum is that you are using a 1D stellar evolution simulation which is known to not treat convection accurately. This model includes results which may or may not be realistic. A good example of this is shown in Fig. 4.7, where `MESA` returns a small bump in the entropy profile due to mixing of species downward from the H shell. In this example, I have decided that I do not want that influencing my simulation. Any choice made will impact the 3D hydrodynamics

simulation. It is also worth noting that small lumps and bumps in physical quantities and/or state variables may not be resolved on the 3D grid. For example, on a 756^3 grid, the spatial resolution for a Pop III H-He shell setup is $\sim 1\,\mathrm{Mm}$, any structure within a factor of a few of this will either be nearly smoothed away by interpolation, or, if near the boundary of the two convection zones, completely smoothed over by another routine where boundaries behave as a prescribed function that enforces a smooth and continuous transition.

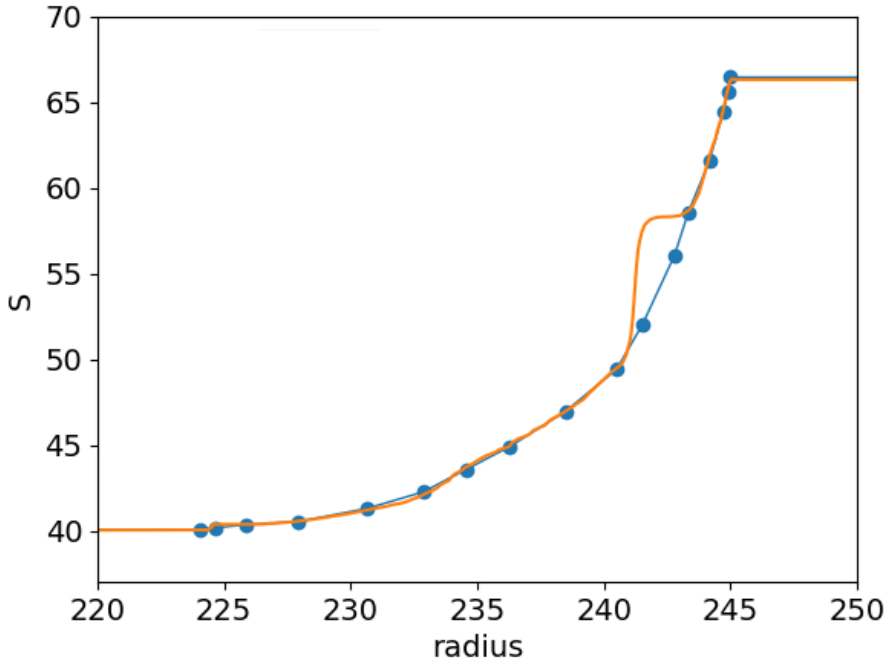

Figure 4.7: Entropy from the `MESA` simulation is shown in orange and a possible entropy profile to be used in 3D hydrodynamics simulation shown in blue. Both shown in `PPMStar` code units.

4.4.2 Multifluid Setup

As stated previously, the two fluid `PPMStar` code can lead to an overestimation of the energy generation at the boundary of the H and He-rich layers. One reason for this is because the mass fractions of both H and C are higher in the boundary layer than in the `MESA` model. All Pop III hydro simulations presented here suffer from this artefact (an example is shown in Fig. 4.2). Test simulations with the version

of the code including radiation pressure in the equation of state showed high energy generation and vortcity, and and the H-shell burns inward rapidly. This result can be seen in Fig. 4.8 and is likely at least partly due to the two fluid approximation. The other contributing factor is discussed in Section 4.4.3.

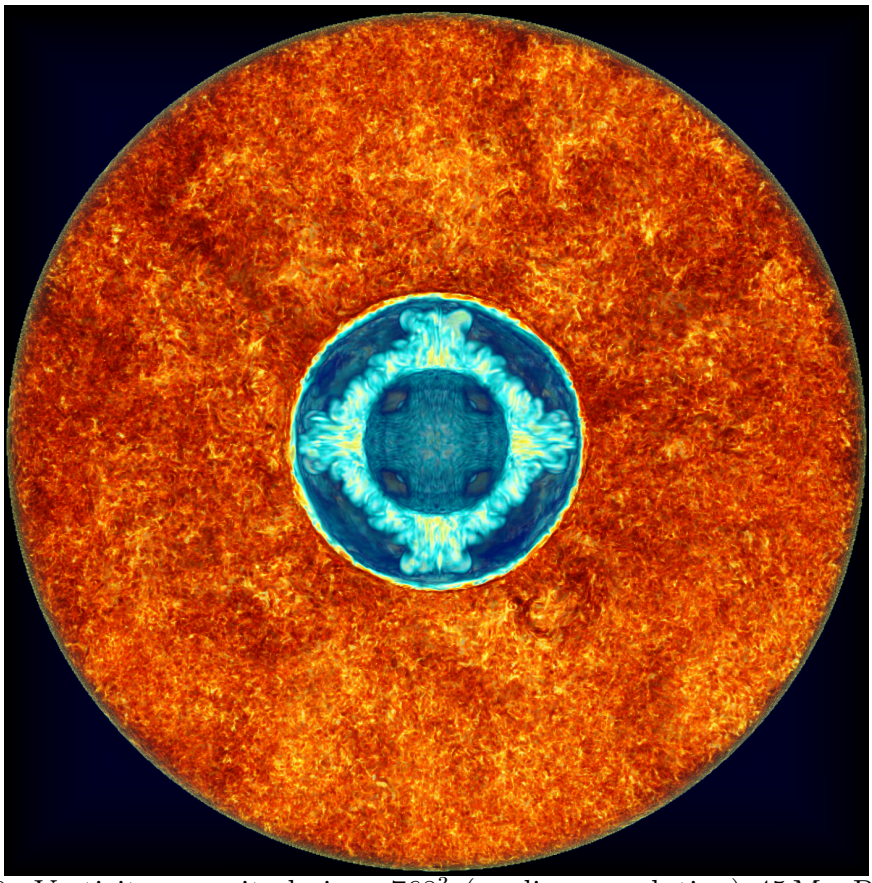

Figure 4.8: Vorticity magnitude in a 768^3 (medium resolution) $45\,\mathrm{M}_\odot$ Pop III test simulation of a He and partial H shell with radiation pressure and nuclear burning included. Image taken at 4.5 hrs simulation time. Strong grid imprints can be seen as convection in the He shell is not able to establish fully due to the strong burning taking place above.

Starting from my original setup script, I also created a script to produce initial conditions for three fluid simulations. The difference in the multifluid setup is shown in Fig. 4.5. This setup assumes there are three fluids, F_1, F_2 and F_3. In the `PPMStar` code fractional volumes, $FV_i \equiv \rho_i X_i/\rho$, are used to track the various fluids. I use this fact to distribute the relevant elements, H, He, C, N and O such that FV_i, μ_i and X_i are all consistent within their various constraints and with each other. The multifluid setup is similar to the two fluid setup shown in Appendix B. The major

differences are shown in Fig. 4.5 and also include various tests that ensure consistency. Fig. 4.9 shows the initial distribution of the mass fractions for each species in `MESA` and Fig. 4.10 shows the final distribution of each of the three fluids plus the sum of the three which must be equal to unity. At the time of writing this thesis, the multifluid version of the `PPMStar` code has not been fully tested.

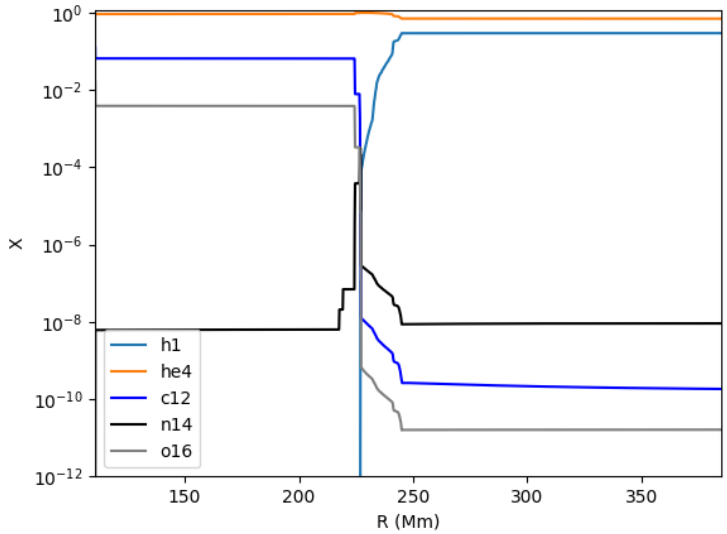

Figure 4.9: Composition of relevant elements in `MESA` model to be used in multifluid simulations.

4.4.3 Network

While a reaction network has not yet been implemented for the three fluid code, preliminary attempts could use a simple modified two reaction network. For each fluid there exists a fractional volume, FV_i, mass fraction, X_i, and constituent mass fractions, $x_{i,j}$, (Fig. 4.11). The simplest solution would be to use the existing reaction network, which includes the $^{12}\mathrm{C}(p,\gamma)^{13}\mathrm{N}$, treating the radiative layer fluid, F_2 as an inert buffer layer. This does not account for additional CNO reactions though and this reaction is only $\sim 7\%$ of the total energy in the CNO cycle, which initially could remain represented by the cooling region.

In previous code versions, the resulting *ash* or daughter products were placed back into the He-rich material, i.e. $^{12}\mathrm{C} + p \rightarrow^{12}\mathrm{C} + Q$. This is not appropriate for the two convection zone simulations as it leads to a runaway effect if F_1 is mixed

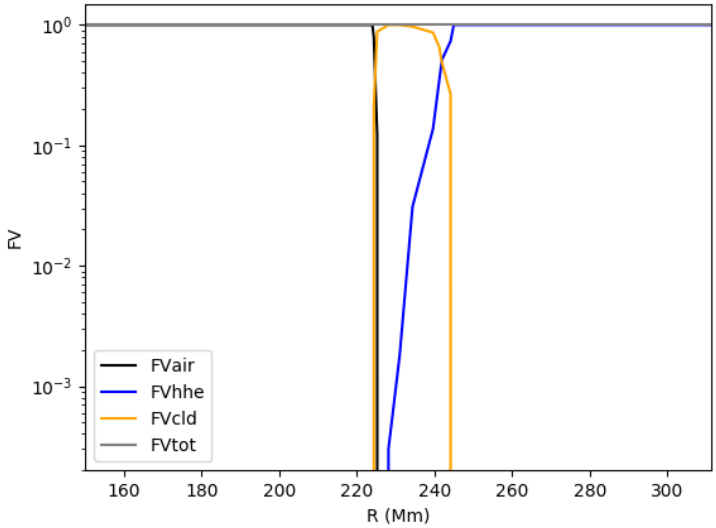

Figure 4.10: FV of each of the three fluids for multifluid runs. The names on the image label refer to the terminology used in `PPMStar` for the three fluids.

upward. i.e., you mix ^{12}C into the H-rich region, the $^{12}\mathrm{C}(p,\gamma)$ reaction occurs and the reaction leaves behind more ^{12}C. This worked well for other simulations where the H-shell was radiative and protons would only ever mix downward. In this case, C can and does mix upwards into the H-shell as well. This could be remedied by simply determining which fluid the ash goes into based on location or any state variable. Any assumptions would only break down if there were significant expansion, which breaks other assumptions as well, such as fixed g.

For the standard CNO1 cycle, the fastest reactions are typically the β decays, with timescales from 10-100 min. The total *cycle time* for CNO1 in the H shell of the $45\mathrm{M}_\odot$ model is dominated by the slowest reaction, $^{14}\mathrm{N}(p,\gamma)^{15}\mathrm{O}$. ^{14}N has a mean lifetime against proton capture of about 500 min at the base of the H shell. If the CNO1 cycle is in equilibrium (steady state), additional energy can be added when F_1 and F_3 mix in this region to account for the entire cycle. At this point it is not clear how a H-He interaction may evolve in 3D and if that is a valid assumption. If it is not valid when (if), CNO catylst (F_1) is mixed upward into the H shell, this can no longer be assumed because the timescales for the CNO1 reactions span two orders of magnitude and timesteps in `PPMStar` are less than 1 s. Results from Chapter 3 indicate that equilibrium is not maintained but this would have to be tested for verification.

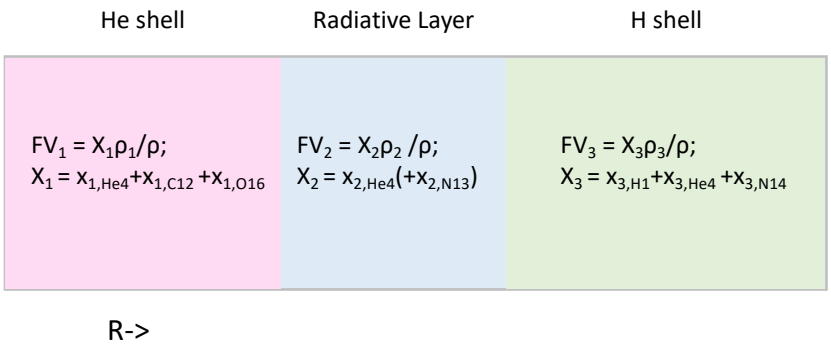

Figure 4.11: Illustration of the Pop III three fluid configuration and composition. Not to scale

4.5 Conclusions

Modelling stars for 3D hydrodynamics is a challenging task, requiring careful consideration of many physical aspects of the model. Here I have demonstrated the necessity of 3D models for simulations of H-He interactions in Pop II stars and the various ingredients necessary to model them using the `PPMStar` code. I have also presented two separate frameworks created to create 1D to 3D mappings for either two-fluid or multi-fluid simulations. These setup frameworks are applicable to many stellar evolution scenarios beyond the Pop III case.

Chapter 5

Summary and Conclusions

5.1 Summary

Significant mixing between H and He layers may occur in stars and with higher frequency in Pop III stars than in their higher-metallicity counterparts. Discussion of these events was previously scattered about the literature

I have shown that these interactions may lead to the i process with neutron densities, $\log(N\mathrm{n}) \sim 13.5$. Starting with C as a seed, the i process is able to reproduce abundance signatures in some of the most iron-poor stars within the Milky Way's halo, HE 0107-5240 and HE 1327-2326. Particularly the light-element abundance signature, which can be seen in other CEMP-no stars as well. The final fate of these stars and outcome of H-He events is still uncertain but we suggest that some H-He interactions, where significant energy is produced due to nuclear reactions, may experience mass ejection events. These events could carry out the unique abundance signatures of the event and form a second generation of stars.

The work presented in Chapter 3 explored for the first time how these interactions behave when varying macroscopic mixing parameters in a grid of models from $15-140\,\mathrm{M}_{\odot}$. Here several new discoveries were presented. One such discovery was the identification of multiple types of H-He interactions within a single stellar evolution code. I also found that H-He interactions may lead to CNO isotopic and elemental ratios consistent with CEMP-no stars, something difficult to do without significant mixing. Furthermore, I also found that these events always occur during core contraction phases and identified the likely dominant physical causes. I found that in one case, where a convective H shell interacts with the radiative layer above He core,

Ne-Na and Mg-Al cycles were triggered, which could also have implications for light element abundances. The case is made for 3D hydrodynamic simulations to better understand aspects of these interactions beyond the predictive capabilities of MLT.

Finally, I discussed the treatment of H-He interactions in the `PPMStar` code. I created a script to create initial conditions to be used for Pop III H-He interaction simulations, which have already been used for these and other stellar hydrodynamics simulations as well. I also wrote a variation of this code to handle three fluid simulations. The unique properties of Pop III stars require special considerations compared to other scenarios previously explored with the `PPMStar`. These include the equation of state, nuclear reaction network and multifluid assumptions.

5.2 Future Prospects

While we are just now scratching the surface of H-He interactions this work highlights exciting avenues for future research into this phenomena. Foremost, would be the continuation of 3D hydrodynamics simulations. 3D hydrodynamics simulations using the correct equation of state, multifluid code and/or a well approximated nuclear reaction network would vastly improve our understanding of H-He interactions. This would allow one to simulate the various interaction types in full 4π geometry including associated instabilities, such as the Global Oscillation of Shell Hydrogen-Ingestion (GOSH) first observed in Herwig et al. (2014).

More observational data and better understanding of the existing data will also push this work forward. As suggested in the 1.3.3, the current classification system for CEMP stars may not be sufficient to properly differentiate the origins of different neutron capture signatures. This situation can be improved by obtaining detailed abundance patterns elemental abundances for trans-iron elements. Currently Ba and Eu are used to classify these stars and too frequently, this is the only data presented. Observations coming out the Gemini telescope's GHOST spectrograph (Such as data promised in Venn et al., 2020) will be able to determine abundances for more n-capture and trans-iron elements typically not included in optical surveys such as Nd, Y and Th. More theoretical work is needed to aid in this endeavour as well in order to clearly determine the important signatures of the i process. Furthermore, a greater number of high quality spectra from follow up studies can potentially help break degeneracy in theoretical models used to explain the origins of the elements in iron-poor and metal-poor stars. This is highlighted in Chapter 3, where various

theoretical models including different physics assumptions are used to explain certain observations. A larger sample of UMP stars from new or ongoing projects such as the Pristine survey, the EMBLA and Gaia-ESO surveys, and the 4MOST survey will also further our understanding and our ability to draw conclusions regarding both the nature of the first stars and both the chemical and dynamical history of our galaxy.

The James Webb Space Telescope (JWST) and the Nancy Grace Roman Space Telescope(formely known as WFIRST) are both infrared telescopes expected to provide new information on the first stars and Epoch of Reionization including possible observations of pair instability supernovae (Hartwig et al., 2018), locating the end of Reionization (Liu & Bromm, 2020) and the first galaxies (Vanzella et al., 2020) and possible even supermassive stars (Surace et al., 2019). If the conditions are correct, it may even be possible to view Pop III core collapse supernovae with gravitational lensing (Rydberg et al., 2020).

Future theoretical and observational work will greatly enhance our understanding of the first stars, the impact they had on their environment and the chemical abundances they left behind.

Appendix A

Supplementary Figures

The figures included here are from Appendix A of Clarkson & Herwig (2020), which is presented in this thesis as Chapter 3.

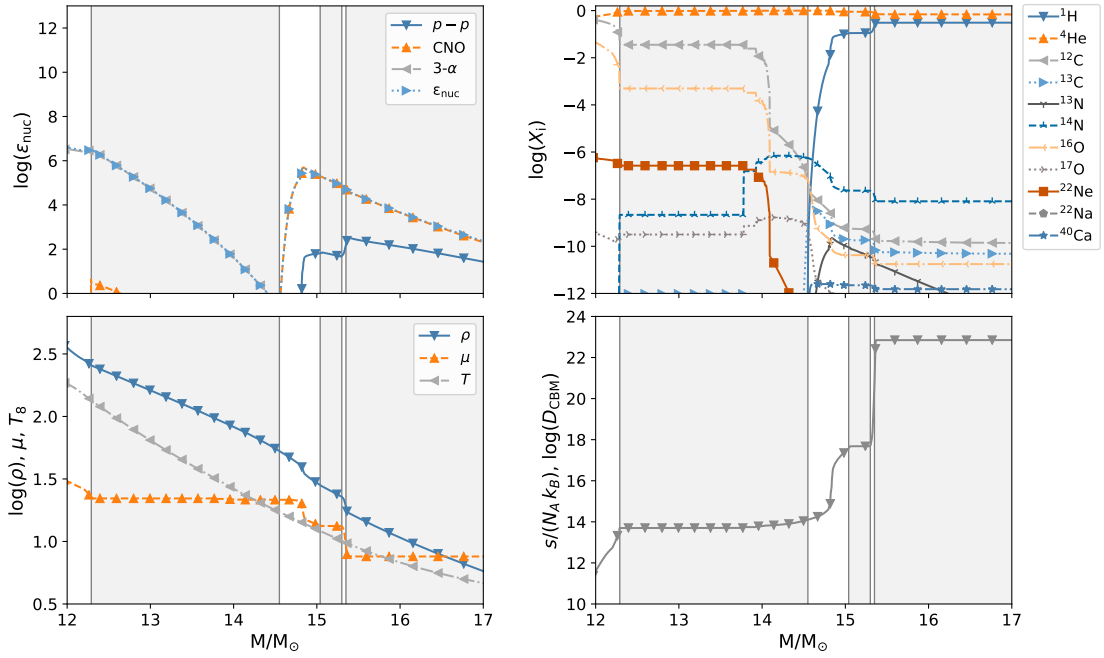

Figure A.1: Profiles for the `Conv-Shell` interaction `40Mled` model with the Ledoux criterion for convection and semiconvecton included. **Top left**: Total specific energy generation and that from CNO, p-p and tri-α reaction groups. **Top right**: Mass fractions of several abundant species. **Bottom left**: Temperature, mean molecular weight and density profiles. **Bottom right**: Specific entropy. Profiles taken $\approx 9\,\mathrm{yr}$ before the H-He interaction begins, at the same time as the top panel of Fig. A.3. Grey areas show regions unstable to convection.

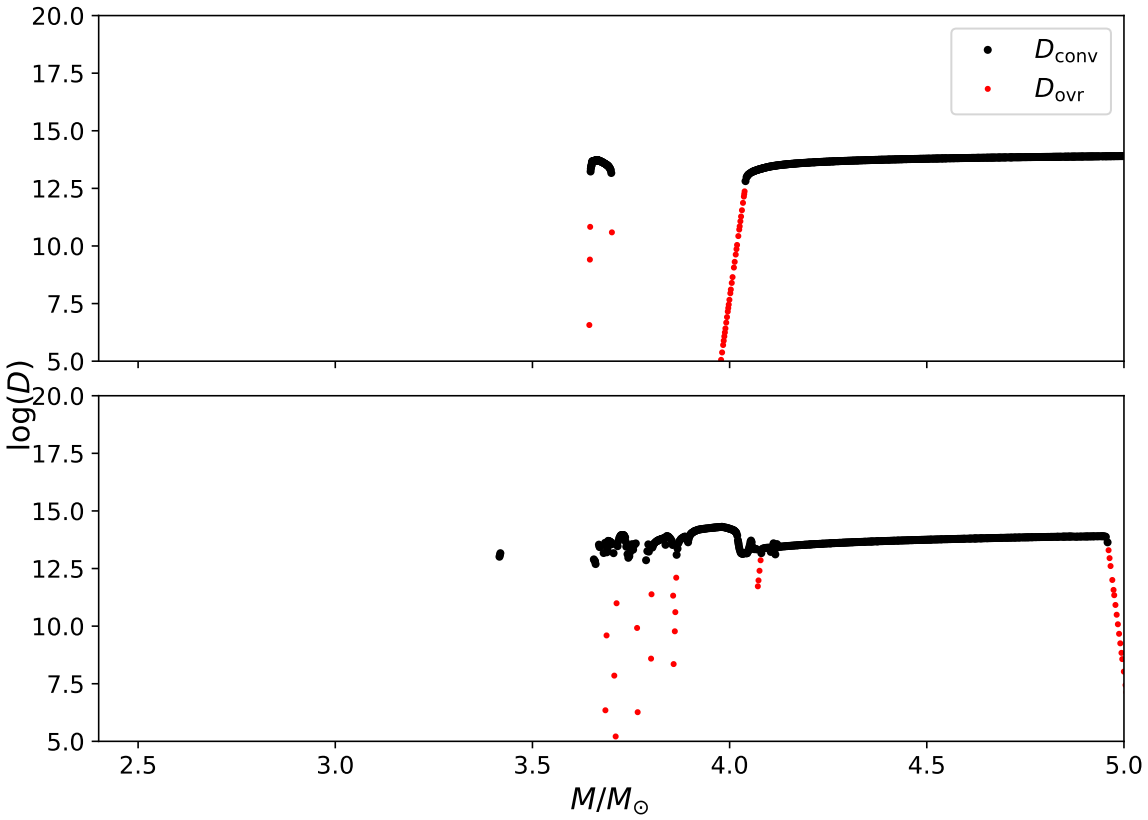

Figure A.2: **Top**: Diffusion coefficients for convection and CBM in the `15Mschf-h` model 277 yr before the H-He interaction begins. **Bottom**: Same quantities at the time shown in Fig. 3.5.

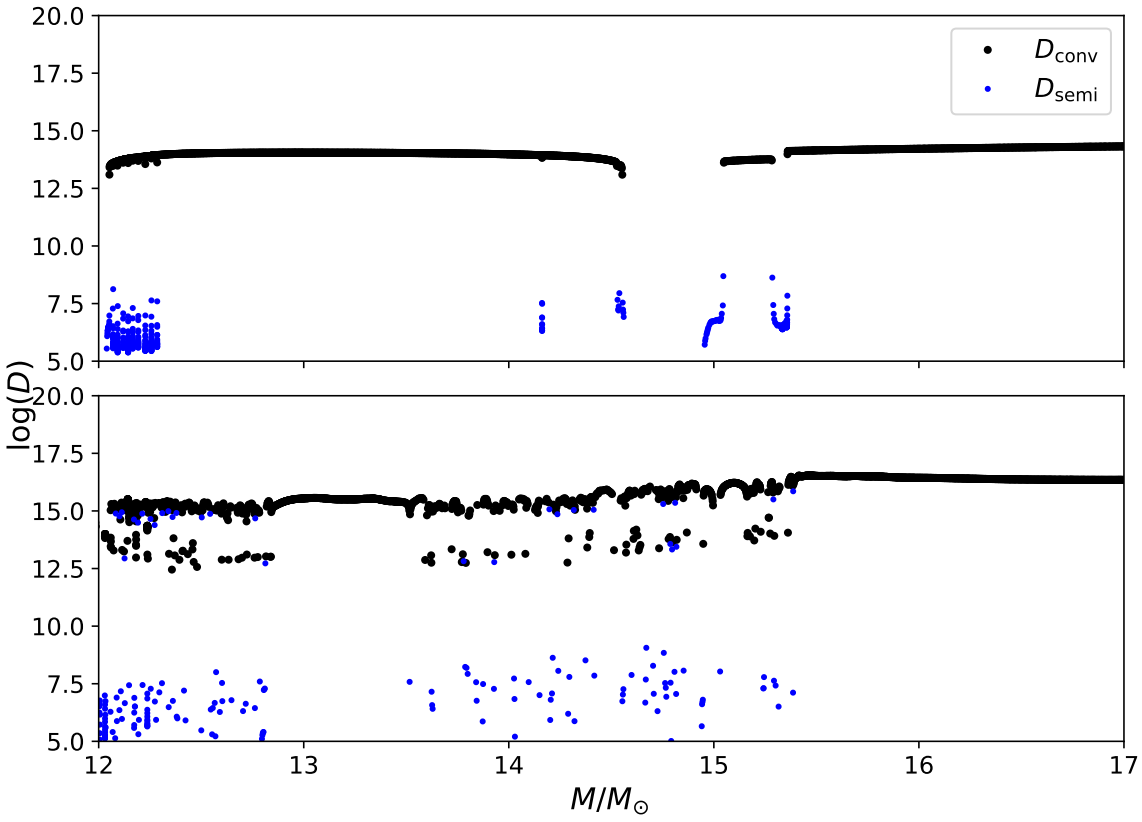

Figure A.3: **Top**: Diffusion coefficients for convection and semiconvection in the `40Mled` model 9 yr before the H-He interaction begins. **Bottom**: Same quantities at the time shown in Fig. 3.9.

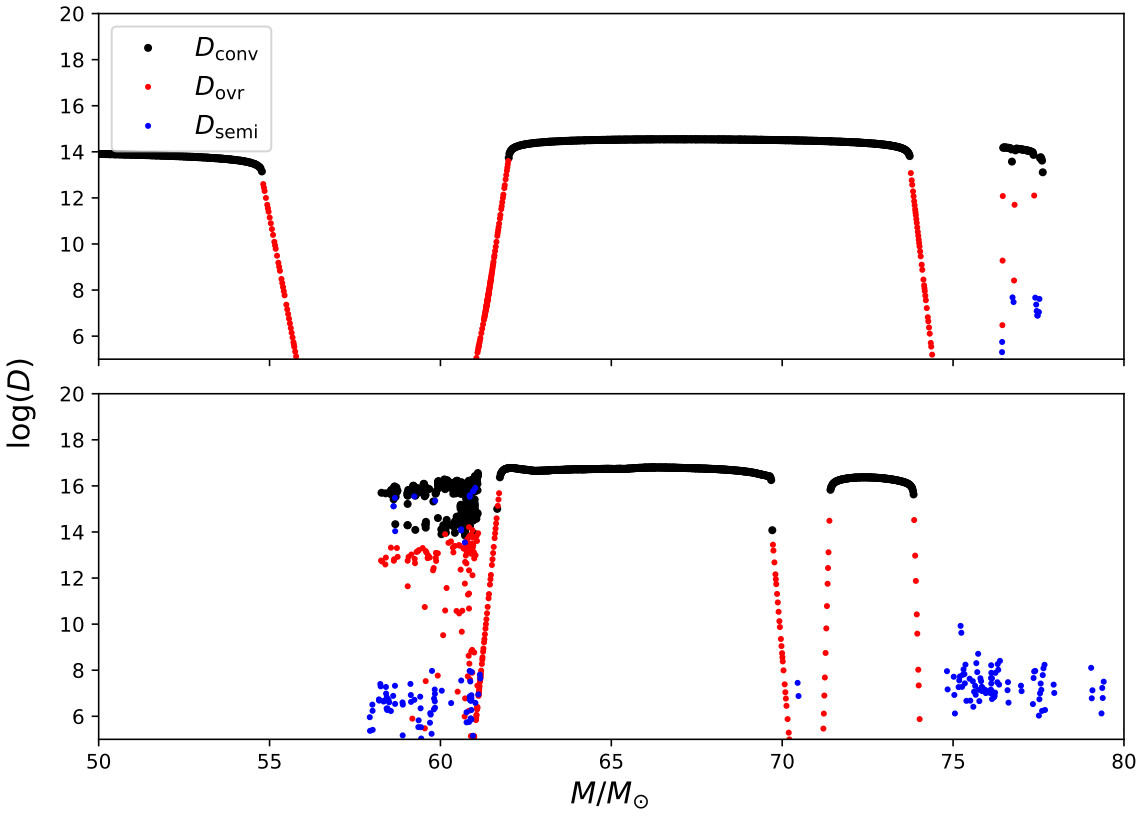

Figure A.4: **Top**: Diffusion coefficients for for convection, semiconvection, and CBM in the `140Mledf-h` model 262 yr before the H-He interaction begins. **Bottom**: Same quantities at the time shown in Fig. 3.11.

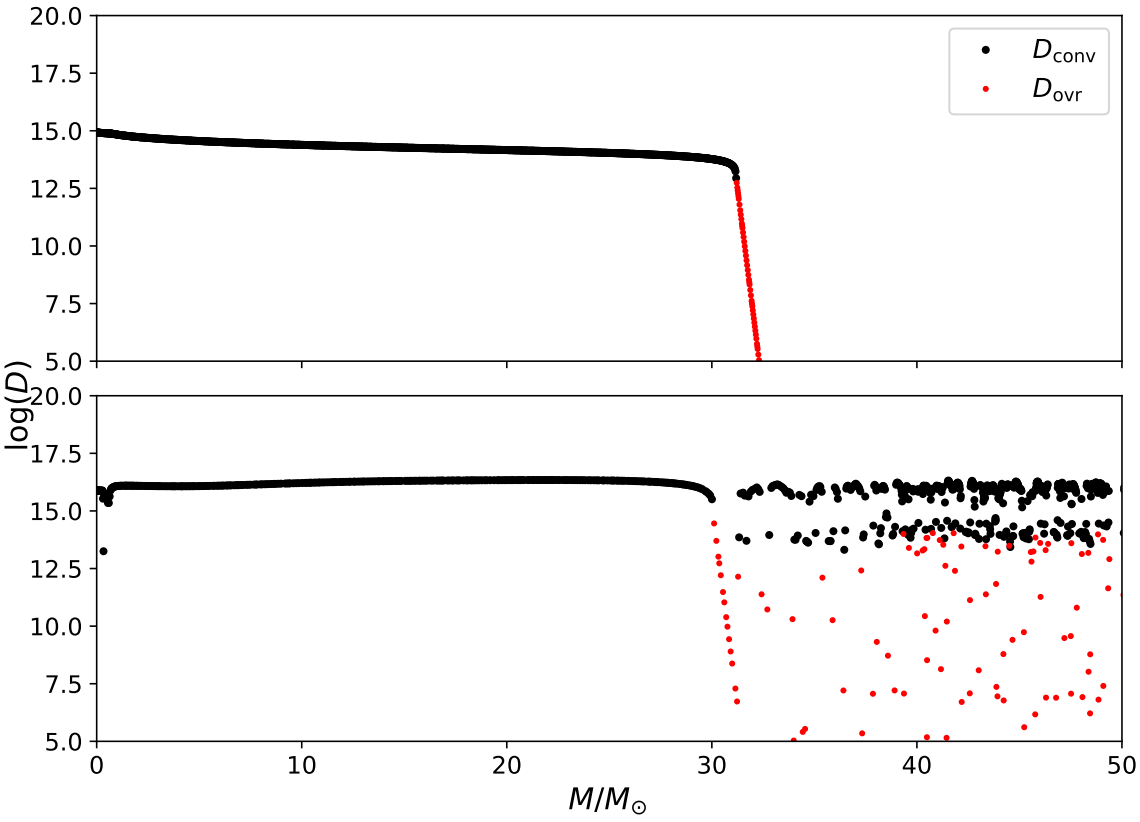

Figure A.5: **Top**: Diffusion coefficients for convection and CBM in the `80Mschf-h` model 27 yr before the H-He interaction begins. **Bottom**: Same quantities at the time shown in Fig. 3.13.

Appendix B

1D to 3D Mapping Code

The code which maps 1D stellar evolution models to initialize and provide a base state for 3D hydro simulations as described in Chapter 4 is presented here.

Master_setup_with_notes

October 17, 2020

1 NewEOS master setup notebook

To make a new setup copy and paste this notebook to your ppmstar/projects/project/setup directory and customize it there.
Do not edit this notebook.

See ppmstar/pylib/utils/setup_docs.ipynb for physics and numerical documentation for the setup

1.1 The mixture of ideal gas and radiation

According Cox & Guili the pressure, specific internal energy (per unit mass) and entropy are

$$\begin{aligned} P &= P_{\rm gas} + P_{\rm rad} &= \frac{\mathcal{R}}{\mu}\rho T + \frac{1}{3}aT^4 \\ E &= E_{\rm gas} + E_{\rm rad} &= \frac{\frac{\mathcal{R}}{\mu}T}{(\gamma_{\rm g}-1)} + \frac{aT^4}{\rho} \\ S &= S_{\rm gas} + S_{\rm rad} &= c_V \log T - \frac{\mathcal{R}}{\mu}\log\rho + \frac{4}{3}\frac{aT^3}{\rho} + \text{const.} \end{aligned}$$

Using the gas pressure fraction $\beta = \frac{P_{\rm gas}}{P}$ the sound speed can be obtained from

$$\Gamma_1 = \beta + \frac{(4-3\beta)^2(\gamma_{\rm g}-1)}{12(1-\beta)(\gamma_{\rm g}-1)+\beta}$$

1.2 Entropy for an ideal gas

$$A = \frac{P}{\rho^{\frac{5}{3}}} S(A) = \frac{3\mathcal{R}}{2}\log A + const \frac{dS}{dr} = \frac{dS}{dA}\frac{dA}{dr} = \frac{3}{2}\frac{R}{A}\frac{dA}{dr}$$

1.3 Structure equations

We want to know how these values change radially in a spherically symmetric, hydrostatic star. To do this we use the equations for hydrostatic equilibrium and mass distribution:

$$\begin{aligned}\frac{dP}{dr} &= -\frac{Gm}{4\pi r^4} \\ \frac{dm}{dr} &= 4\pi r^2 \rho\end{aligned}$$

1.4 Sound speed

$$\begin{aligned}c_s^2 &= \left(\frac{\partial P}{\partial \rho}\right)_{\rm ad} \\ \Gamma_1 &= \left(\frac{d\ln P}{d\ln \rho}\right)_{\rm ad} \\ c_s^2 &= \Gamma_1 \frac{P}{\rho}\end{aligned}$$

For an ideal gas $\Gamma_1 = \gamma_{\rm g}$ and $c_s^2 = \frac{\gamma_{\rm g} P}{\rho}$

[1]:
```
%pylab ipympl
from IPython.display import Image
from nugridpy import astronomy as ast
from nugridpy import mesa as ms
import sys
sys.path.insert(1,"/user/scratch14_wendi3/Ondrea/repos/PyPPM")
from ppmpy1 import ppmsetup as ps
from scipy import interpolate
from nugridpy import ascii_table as at
import nugridpy.constants as nuconst
```

```
Populating the interactive namespace from numpy and matplotlib
```

[2]:
```
from contextlib import contextmanager
import os

@contextmanager
def suppress_stdout():
    with open(os.devnull, "w") as devnull:
        old_stdout = sys.stdout
        sys.stdout = devnull
        try:
            yield
        finally:
            sys.stdout = old_stdout

import warnings
warnings.filterwarnings("ignore")
```

[3]:
```
import logging  #this supresses annoying debug messages on gold. Not necessary␣
↪for the notebook itself.
logger = logging.getLogger()
logger.setLevel(logging.ERROR)
```

1.5 Find some mesa data to model the setup after

We are starting here with a $45M_{\odot}$ Pop III H-He interaction.

[4]:
```
model = 2885
ddir = '/data/ppm_rpod2/Stellar_models/PopIII/45M_led_mingap_letter_hdf/LOGS'
```

[5]:
```
M = ms.star_log(ddir)
```

```
Using old history.datasa file …
 reading …100%
```

1.6 Step 1 plt.plot a Kippenhahn diagram to help determine which model number you want to use

Use `ppmsetup.get_prof_data` to load all the data you need for the setup itself. You may also want to load and plt.plot variables such as Pgas/Ptotal, sound speed and the radiative and adiabatic gradients to see the structure in your profile. The latter three aren't loaded automatically with `get_prof_data`.

[6]:
```
close(1);figure(1)
with suppress_stdout():
    M.kip_cont(ifig=1,mix_zones=50,burn_zones=50)
vlines(2885,0,45,linestyles='dotted')
savefig('kip.png')
```

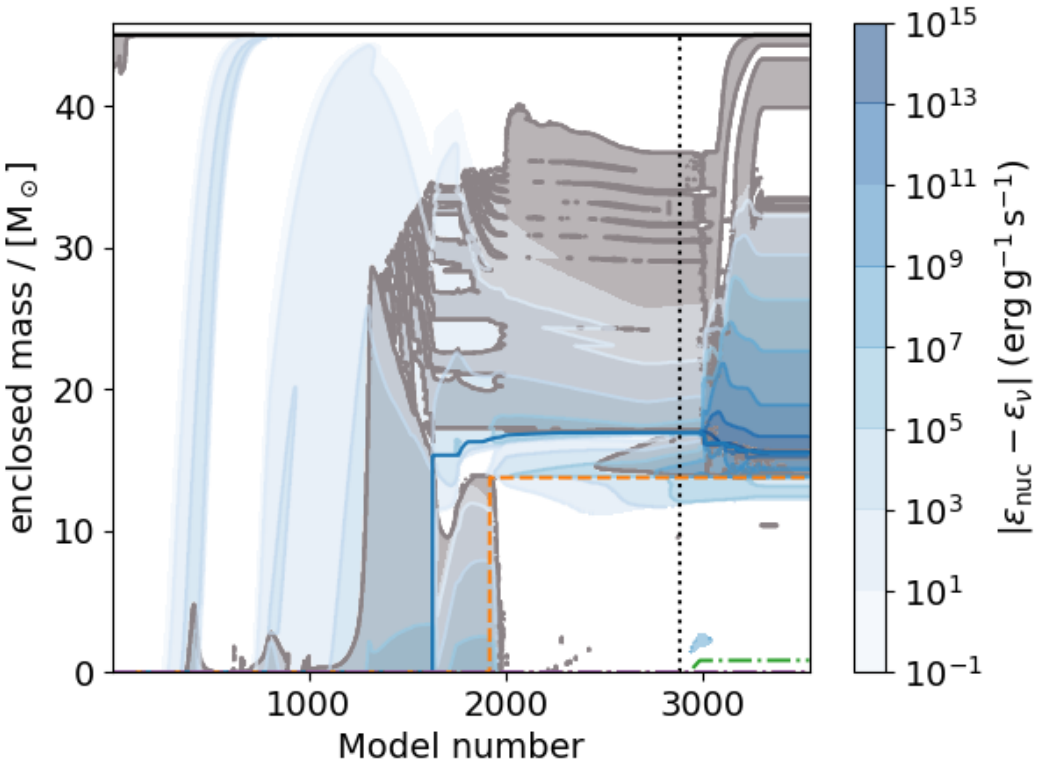

[8]:
```
with suppress_stdout():
    log_conv_vel, radius_mesa, P_mesa, T_mesa, entropy_mesa, rho_mesa,␣
↪mass_mesa, mu_mesa ,\
    pgas_div_ptotal = ps.get_prof_data(ddir,model)  #loads in all mesa profile␣
↪data needed. NOT GENERAL
```

1.7 Step 2

We transform the mesa data into code units and then do the integration in code units. Physical constants a, R and G are included in ppmsetup.py in both cgs and ppm units for the first two. G is just im ppm units.

1.7.1 Code units

```
c         1 unit of length = 1000 km = 1 Mm = 10**8 cm.
c         1 unit of velocity = 1000 km/sec = 10**8 cm/sec = 1 Mm / sec
c         1 unit of time = 1 sec
c         1 unit of density = 1 kgm/cc = 1000 gm/cc = 10**27 gm / Mm**3
c         1 unit of mass = 10**27 gm = 5.025e-07 solar masses
```

```
c                                    = 1/6 earth masses
c                1 solar mass = 1.99 * 10**30 kg.
c                1 earth mass = 6.0e+24 kg.
c          1 unit of energy = 10**27 gm * 10**16 cm**2/sec**2
c                           = 10**43 ergs
c                1 unit of energy per unit volume = 10**43 / 10**24 cgs
c          1 unit of pressure = 1000 (gm/cc) * (10**8 cm/sec)**2
c                             = 10**19 gm/(cm-sec**2)
c          1 unit of acceleration = 10**8 cm/sec/sec
c          1 unit of temperature = 10**9 degrees Kelvin = GK
```

[12]:
```
#could change this so it does not have to read the mesa data again
with suppress_stdout():
    rho_code = ps.UnitConvert(quantity='density', convertto='PPMUnits',␣
 ↪modordump=model, datadir = ddir)
    P_code = ps.UnitConvert(quantity='pressure', convertto='PPMUnits',␣
 ↪modordump=model, datadir = ddir)
    T_code = ps.UnitConvert(quantity='temperature', convertto='PPMUnits',␣
 ↪modordump=model, datadir= ddir)
    radius_code = ps.UnitConvert(quantity='radius',convertto='PPMUnits',␣
 ↪modordump=model, datadir= ddir)
    m_code = mass_mesa*nuconst.m_sun/1e27
```

[13]:
```
close(114);figure(114)
plot(radius_code,pgas_div_ptotal,label='pgas_div_ptotal')
plot(radius_code,log_conv_vel/max(log_conv_vel[200:-1]),label='log vconv / log␣
 ↪vconvmax')
ylim(0.2,1.05); xlim(0,600)

legend()
savefig('p_ptot.png')
```

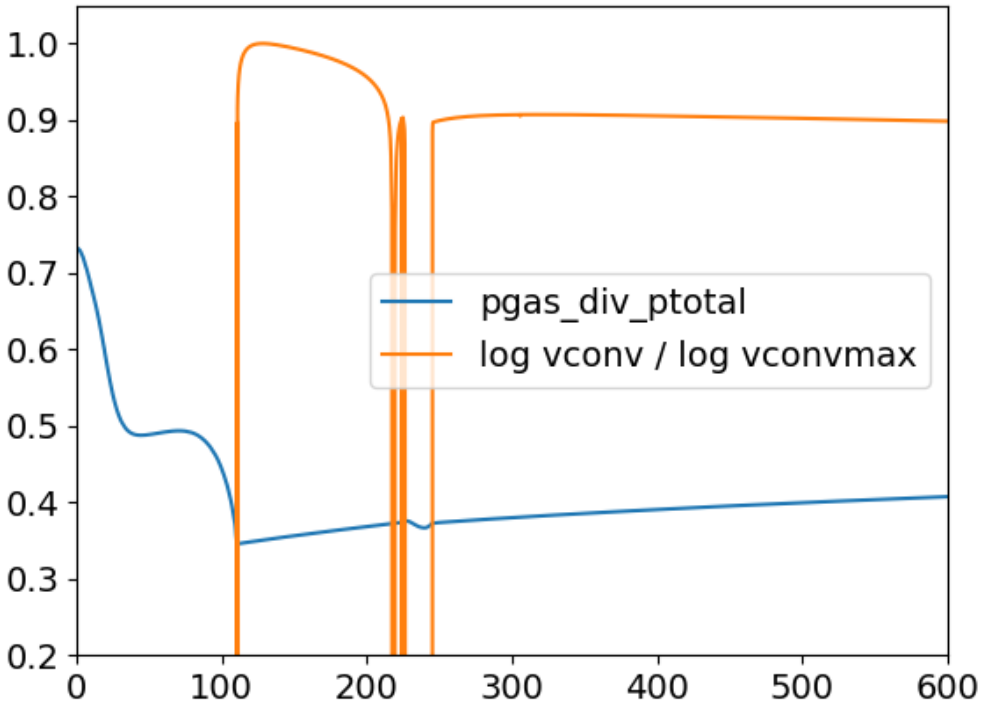

1.8 Step 3

Once you have looked at your profile, you will need information from the extracted profile to begin the setup. You will want to get the indices in the mesa profile for the top and base of the convection zone(s)

1.9 Defining setup for a double shell simulation

[15]:
```
# If you are not doing a double shell problem you don't need this cell but you␣
↪can see two of these indicies are used in the cell below this one.
bothe = 13.896
tophe=224
both=245  #radius in Mm for this one only
toph = 19.0

idxhebot = np.argmin(np.abs(mass_mesa-bothe))
idxhetop = np.argmin(np.abs(radius_code-tophe))
idxhbot = np.argmin(np.abs(radius_code-both))
idxhtop = np.argmin(np.abs(mass_mesa-toph))
```

```
print(mu_mesa[idxhebot-30])
print("bottom of he shell = ", radius_code[idxhebot-30],"Mm")
print("top of he shell = ", radius_code[idxhetop],"Mm")
print("bottom of h shell = ", radius_code[idxhbot],"Mm")
print("top of h shell = ", radius_code[idxhtop],"Mm")
print("average mu for he shell =", (mu_mesa[np.argmin(np.
 ↪abs(mass_mesa-tophe))]+mu_mesa[np.argmin(np.abs(mass_mesa-bothe))])/2 )
print("average mu for h shell =", (mu_mesa[np.argmin(np.
 ↪abs(mass_mesa-toph))]+mu_mesa[np.argmin(np.abs(mass_mesa-both))])/2)
```

```
1.354429837010161
bottom of he shell =  110.86261296656872 Mm
top of he shell =  224.0391751863432 Mm
bottom of h shell =  244.99759646778742 Mm
top of h shell =  426.8546465913972 Mm
average mu for he shell = 0.9959640466339974
average mu for h shell = 0.7510180717441147
```

1.9.1 The cell below is critical. You really don't want any transition to be < 7 cells on a 756 run

[16]:
```
ngrid = 756//2                # number of grid zones in PPMstar in one radial␣
 ↪direction
radmax= radius_code[idxhtop]+30 #boundary
dx    = radmax/(ngrid)          # grid zone in PPMstar

radin0 = 90 #g starts turning on
idxradin0 = np.argmin(np.abs(radius_code-radin0))
radinner = 100 # g full on
idxradinner = np.argmin(np.abs(radius_code-radinner))
radbase = radius_code[idxhebot]

radtop =radius_code[idxhtop]
radouter = radmax-20#g starts turning off
idxradouter = np.argmin(np.abs(radius_code-radouter))
radout0 = radmax-12.5 #g off
idxradout0 = np.argmin(np.abs(radius_code-radout0))

ncore = int(radin0//dx)         # number of grid zones in inert core
Ravedge = 15*dx
Nconv = Ravedge/5*dx
print("Ravedge(total R smoothed) =",Ravedge, "Nconv(smoothing length)=", Nconv)
```

```
Ravedge(total R smoothed) = 18.129152642515763 Nconv(smoothing length)=
4.382215673808483
```

[17]:
```
print(radin0, radinner, radbase, radtop, radouter, radout0)
print("each cell is",dx, "Mm")
print("core is",ncore,"cells in radius")
print((radinner-radin0)/dx,"cells where g turns on")
print((radbase-radinner)/dx,"cells to transition to base")
print((radouter-radtop)/dx,"cells to transition to where g turns off")
print((radout0-radouter)/dx,"cells where g turns off")
```

```
90 100 110.73890463320912 426.8546465913972 436.8546465913972 444.3546465913972
each cell is 1.2086101761677175 Mm
core is 74 cells in radius
8.273966409672452 cells where g turns on
8.885333621184811 cells to transition to base
8.273966409672452 cells to transition to where g turns off
6.2054748072543395 cells where g turns off
```

[18]:
```
#This cell should especailly be run if this is a fresh set up. PPM needs these.
with suppress_stdout():
    a = ms.mesa_profile(ddir,model)

ps.get_burning_coeffs(a, radbase+(radius_code[idxhetop]-radbase)/2, 'c12') ␣
 ↪#From the middle of the convection zone
ps.get_burning_coeffs(a, radtop+(radtop-radius_code[idxhbot])/2, 'h1')
```

```
Mass fractions of species with X > 1.0e-03 at r = 167.356 Mm:
he4 0.9303982810012608
c12 0.06571066730372785
o16 0.003887289351681887
Average mass number: 4.196063
Number fraction of fuel (c12): 0.022977

Mass fractions of species with X > 1.0e-03 at r = 517.780 Mm:
h1 0.2974578297796805
he4 0.702542160841672
Average mass number: 2.113748
Number fraction of fuel (h1): 0.628751
```

[18]:
```
(2.1137476490082348, 0.6287507883758914)
```

1.10 Step 4

Make a mock ppm entropy profile to interpolate over (for a nice set of values to give PPMStar). To do this use the ppmsetup.EOSgasrad function. You give this function your mesa data converted to ppm units and it returns both entropy and pressure.

[19]:
```
S_code,P_code=ps.EOSgasrad(T_code,rho_code,mu_mesa,ps.a_code,ps.R_code)

f_muint  = interpolate.interp1d(radius_code,mu_mesa, kind='linear')
f_Tint   = interpolate.interp1d(radius_code,T_code,  kind='linear'); T0    =␣
 ↪f_Tint(radbase)
f_rhoint = interpolate.interp1d(radius_code,rho_code,kind='linear'); rho0  =␣
 ↪f_rhoint(radbase)
f_mint = interpolate.interp1d(radius_code,m_code,kind='linear');  m0    =␣
 ↪f_mint(radbase)
#print(m0)
```

1.11 Step 5

plot the entropy profile. I have included four points I selected and altered myself to the plt.plot. These points are to ultimately be added to the setup file. I will interpolate between them plus ~5 more points defining the radiative region between the two convection zones. The plt.plot below is just for me to see what I am doing and store the limits for the next plt.plot.

[20]:
```
# first make S plot and zoom in to range for picking values
close(345),figure(345)

#Here I set beforehand the values at the top and bottom of each convection zone␣
 ↪as we need them constant
#then plot them to see if they are well placed
S_he_pts =␣
 ↪[S_code[idxradin0],S_code[idxradinner],S_code[idxhetop],S_code[idxhetop]],\
            [radius_code[idxradin0],radius_code[idxradinner],radbase,224.05]
S_h_pts = [[S_code[idxhtop], S_code[idxhtop],␣
 ↪S_code[idxradouter],S_code[idxradout0]],\
          ␣
 ↪[radius_code[idxhbot],radius_code[idxhtop],radius_code[idxradouter],radius_code[idxradout0]]
scatter(S_he_pts[1],S_he_pts[0], c='red')
scatter(S_h_pts[1],S_h_pts[0], c='red')

yl,xl=[9,75],[radin0-10,radout0+10]
plot(radius_code,S_code,label='mesa model in code units')
#plot(radius_points,S_points,'o-',label='points') # once points are selected␣
 ↪below, uncomment and check points
legend(loc=0)
xlabel('radius');ylabel('S')
set_lims = True
if set_lims:
    xlim(xl)
    ylim(yl)
savefig('S1.png')
```

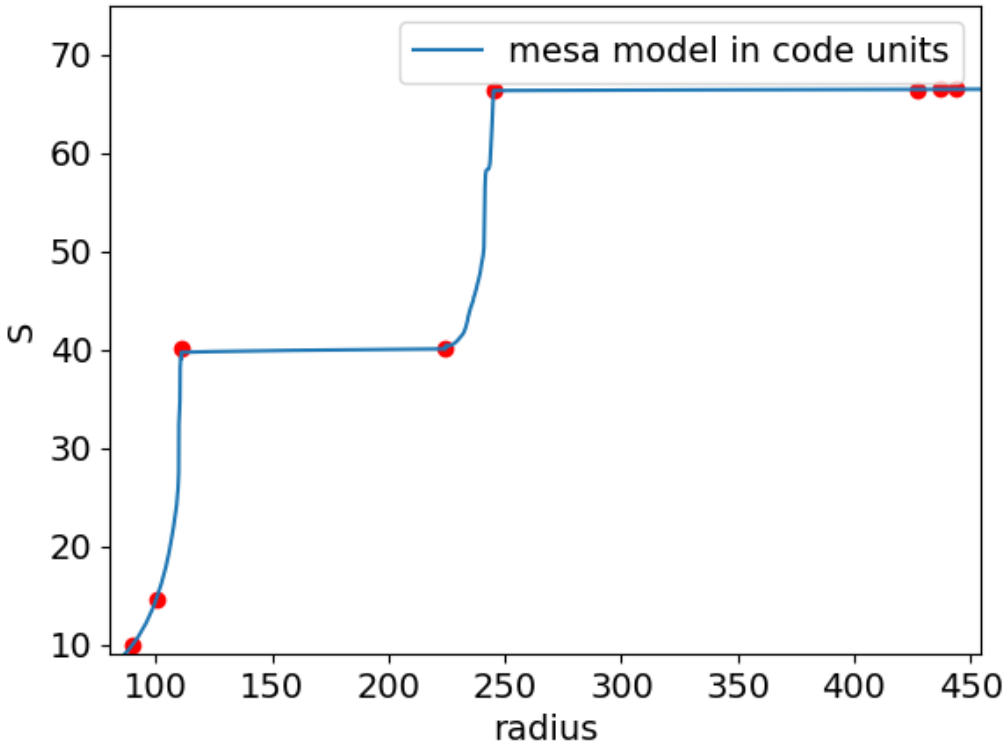

1.12 Step 6

This is where you click to define your S points for PPMStar. Not the the first click can make the page move a bit but it did work. Just keep on clicking where you want the points after it.

[22]:
```
# use this cell to select points by clicking on the graph.
# you can't change the zoom while you select points
# so you have to go in 2-3 attempts
# parameters to set

npoints_select = 8   # how many points to be seleted, will be written into␣
↪list coords
overplot_selected_points = False #only set to true if you have selected the␣
↪points once before
```

```
set_lims = True
xl=(220,260)
yl=(39,68)

close(1002)
fig = figure(1002, figsize=(10,8))
ax = fig.add_subplot(111)
scatter(S_he_pts[1],S_he_pts[0], c='red')
scatter(S_h_pts[1],S_h_pts[0], c='red')

if overplot_selected_points: ax.
 ↪plot(radius_points,S_points,'--o',label='points')
ax.plot(radius_code,S_code,label='mesa')
if set_lims:
    xlim(xl)
    ylim(yl)
coords = []

def onclick(event):
    '''
    This functions allows one to interactively click on a plot and store points.
 ↪ Not working from ppmsetup.py
    '''
    global ix, iy
    ix, iy = event.xdata, event.ydata
    print('x = %d, y = %d'%(ix, iy))

    global coords
    coords.append((ix, iy))

    if len(coords) == npoints_select:
        fig.canvas.mpl_disconnect(cid)

cid = fig.canvas.mpl_connect('button_press_event', onclick)
savefig('S2.png')
```

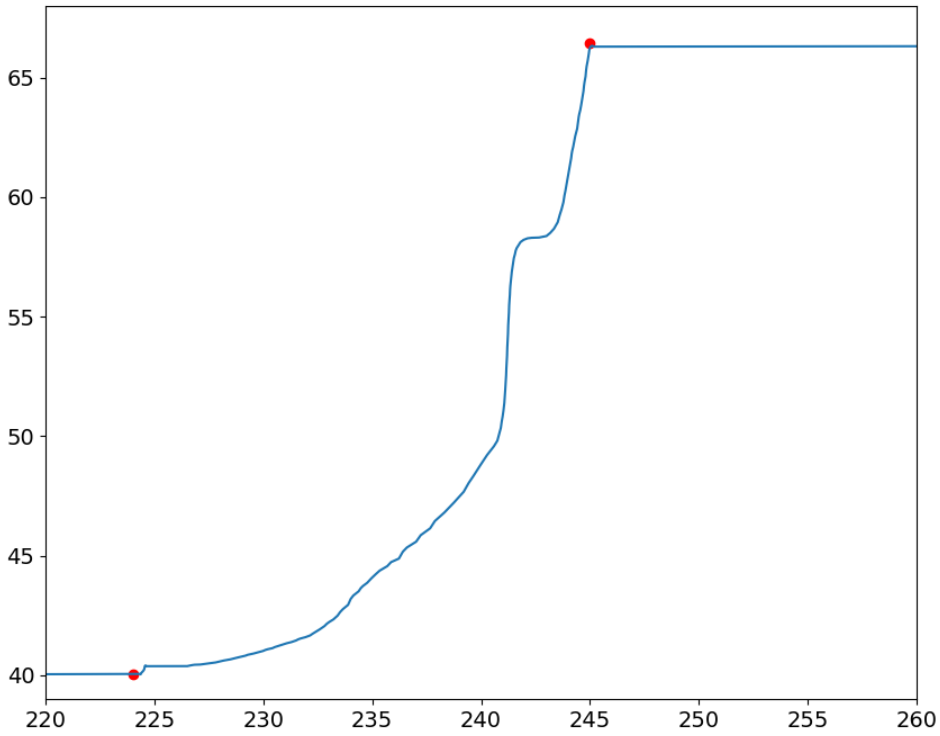

[23]:
```
# check recorded
coords
```

[23]:
```
[(224.83539511746145, 40.156379942712334),
 (227.6180038131136, 40.4877683960395),
 (230.6250164358345, 41.098037756308855),
 (234.66428712307155, 43.626296534567636),
 (238.47915388323986, 46.85200601027711),
 (240.81295472475458, 49.90335281162391),
 (242.38378221423562, 54.262419670690775),
 (243.59556342040673, 59.05739321566432)]
```

[24]:
```
rrr=list(array(coords).T[0])
sss=list(array(coords).T[1])
print([ '%.3f'%x for x in rrr ])
print([ '%.3f'%x for x in sss ])
```

```
['224.835', '227.618', '230.625', '234.664', '238.479', '240.813', '242.384',
'243.596']
```

```
['40.156', '40.488', '41.098', '43.626', '46.852', '49.903', '54.262', '59.057']
```

[25]:
```
radius_points = array(S_he_pts[:][1]+rrr+S_h_pts[:][1])  #combine the points I␣
 ↪chose an the ones obtained by clicking
S_points      = array(S_he_pts[:][0]+sss+S_h_pts[:][0])
```

[26]:
```
# one way to get mu values is to interpolate for the picked radii in the
# mesa my profile. this is done here, but check values grpahically and change by
# hand if needed; in the example below three innermost hand-picked values
# are combined with interpolated values for the outer points
mu_points_int = f_muint(radius_points[4:-4])
mu_points =␣
 ↪array([mu_mesa[idxhetop]]+[mu_mesa[idxhetop]]+[mu_mesa[idxhetop]]+[mu_mesa[idxhetop]]+\
                ␣
 ↪list(mu_points_int)+[mu_mesa[idxhbot]]+[mu_mesa[idxhbot]]+[mu_mesa[idxhbot]]+[mu_mesa[idxhb
print(mu_points)
```

```
[1.35425544 1.35425544 1.35425544 1.35425544 1.33587291 1.33309044
 1.33147016 1.29128097 1.23046374 1.16623186 1.01504427 0.9953395
 0.89314435 0.89314435 0.89314435 0.89314435]
```

[27]:
```
close(346);figure(346)
plt.plot(radius_points,mu_points,label='mu_points')
plt.plot(radius_code,mu_mesa,label='mu_mesa')
plt.xlim(xl)
plt.legend()
savefig('mu.png')
```

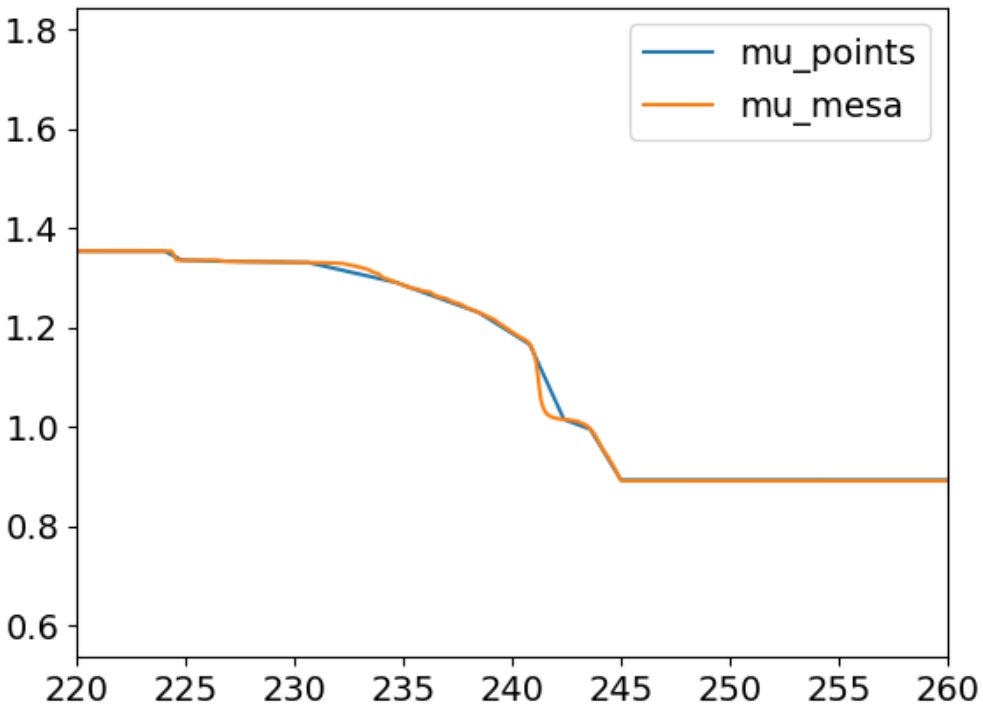

1.13 Print setup file. If you are just making the setup you can stop after this.

At this point we have a set of 10-15 triples (r, S, mu) which are defining the setup. Print into setup.dat file.

[29]:
```
#round floats
mu_points = np.round(mu_points,3)

S_points = np.round(S_points,3)

radius_points = np.round(radius_points,3)
```

[30]:
```
T0=T0; rho0=rho0; mu=f_muint(radbase)
Sdum,P0 = ps.EOSgasrad(T0,rho0,mu,ps.a_code,ps.R_code)
headers = ["M45, Z=0","Constructed by Ondrea, Oct 2020", "all quantities in␣
↪code units",\
           "mesa_data_dir:/ppm_rpod2/Stellar_models/PopIII/
↪45M_led_mingap_letter_hdf/", "mesa_dump:2885","Inner boundary:",\
           "pressure P0 = " + str(np.round(P0,3)), \
           "mass m0     = " + str(np.round(m0,3)),\
```

```
           "Ravedge     = " + str(np.round(Ravedge,3))]
dcols   = ['radius','S','mu']
data    = [radius_points,S_points,mu_points]
at.write('LDoubleshell_master.dat', headers, dcols, data)
```

```
Warning this method will overwrite ./LDoubleshell_master.dat
Would you like to continue? (y)es or (n)no?

-->  yes

Yes selected
Continuing as normal
```

[31]:
```
cat LDoubleshell_master.dat
```

```
H M45, Z=0
H Constructed by Ondrea, Oct 2020
H all quantities in code units
H mesa_data_dir:/ppm_rpod2/Stellar_models/PopIII/45M_led_mingap_letter_hdf/
H mesa_dump:2885
H Inner boundary:
H pressure P0 = 2.031
H mass m0     = 27641708.302
H Ravedge     = 18.129
  radius    S         mu
  90.0350   10.0170  1.3540
  100.0060  14.5530  1.3540
  110.7390  40.0490  1.3540
  224.0500  40.0490  1.3540
  224.8350  40.1560  1.3360
  227.6180  40.4880  1.3330
  230.6250  41.0980  1.3310
  234.6640  43.6260  1.2910
  238.4790  46.8520  1.2300
  240.8130  49.9030  1.1660
  242.3840  54.2620  1.0150
  243.5960  59.0570  0.9950
  244.9980  66.4430  0.8930
  426.8550  66.4430  0.8930
  436.9650  66.4480  0.8930
  444.0040  66.4510  0.8930
```

1.14 Read setup file

Continue here if you have skipped the setup of the 10 -- 15 points and want to integrate again from the saved setup file.

1.14.1 If you have just made a setup and are checking it you will have your necessary parameters stored in memory.

1.14.2 If you are starting from a setup file, please go to the top of the page and execute until you have defined S_code and P_code. Doing this will avoid you accidentally changing anything.

[32]:
```
sfile=at.readTable('LDoubleshell_master.dat',sldir='./')
```

[33]:
```
plt.close(1111);plt.figure(1111)
sfile.plot('radius','S',shape='-o')
savefig('S3.png')
```

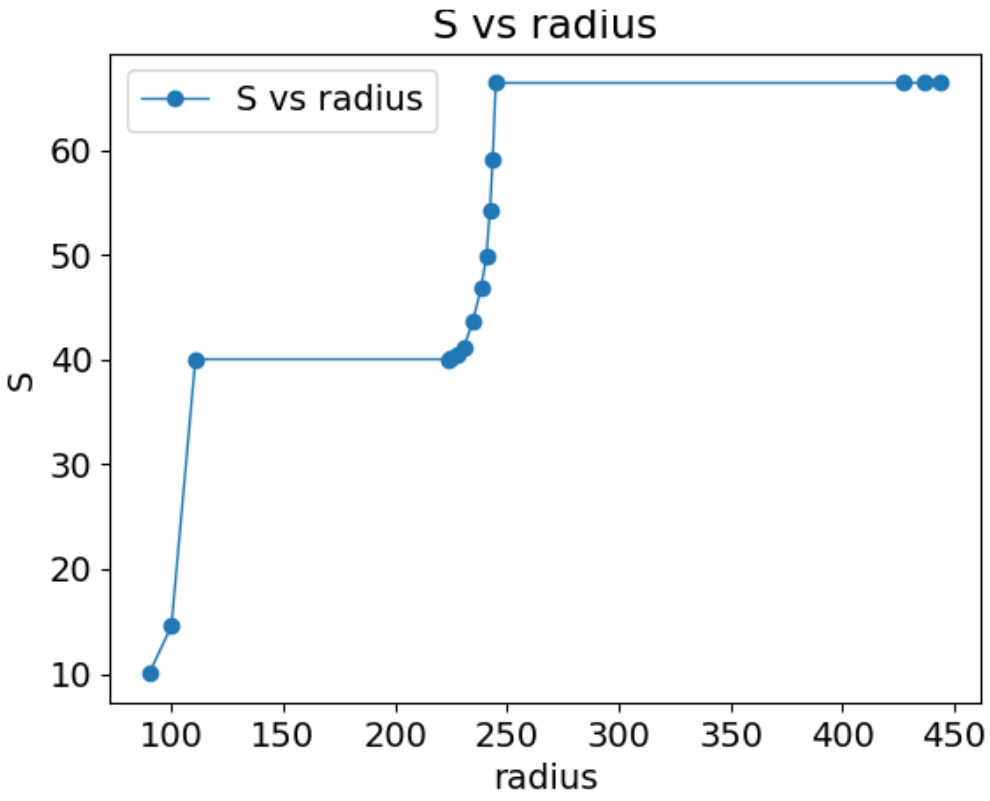

[35]:
```
plt.close(1112);plt.figure(1112)
sfile.plot('radius','mu',shape='-o')
savefig('mu1.png')
```

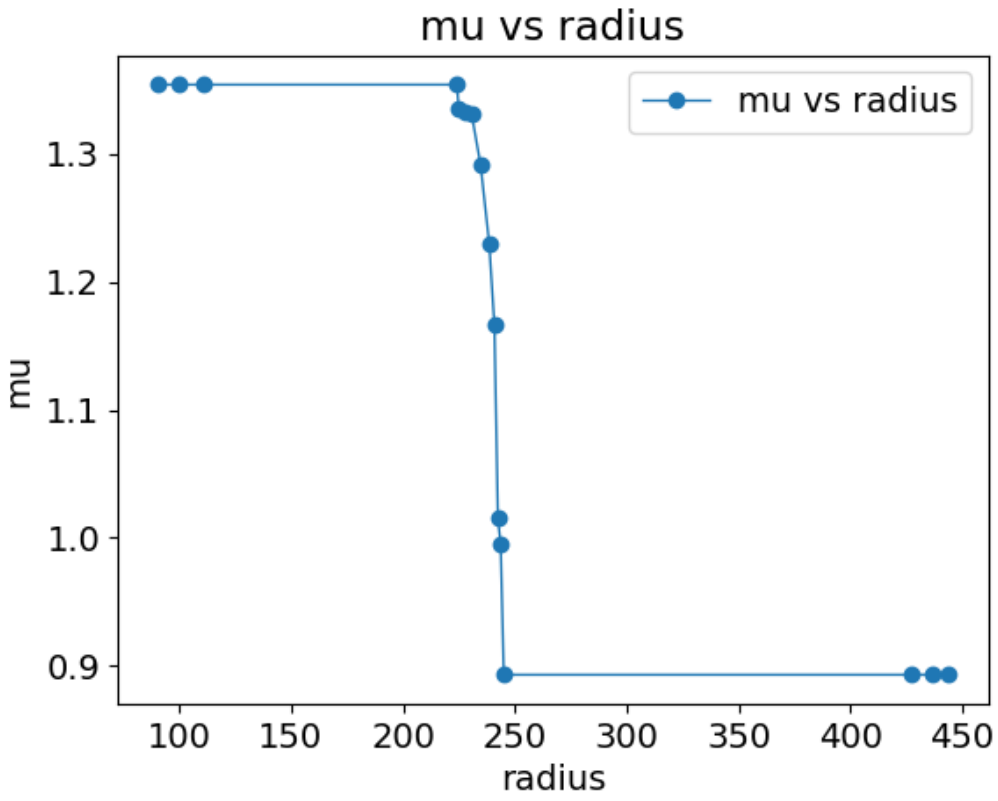

[36]:
```
S_points=sfile.data['S']
mu_points=sfile.data['mu']
radius_points=sfile.data['radius']
```

[37]:
```
pressure_string = [ x  for x in sfile.hattrs if "P0" in x]
mass_string = [ x  for x in sfile.hattrs if "m0" in x]
P0=float(pressure_string[0].split('=')[1]) #read the pressure and mass at the␣
 ↪base from the setup file to start the integration below
m0=float(mass_string[0].split('=')[1])
```

1.15 Final integration

What follows will take place in the inirad code of PPMstar.F.

1.15.1 smoothing out the edges of mu and S

1. define ppm grid
2. linear interpolation on PPM grid and running box average with by N=2*Nconv+1 kernel

[38]:
```
# generate radius grid, we have that already, of course, in PPM
rppm=linspace(radbase+1,radout0-1,ngrid-ncore+1) #the +1 and -1 are to kee the␣
 ↪points inside the interpolation range
# interpolate linear the PPM grid to the sparse points
f_Spoints=interpolate.interp1d(radius_points,S_points,kind='linear')
Sppm=f_Spoints(rppm)
f_mupoints=interpolate.interp1d(radius_points,mu_points,kind='linear')
muppm=f_mupoints(rppm)
```

[39]:
```
# smooth the edges, but don't do anything at the boundaries
Ngrid=len(rppm)
Sconv=ones(Ngrid)
muconv=ones(Ngrid)
for i in range(Ngrid):
    nmin = int(max(i-Nconv,0)); nmax = int(min(i+Nconv+1,Ngrid))
    if min(i-0,Ngrid-1-i) < Nconv:   # near the boundary
        Sconv[i] = Sppm[i]
        muconv[i] = muppm[i]
    else:
        Sconv[i]  = sum(Sppm[nmin:nmax])/(nmax-nmin)
        muconv[i] = sum(muppm[nmin:nmax])/(nmax-nmin)
Sppm  = Sconv
muppm = muconv
```

[40]:
```
rhs3 = lambda x,r: ps.rhs4(x,r,T,rho,P)
```

[41]:
```
Rbymu = ps.R_code/muppm[0]
T   = exp(Sppm[0]/Rbymu + log(P0/Rbymu))**(2./5) # guess from ideal
rho = P0/Rbymu/T                                 # gas for first grid point

h  = diff(rppm)[0]                           # dx, cell size
x = [m0,P0]                                  # initial condition at lower␣
 ↪boundary
Tppm = ones(len(rppm)); rhoppm = ones(len(rppm)) # output arrays
mppm = ones(len(rppm)); pppm = ones(len(rppm))


for i in range(0,len(rppm)):
    m,P = x
    S = Sppm[i]; mu = muppm[i]; r = rppm[i]         # input from profile
```

```
    rho, T = ps.rhoTfromSP(T,rho,S,P,ps.a_code,ps.R_code,mu) # rho,T from␣
↪S,P,mu via EOS, use previous rho,T as initial guess
    rhoppm[i] = rho; Tppm[i]   = T; mppm[i]   = m   # save values
    pppm[i] = P
    k1 = h*array(rhs3(x,r))                    # RK4
    k2 = h*array(rhs3(x+k1/2.,r+h/2.))
    k3 = h*array(rhs3(x+k2/2.,r+h/2.))
    k4 = h*array(rhs3(x+k3,r+h))
    x=x+(k1+2*k2+2*k3+k4)/6.
```

[42]:
```
headers = ["M45, Z=0","Interpolated and integrated from setup file", "all␣
↪quantities in code units",\
           "setup file: LDoubleshell_master.dat.dat"]
dcols   = ['radius','S','mu','T','rho','P']
data    = [rppm,Sppm,muppm,Tppm,rhoppm,pppm]
at.write('LDoubleshell_int.dat', headers, dcols, data)
```

```
Warning this method will overwrite ./LDoubleshell_int.dat
Would you like to continue? (y)es or (n)no?

-->  yes

Yes selected
Continuing as normal
```

[43]:
```
nup = where(radius_code>radout0)[0][-1]
nn  = where(radius_code<radin0)[0][0]
plt.close(50);plt.figure(50)
plt.plot(radius_code[nn:nup:-1],m_code[nn:nup:-1],'-',label="MESA model")
plt.plot(rppm,mppm,'--',label="setup")
xlabel('radius');ylabel('mass')
plt.legend()
savefig('mass.png')
```

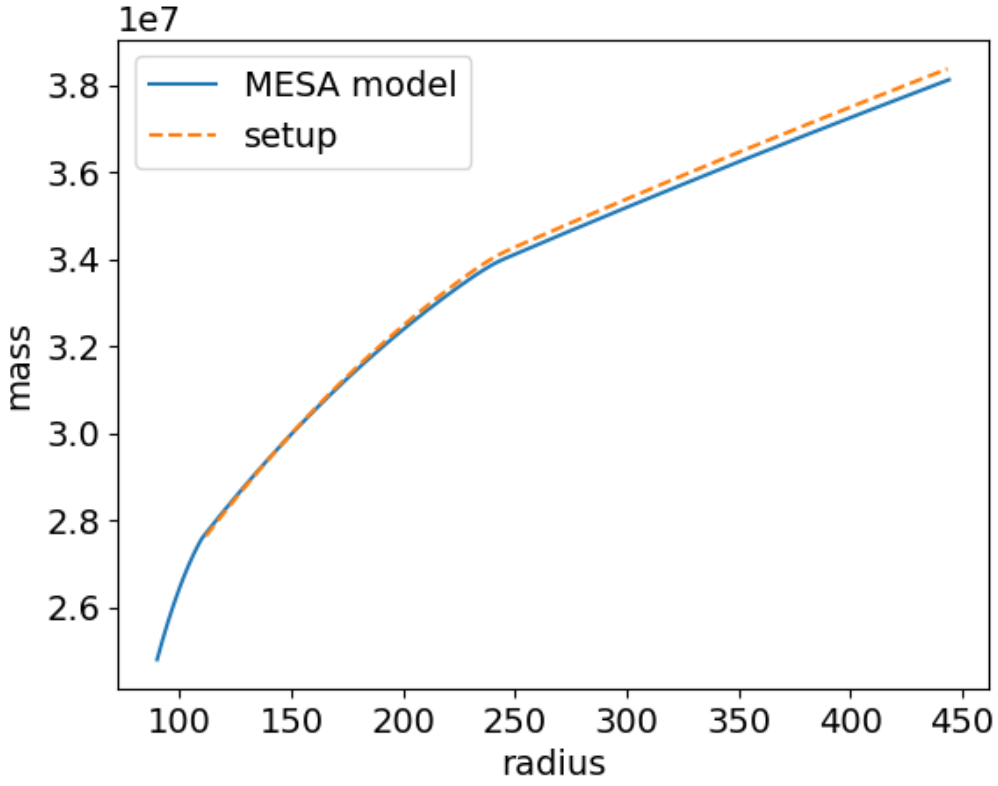

[45]:
```
plt.close(153);plt.figure(153)
plt.plot(radius_code[nn:nup:-1],rho_code[nn:nup:-1],'-',label="MESA model")
plt.plot(rppm,rhoppm,'--',label="setup")
xlabel('radius');ylabel('$\\rho$')
plt.legend()
savefig('rho.png')
```

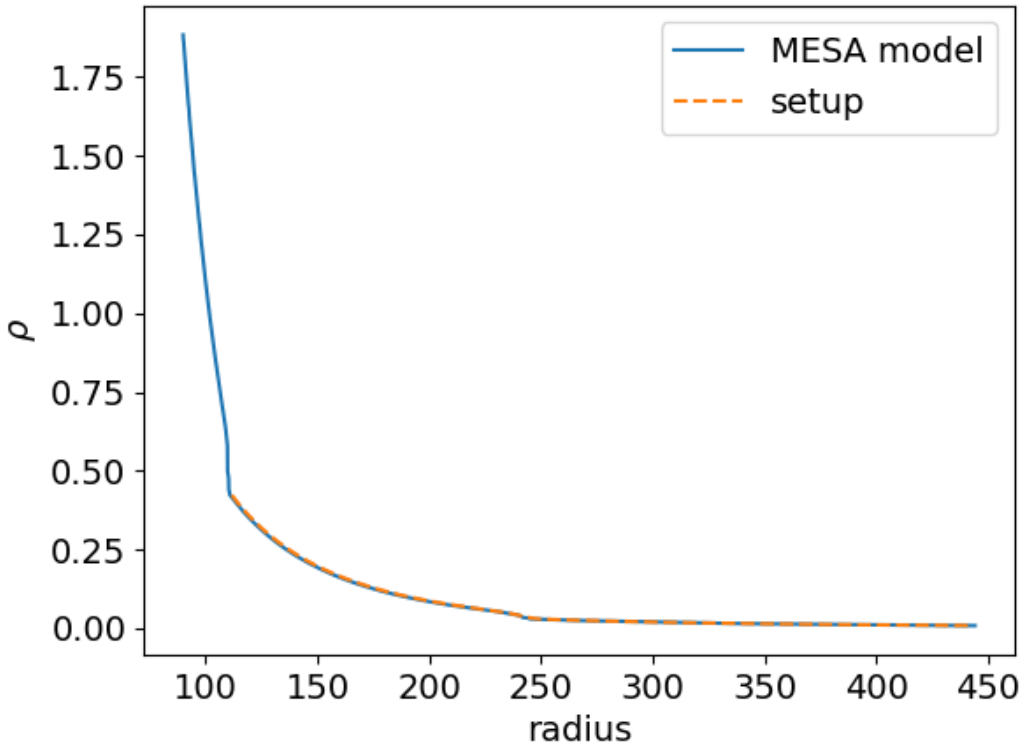

[47]:
```
plt.close(152);plt.figure(152)
plt.plot(radius_code[nn:nup:-1],T_code[nn:nup:-1],'-',label="MESA model")
plt.plot(rppm,Tppm,'--',label="setup")

xlabel('radius');ylabel('T')
plt.legend()
savefig('T.png')
```

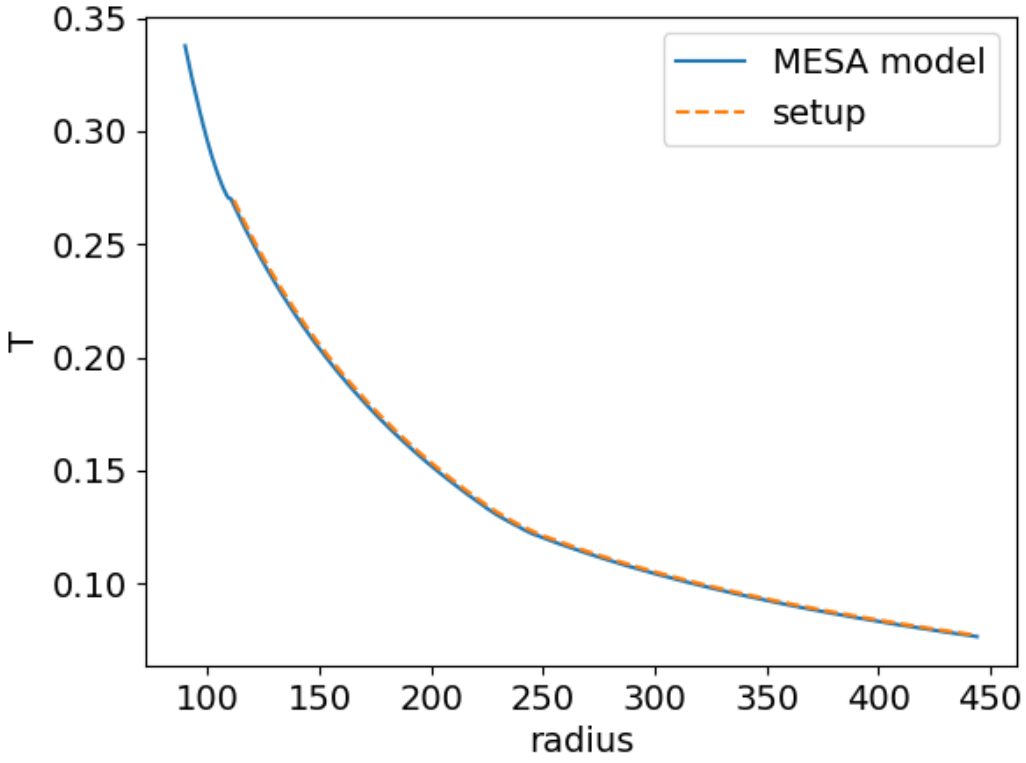

[49]:
```
plt.close(53);plt.figure(53)
plt.plot(radius_code[nn:nup:-1],S_code[nn:nup:-1],'-',label="MESA model")
plt.plot(rppm,Sppm,'--',label="setup")
sfile.plot('radius','S',shape='o')
xlabel('radius');ylabel('S')
#plt.xlim(rRK[0],rRK[-1]);plt.ylim(0.9*SRK[0],SRK[-1])
plt.legend()
savefig('S4.png')
```

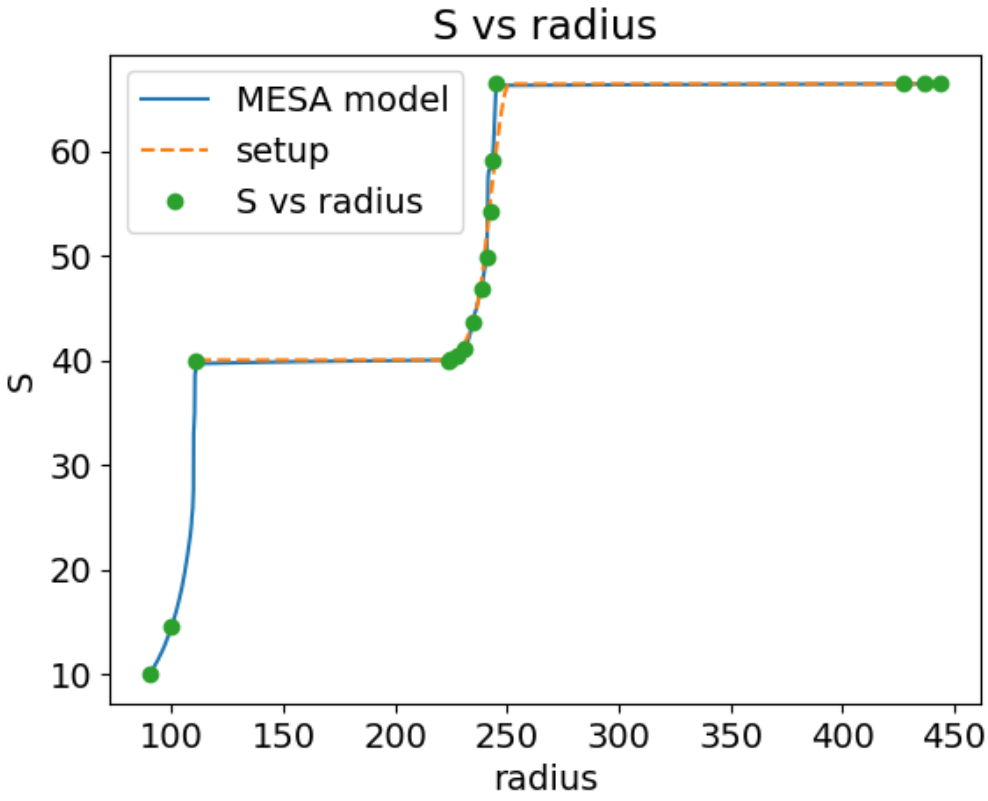
S vs radius
MESA model
setup
S vs radius
S
radius
10
20
30
40
50
60
100
150
200
250
300
350
400
450

Bibliography

Andrassy R., Herwig F., Woodward P., Ritter C., 2020, MNRAS, 491, 972

Arentsen A., Starkenburg E., Shetrone M. D., Venn K. A., Depagne É., McConnachie A. W., 2019, A&A, 621, A108

Arnett W. D., Meakin C., Viallet M., 2014, AIP Advances, 4, 041010

Arnould M., Goriely S., Takahashi K., 2007, Phys. Rep., 450, 97

Asplund M., Grevesse N., Sauval A. J., Scott P., 2009, ARA&A, 47, 481

Baade W., 1944, ApJ, 100, 137

Banerjee P., Qian Y.-Z., Heger A., 2018, ApJ, 865, 120

Barkana R., Loeb A., 2001, Phys. Rep., 349, 125

Battino U., et al., 2016, ApJ, 827, 30

Beers T. C., Christlieb N., 2005, ARA&A, 43, 531

Beers T. C., Sivarani T., Marsteller B., Lee Y., Rossi S., Plez B., 2007, AJ, 133, 1193

Bessell M. S., et al., 2015, ApJ, 806, L16

Böhm-Vitense E., 1958, Z. Astrophys., 46, 108

Bromm V., Yoshida N., 2011, ARA&A, 49, 373

Campbell S. W., Lugaro M., Karakas A. I., 2010, A&A, 522, L6

Casanova J., José J., García-Berro E., Shore S. N., Calder A. C., 2011, Nature, 478, 490

Castellani V., Paolicchi P., 1975, Ap&SS, 35, 185

Chen K.-J., Heger A., Almgren A. S., 2013, Astronomy and Computing, 3, 70

Chiappini C., Hirschi R., Meynet G., Ekström S., Maeder A., Matteucci F., 2006, A&A, 449, L27

Chiosi C., 1983, Mem. Soc. Astron. Italiana, 54, 251

Choplin A., Maeder A., Meynet G., Chiappini C., 2016, A&A, 593, A36

Choplin A., Ekström S., Meynet G., Maeder A., Georgy C., Hirschi R., 2017, A&A, 605, A63

Christlieb N., Gustafsson B., Korn A. J., Barklem P. S., Beers T. C., Bessell M. S., Karlsson T., Mizuno-Wiedner M., 2004, ApJ, 603, 708

Clarkson O., Herwig F., 2020, Monthly Notices of the Royal Astronomical Society

Clarkson O., Herwig F., Pignatari M., 2018, MNRAS, 474, L37

Clarkson O., Herwig F., Andrassy R., Woodward P., Pignatari M., Mao H., 2019a, pp 321–325, doi:10.1007/978-3-030-13876-9˙56, http://link.springer.com/10.1007/978-3-030-13876-9{_}56

Clarkson O., Herwig F., Pignatari M., 2019b, MNRAS, 488, 222

Colella P., Woodward P. R., 1984, Journal of Computational Physics, 54, 174

Couch S. M., 2017, Philosophical Transactions of the Royal Society of London Series A, 375, 20160271

Couch S. M., Chatzopoulos E., Arnett W. D., Timmes F. X., 2015, ApJ, 808, L21

Couture A., et al., 2008, Phys. Rev. C, 77, 015802

Cowan J. J., Rose W. K., 1977, ApJ, 212, 149

Cristallo S., Piersanti L., Straniero O., Gallino R., Domínguez I., Käppeler F., 2009, Publications of the Astronomical Society of Australia, 26, 139

Cristini A., Meakin C., Hirschi R., Arnett D., Georgy C., Viallet M., Walkington I., 2017, MNRAS, 471, 279

Cyburt R. H., et al., 2010, ApJS, 189, 240

Cyburt R. H., Fields B. D., Olive K. A., Yeh T.-H., 2016, Reviews of Modern Physics, 88, 015004

Dardelet L., et al., 2014, in XIII Nuclei in the Cosmos (NIC XIII), Proceedings of Science. (arXiv:1505.05500), https://pos.sissa.it/204/145

Davis A., Jones S., Herwig F., 2019, MNRAS, 484, 3921

Denissenkov P. A., Tout C. A., 2003, MNRAS, 340, 722

Denissenkov P. A., Herwig F., Woodward P., Andrassy R., Pignatari M., Jones S., 2019, MNRAS, 488, 4258

Doherty C. L., Gil-Pons P., Lau H. H. B., Lattanzio J. C., Siess L., Campbell S. W., 2014, MNRAS, 441, 582

Ebinger K., Curtis S., Ghosh S., Fröhlich C., Hempel M., Perego A., Liebendörfer M., Thielemann F.-K., 2020, ApJ, 888, 91

Eiden K., Zingale M., Harpole A., Willcox D., Cavecchi Y., Katz M. P., 2020, ApJ, 894, 6

Ekström S., Meynet G., Chiappini C., Hirschi R., Maeder A., 2008, A&A, 489, 685

Ezer D., 1961, ApJ, 133, 159

Ezer D., Cameron A. G. W., 1971, Ap&SS, 14, 399

Farmer R., Fields C. E., Petermann I., Dessart L., Cantiello M., Paxton B., Timmes F. X., 2016, The Astrophysical Journal Supplement Series, 227, 22

Fields C. E., Timmes F. X., Farmer R., Petermann I., Wolf W. M., Couch S. M., 2018, ApJS, 234, 19

Frebel A., Norris J. E., 2015, Annual Review of Astronomy and Astrophysics, 53, 631

Frebel A., et al., 2006, ApJ, 652, 1585

Frebel A., Collet R., Eriksson K., Christlieb N., Aoki W., 2008, ApJ, 684, 588

Frischknecht U., et al., 2016, MNRAS, 456, 1803

Fujimoto M. Y., Iben Icko J., Hollowell D., 1990, ApJ, 349, 580

García-Berro E., Ritossa C., Iben Icko J., 1997, ApJ, 485, 765

Gil-Pons P., Doherty C. L., Lau H., Campbell S. W., Suda T., Guilani S., Gutiérrez J., Lattanzio J. C., 2013, A&A, 557, A106

Goriely S., Siess L., 2004, A&A, 421, L25

Hampel M., Stancliffe R. J., Lugaro M., Meyer B. S., 2016, ApJ, 831, 171

Hampel M., Karakas A. I., Stancliffe R. J., Meyer B. S., Lugaro M., 2019, ApJ, 887, 11

Hansen C. J., Kawaler S. D., 1994, Stellar Interiors. Physical Principles, Structure, and Evolution., doi:10.1007/978-1-4419-9110-2.

Hansen T., et al., 2015, ApJ, 807, 173

Hartmann D., Woosley S. E., El Eid M. F., 1985, ApJ, 297, 837

Hartwig T., Bromm V., Loeb A., 2018, MNRAS, 479, 2202

Hauser W., Feshbach H., 1952, Physical Review, 87, 366

Heger A., Woosley S. E., 2010, ApJ, 724, 341

Heger A., Langer N., Woosley S. E., 2000, ApJ, 528, 368

Heger A., Fryer C. L., Woosley S. E., Langer N., Hartmann D. H., 2003, ApJ, 591, 288

Herwig F., 2000, A&A, 360, 952

Herwig F., 2004, ApJ, 605, 425

Herwig F., Bloecker T., Schoenberner D., El Eid M., 1997, A&A, 324, L81

Herwig F., Pignatari M., Woodward P. R., Porter D. H., Rockefeller G., Fryer C. L., Bennett M., Hirschi R., 2011, ApJ, 727, 89

Herwig F., VandenBerg D. A., Navarro J. F., Ferguson J., Paxton B., 2012, ApJ, 757, 132

Herwig F., Woodward P. R., Lin P.-H., Knox M., Fryer C., 2014, ApJ, 792, L3

Higgins E. R., Vink J. S., 2019, A&A, 622, A50

Hirano S., Hosokawa T., Yoshida N., Umeda H., Omukai K., Chiaki G., Yorke H. W., 2014, ApJ, 781, 60

Hirschi R., 2007, A&A, 461, 571

Hirschi R., Chiappini C., Meynet G., Maeder A., Ekström S., 2008, in Bresolin F., Crowther P. A., Puls J., eds, IAU Symposium Vol. 250, Massive Stars as Cosmic Engines. pp 217–230 (arXiv:0802.1675), doi:10.1017/S1743921308020528

Hollowell D., Iben Icko J., 1989, ApJ, 340, 966

Iben I. J., 1985, QJRAS, 26, 1

Iliadis C., 2007, Nuclear Physics of Stars, doi:10.1002/9783527692668.

Janka H.-T., Melson T., Summa A., 2016, Annual Review of Nuclear and Particle Science, 66, 341

Jones S., Ritter C., Herwig F., Fryer C., Pignatari M., Bertolli M. G., Paxton B., 2016, MNRAS, 455, 3848

Jones S., Andrassy R., Sandalski S., Davis A., Woodward P., Herwig F., 2017, MNRAS, 465, 2991

Kaiser E. A., Hirschi R., Arnett W. D., Georgy C., Scott L. J. A., Cristini A., 2020, MNRAS,

Käppeler F., Gallino R., Bisterzo S., Aoki W., 2011, Reviews of Modern Physics, 83, 157

Keller S. C., et al., 2014, Nature, 506, 463

Kippenhahn R., Weigert A., 1990, Stellar Structure and Evolution

Komiya Y., Suda T., Yamada S., Fujimoto M. Y., 2020, ApJ, 890, 66

Krtička J., Kubát J., 2006, A&A, 446, 1039

Kudritzki R.-P., Puls J., 2000, ARA&A, 38, 613

Langer N., 2012, Annual Review of Astronomy and Astrophysics, 50, 107

Langer N., El Eid M. F., Fricke K. J., 1985, A&A, 145, 179

Lau H. H. B., Stancliffe R. J., Tout C. A., 2009, MNRAS, 396, 1046

Limongi M., Chieffi A., 2012, ApJS, 199, 38

Limongi M., Chieffi A., Bonifacio P., 2003, ApJ, 594, L123

Liu B., Bromm V., 2020, MNRAS, 497, 2839

Lombardo I., Dell'Aquila D., He J.-J., Spadaccini G., Vigilante M., 2019, Phys. Rev. C, 100, 044307

Lugaro M., Karakas A. I., Stancliffe R. J., Rijs C., 2012, ApJ, 747, 2

Maeder A., Meynet G., 2015, A&A, 580, A32

Malaney R. A., 1986, MNRAS, 223, 683

Marassi S., Chiaki G., Schneider R., Limongi M., Omukai K., Nozawa T., Chieffi A., Yoshida N., 2014, ApJ, 794, 100

Marigo P., Girardi L., Chiosi C., Wood P. R., 2001, A&A, 371, 152

Masseron T., Johnson J. A., Plez B., van Eck S., Primas F., Goriely S., Jorissen A., 2010, A&A, 509, A93

Meakin C. A., Arnett D., 2007, ApJ, 667, 448

Meyer B. S., Krishnan T. D., Clayton D. D., 1996, ApJ, 462, 825

Miller Bertolami M. M., Althaus L. G., Serenelli A. M., Panei J. A., 2006, A&A, 449, 313

Miralda-Escudé J., Haehnelt M., Rees M. J., 2000, ApJ, 530, 1

Mocák M., Meakin C., Campbell S. W., Arnett W. D., 2018, MNRAS, 481, 2918

Müller B., Melson T., Heger A., Janka H.-T., 2017, MNRAS, 472, 491

Nomoto K., Kobayashi C., Tominaga N., 2013, ARA&A, 51, 457

Nordlander T., Amarsi A. M., Lind K., Asplund M., Barklem P. S., Casey A. R., Collet R., Leenaarts J., 2017, A&A, 597, A6

Norris J. E., Gilmore G., Wyse R. F. G., Yong D., Frebel A., 2010, ApJ, 722, L104

Norris J. E., et al., 2013, ApJ, 762, 28

O'Connor E., Ott C. D., 2011, ApJ, 730, 70

Paxton B., et al., 2015, ApJS, 220, 15

Pian E., et al., 2017, Nature, 551, 67

Pignatari M., Gallino R., Meynet G., Hirschi R., Herwig F., Wiescher M., 2008, ApJ, 687, L95

Pignatari M., et al., 2015, ApJ, 808, L43

Pignatari M., et al., 2016, ApJS, 225, 24

Placco V. M., et al., 2016, ApJ, 833, 21

Plez B., Cohen J. G., 2005, A&A, 434, 1117

Prantzos N., 2000, New Astron. Rev., 44, 303

Rauscher T., Thielemann F.-K., 2000, Atomic Data and Nuclear Data Tables, 75, 1

Reed D. S., Bower R., Frenk C. S., Jenkins A., Theuns T., 2007, MNRAS, 374, 2

Ritossa C., García-Berro E., Iben Icko J., 1999, ApJ, 515, 381

Ritter C., Herwig F., Jones S., Pignatari M., Fryer C., Hirschi R., 2017, MNRAS, submitted, arXiv:1709.08677

Ritter C., Herwig F., Jones S., Pignatari M., Fryer C., Hirschi R., 2018, MNRAS, 480, 538

Robertson B. E., Ellis R. S., Furlanetto S. R., Dunlop J. S., 2015, ApJ, 802, L19

Roederer I. U., Preston G. W., Thompson I. B., Shectman S. A., Sneden C., 2014, ApJ, 784, 158

Roederer I. U., Karakas A. I., Pignatari M., Herwig F., 2016, ApJ, 821, 37

Rydberg C.-E., Whalen D. J., Maturi M., Collett T., Carrasco M., Magg M., Klessen R. S., 2020, MNRAS, 491, 2447

Ryden B., 2003, Introduction to cosmology

Schlattl H., Cassisi S., Salaris M., Weiss A., 2001, ApJ, 559, 1082

Schwarzschild M., Härm R., 1958, ApJ, 128, 348

Schwarzschild M., Spitzer L., 1953, The Observatory, 73, 77

Seitenzahl I. R., et al., 2013, MNRAS, 429, 1156

Smith N., 2014, ARA&A, 52, 487

Smith N., Li W., Silverman J. M., Ganeshalingam M., Filippenko A. V., 2011, MNRAS, 415, 773

Spitzer L., 1962, Physics of Fully Ionized Gases

Stacy A., Greif T. H., Bromm V., 2012, MNRAS, 422, 290

Stacy A., Bromm V., Lee A. T., 2016, MNRAS, 462, 1307

Stancliffe R. J., Dearborn D. S. P., Lattanzio J. C., Heap S. A., Campbell S. W., 2011, ApJ, 742, 121

Starrfield S., Truran J. W., Sparks W. M., 1975, ApJ, 198, L113

Stothers R., 1970, MNRAS, 151, 65

Suda T., Fujimoto M. Y., 2010, MNRAS, 405, 177

Sukhbold T., Adams S., 2020, MNRAS, 492, 2578

Sukhbold T., Woosley S. E., 2014, ApJ, 783, 10

Sukhbold T., Woosley S. E., Heger A., 2018, ApJ, 860, 93

Surace M., Zackrisson E., Whalen D. J., Hartwig T., Glover S. C. O., Woods T. E., Heger A., Glover S. C. O., 2019, MNRAS, 488, 3995

Susa H., Hasegawa K., Tominaga N., 2014, ApJ, 792, 32

Takahashi K., Umeda H., Yoshida T., 2014, ApJ, 794, 40

Truran J. W., Cameron A. G. W., 1971, Ap&SS, 14, 179

Turk M. J., Abel T., O'Shea B., 2009, Science, 325, 601

Umeda H., Nomoto K., 2003, Nature, 422, 871

Vanzella E., et al., 2020, MNRAS, 494, L81

Venn K. A., et al., 2020, MNRAS, 492, 3241

Wanajo S., Janka H.-T., Müller B., 2013, ApJ, 767, L26

Wiescher M., Görres J., Uberseder E., Imbriani G., Pignatari M., 2010, Annual Review of Nuclear and Particle Science, 60, 381

Wise J. H., Turk M. J., Norman M. L., Abel T., 2012, ApJ, 745, 50

Woods T. E., Heger A., Haemmerlé L., 2020, MNRAS, 494, 2236

Woodward P., Herwig F., Porter D., Fuchs T., Nowatzki A., Pignatari M., 2008, in O'Shea B. W., Heger A., eds, American Institute of Physics Conference Series Vol. 990, First Stars III. pp 300–308 (arXiv:0711.2091), doi:10.1063/1.2905567

Woodward P. R., Herwig F., Lin P.-H., 2015, ApJ, 798, 49

Woosley S. E., Weaver T. A., 1982, in Rees M. J., Stoneham R. J., eds, NATO Advanced Science Institutes (ASI) Series C Vol. 90, Supernovae: A survey of current research. pp 79–116

Woosley S. E., Heger A., Weaver T. A., 2002, Rev. Mod. Phys., 74, 1015

Yadav N., Müller B., Janka H. T., Melson T., Heger A., 2019, arXiv e-prints, p. arXiv:1905.04378

Yong D., et al., 2013, ApJ, 762, 26

Yoon S. C., Dierks A., Langer N., 2012, A&A, 542, A113

Yoon J., et al., 2016, ApJ, 833, 20

Zingale M., et al., 2002, ApJS, 143, 539